# ABSTRACT

Title of dissertation: ASYMMETRIC INTERCALATION OF
TRANSITION METAL CHALCOGENIDES

Huafei Zheng, Doctor of Philosophy, 2025

Dissertation directed by: Professor Efrain E. Rodriguez
Department of Chemistry and Biochemistry

Layered transition metal chalcogenides (TMCs) offer a versatile platform for novel quantum properties through intercalation chemistry. By intercalating molecular species into the van der Waals gaps, one can modulate the host structure, tune electronic correlations, and even break the symmetries of the structure. In particular, the use of polar and chiral amines enables the disruption of inversion symmetry, giving rise to polar metallic states or enhanced superconducting behavior.

This dissertation investigates the intercalation of amines, including chiral molecules, into layered transition metal chalcogenides (TMCs) through hydrothermal and solvothermal synthesis. By inserting organic molecules into the gaps between the layers of inorganic hosts, new hybrid materials were constructed with tunable electronic and magnetic properties. A polar ferromagnetic metal was realized by intercalating $[Co(en)_3]^{2+}$ complexes into CoS, where hydrogen bonding

disrupts inversion symmetry while preserving metallic conductivity. Chiral amine intercalation into $TaSe_2$ was shown to enhance its superconducting transition temperature (Tc) up to 7 K. To probe the mechanisms underlying intercalation and crystallization, in-situ synchrotron powder X-ray diffraction was applied to monitor time-resolved structural evolution under eight different hydrothermal and solvothermal conditions. The study revealed differences in crystallization kinetics and intermediate phases, depending on precursor chemistry and solvent properties.

# ASYMMETRIC INTERCALATION OF TRANSITION METAL CHALCOGENIDES

By

Huafei Zheng

Dissertation submitted to the Faculty of the Graduate School of the
University of Maryland, College Park, in partial fulfillment
of the requirements for the degree of
Doctor of Philosophy
2025

Advisory Committee:

Professor Efrain E. Rodriguez, Chair/advisor

Professor Johnpierre Paglione, Dean's Representative

Professor Andrei Vedernikov

Professor Mercedes Taylor

Professor Zhiwei Li

# Dedication

The dedication of this dissertation is split to three ways:  To my father, who introduced me to the brilliant world of chemistry. To my advisor, Efrain, for his guidance, kindness, patience and support. To Guoliang and Hanlin, whose friendship help me navigate the challenges of living and studying.

# Acknowledgements

I would like to thank my advisor Professor Efrain Rodrguez for the guidance throughout my research and this dissertation work. Especially, I appreciate the friendly and supportive atmosphere he creates in the group, which quietly provided the space I needed to refocus and regain my confidence. I would also like to thank my other committee members, Professor Andrei Vedernikov, Johnpierre Paglione, Mercedes Talyor and Zhiwei Li for their time to review this dissertation and providing valuable advice to improve the work.

I am thankful to the past and present members of the Rodriguez group for their camaraderie and generous help in the lab. In particular, I would like to thank Dr. Xiuquan Zhou and Dr. Brandon Wilfong for mentoring me when I first joined the group. I also appreciate the support and insightful discussions from Lahari Balisetty, Cein Mandujano, Stephanie Hong, and Ryan Stadel throughout my research.

I gratefully acknowledge Dr. Peter Zavalij at the X-ray Crystallographic Center for his assistance with crystal structure determination. Also, as the TA at XCC, I also had the opportunity to learn a great deal about diffraction from Peter. I thank Amanda Brocki for her support with TGA-MS measurements. I also appreciate Dr. Zhongxuan Wang's kind help in arranging time for circular dichroism measurements and Dr. Jihun Park for the help in resistance measurements.

Research at University of Maryland was supported by the National Science Foundation NSF DMR-2113682 and the Department of Commerce NIST Award No. 70NANB12H238. I acknowledge support from the X-ray Crystallographic Center, Quantum Materials Center, and the Maryland Nanocenter for allowing the use of facilities necessary to my research. I would like

to acknowledge support from the Advanced Photon Source at Argonne National Laboratory, and the Spallation Neutron Source at Oak Ridge National Laboratory for providing high-resolution synchrotron and neutron diffraction data essential for my research.

Being far from home often means uncertainty and loneliness. I really appreciate that I have some amazing friends who have shared the rental house we live in over years since our first day here. We cooked together, took trips together, faced challenges together and looked after each other, especially during the pandemic. Besides, I always feel true fortunate to have known Guoliang and Hanlin, whose friendship and advice meant a great deal to me through this journey.

And finally, I thank my parents for their love and support.

# Table of Contents

Dedication ........ ii
Acknowledgements ........ iii
Table of Contents ........ v
List of Tables ........ vi
List of Figures ........ viii
List of Abbreviations ........ xi

Chapter 1: Introduction

- 1.1 Transition metal chalcogenides ........ 1
- 1.2 Compound intercalation ........ 3
- 1.3 Hydrogen bonding ........ 6
- 1.4 Hydrothermal and solvothermal reactions ........ 9
- 1.5 Objective and outline ........ 14

Chapter 2: Methods

- 2.1 Synthetic Methods ........ 17
  - 2.1.1 In-situ intercalation ........ 17
  - 2.1.2 Ex-situ intercalation ........ 18
- 2.2 X-ray diffration ........ 19
  - 2.2.1 Laboratory Powder X-ray diffraction ........ 20
  - 2.2.2 Single crystal X-ray diffraction ........ 22
  - 2.2.3 Synchrotron X-ray diffraction ........ 22
- 2.3 Neutron diffraction ........ 23
- 2.4 Magnetic susceptibility measurement ........ 27
- 2.5 Electrical transport measurements ........ 29
- 2.6 Thermogravimetric analysis ........ 31
- 2.7 Circular dichroism ........ 32

Chapter 3: Solvothermal synthesis of amine intercalated Fe and Co chalcogenides and and polar ferromagnetic breaking the crystal symmetry.

- 3.1 Introduction ........ 34
- 3.2 Experimental and computational methods ........ 37
  - 3.2.1 Sample synthesis ........ 37
  - 3.2.2 Diffraction study ........ 40
  - 3.2.3 Magneitc measurements ........ 41
  - 3.2.4 Resistivity measurements ........ 42
  - 3.2.5 First-princples calculations ........ 42
- 3.3 Results ........ 42
  - 3.3.1 Crystal structure ........ 42
  - 3.3.2 Magnetism ........ 49
  - 3.3.3 Electrical transport ........ 51
  - 3.3.4 Electronic structure ........ 52

3.4 Discussion ........................................................................................... 53
3.4.1 Hydrogen bonding ................................................................................ 53
3.4.2 Role of metal-amine complex ............................................................. 56
3.4.3 Polar metals .......................................................................................... 57
3.4.4 Band ferromagnetism in en-CoS ........................................................ 60
3.5 Conclusions ........................................................................................... 62
Chapter 4: Chiral amine intercalations into TMDs ................................... 65
4.1 Introduction .......................................................................................... 65
4.2 Experimental methods .......................................................................... 68
4.2.1 Sample syntheis ................................................................................... 68
4.2.2 X-ray diffraction study ........................................................................ 69
4.2.3 Magnetic measurement ........................................................................ 70
4.2.4 Electric transport measurement .......................................................... 70
4.2.5 Chiral dichroism ................................................................................... 70
4.2.6 Thermogravimetric analysis ................................................................ 71
4.3 Results and discussions ........................................................................ 71
5.3.1 Crystal strcuture and synthesis ........................................................... 71
5.3.2 Superconductivity ................................................................................ 79
4.4 Conclusion ............................................................................................ 83

Chapter 5: In-situ synchro X-ray study on hydrothermal and solvothermal TMC intercalations.

5.1 Introduction .......................................................................................... 85
5.2 Experiements ........................................................................................ 88
5.2.1 In-situ experiments and set-ups ........................................................... 88
5.2.2 Hydrothermal/solvotheraml synthesis with Fe ................................... 89
5.2.3 Bottom-up hydrothermal/solvotheraml synthesis with Co .................. 90
5.3 Results and discussions ........................................................................ 92
5.3.1 Bottom-up intercalations of $(Li_{1-x}Fe_xOH)FeS$ .......................... 92
5.3.2 $KFe_2S_2$ deintercalation with LiOH .................................................. 97
5.3.3 $KFe_2S_2$ deintercalation with NaOH ................................................ 102
5.3.4 $KFe_2Se_2$ deintercalation with LiOH ................................................ 105
5.3.5 Bottom-up ammonia intercalations into FeS with guanidine ............ 108
5.3.6 Bottom-up solvothermal intercalations of ethylenediamine into CoS ........ 112
5.3.7 Bottom-up solvothermal intercalations of 1,2-diaminopropane into CoS ... 115
5.3.8 Bottom-up solvothermal intercalations of 1,2-diaminopropane into FeS .... 118
5.3.9 Summary .............................................................................................. 120
5.4 Conclusions ........................................................................................... 122

Chapter 6: Conclusions and future works

6.1 Conclusions ........................................................................................... 124
6.2 Future works ......................................................................................... 125
6.2.1 Chiral biologically relevant molecule inrercalation ............................ 125
6.2.2 Co-intercalations .................................................................................. 126
Bibliography .............................................................................................. 128

# List of Tables

1.1. Mean values for over 700 organic structures contaiong the hydrogen bond to S or Se. Study by Allen *et al*. ……………………………………………………………………………………………..………..8

1.2 Parameters involving hydrogen for several intercalated Fe*Ch*…………………………………………9

3.1 Single crystal X-ray diffraction data for [Co(*en*)$_3$]Cl$_2$· *en* and [Co(*en*)$_3$]Cl$_2$…………………….…….41

3.2 Relevant bond distances (Å) and bond angles (°) for the Co(*en*)$_3$ complex …………………….……..48

3.3. Hydrogen bond distances (Å) and bond angles (°) for the Co(*en*)$_3$ complex…………………………56

# List of Figures

1.1: Classification of transition metal chalcogenides (TMCs) based on crystal structure and transition metal identity…………………………………………………………………………………….…. 2

1.2: Three approaches of intercalation in synthesis based on the starting materials……………………......5

1.3: The general structure of a hydrogen bond…………………………………………………………....7

1.4: Illustration of a natural hydrothermal system at a mid-ocean ridge…………………….….………10

1.5: autoclaves……………………………………………………………………………..……13

2.1: Schematic illustration of Bragg's Law…………………………………………………..………19

2.2: Neutron scattering vs. X-ray scattering…………………………………………………..………24

2.3: Representative magnetic susceptibility ($\chi$) vs. temperature (T) curves……………………..……....28

2.4: Schematic and optical image of a four-probe resistivity measurement setup……………………...30

3.1: Tetrahedral transition metal chalcogenides (TTMCs)…………………………………..…….36

3.2: The powder XRD patterns of ground polycrystalline $[\mathrm{Co}(en)_3](\mathrm{CoS})_{12} \cdot en$ ……………………....38

3.3: The synchrotron XRD patterns of polycrystalline $[\mathrm{Co}(en)_3](\mathrm{CoS})_{12} \cdot en$ ………………………..……38

3.4: The powder XRD patterns of ground polycrystalline samples of the solvothermally prepared products under different reaction conditions…………………………………………………………………. 39

3.5: The powder XRD patterns collected at room temperature of ground polycrystalline sample of the solvothermally prepared product for different number of days. …………………………...………...….40

3.6: Precession images of single crystal x-ray diffraction. ………………………………………………… 44

3.7: Full precession images of the hk0- and 0kl-planes from single crystal diffraction…………………. 46

3.8: The two N—H…S hydrogen bonds that determine the polarity of en-CoS from single crystal structure ……………………………………………………………………………………………..47

3.9: Single crystal structure of en-CoS viewed down the *c*-axis……………………………………… 48

3.10: Field dependent magnetic measurements of a polycrystalline en-CoS sample ……………………..49

3.11: Temperature dependent resistivity of a pressed pellet of as-recovered polycrystalline en-CoS samples at zero applied field. ……………………………………………………………………………50

3.12: Electronic density of states (DOS)…………………………………………………………… 52

3.13: The two N—H…S hydrogen bonds that determine the polarity of en-CoS from single crystal structure. ……………………………………………………………………………………………..55

3.14: Crystal structure of $[\mathrm{Co}(en)_3]\mathrm{Cl}_2$……………………………………………………………….…58

3.15: The chiral $[Co(en)_3]^{2+}$ complexes in en-CoS…………………………………………………… 59

3.16: Calculated magnetic moment per Co site under electrostatic doping as computed for CoS layers….62

3.17: The powder XRD patterns of ground polycrystalline samples of the solvothermal prepared products with two different chalcogen sources……………………………………………………………….. 63

4.1: Molecular structures of enantiopure α-methylbenzylamine derivatives……………………...….72

4.2: Powder X-ray diffraction (XRD) patterns…………………………………………………...…74

4.3: Le Bail refinement of the neutron diffraction pattern of the intercalated $TaSe_2$ sample……..……….76

4.4: Circular dichroism……………………………………………………………………….………77

4.5: Thermogravimetric analysis of *en*–$TaSe_2$, RMBA–$TaSe_2$, and SMBA–$TaSe_2$………………………78

4.6: Temperature-dependent magnetic susceptibility of (a) en–$TaSe_2$ and (b) RMBA–$TaSe_2$…………..…80

4.7: resistance R–T curves…………………………………………………………………………81

4.8:: Magnetic susceptibility (χ) of SMBA–intercalated $TaSe_2$……………………………………………82

5.1:Schemes of in-situ reactions……………………………………………………………………….. 88

5.2: In-situ synchrotron powder X-ray diffraction contour plot of the hydrothermal reaction between Fe and thiourea in the presence of LiOH……………………………………………………………..…...93

5.3: Evolution of phase composition and lattice parameters during the hydrothermal reaction of Fe with thiourea and LiOH……………………………………………………………………………………94

5.4: Kinetic analysis and proposed mechanism of Fe consumption during the hydrothermal synthesis of $(Li_{1-x}Fe_xOH)FeS$……………………………………………………………………………….…….95

5.5: Time-resolved in-situ synchrotron powder X-ray diffraction contour plot for the hydrothermal transformation of $KFe_2S_2$ into $(Li_{1-x}Fe_xOH)FeS$………………………………………………….………98

5.6: Evolution of the weight percentages of Fe (blue), $(Li_{1-x}Fe_xOH)FeS$ (orange), and $KFe_2S_2$…………...99

5.7: Time-dependent evolution of the lattice parameters……………………………………….……..101

5.8: In-situ synchrotron PXRD contour plot of the hydrothermal reaction between Fe powder, NaOH, and thiourea…………………………………………………………………………………….………103

5.9 Evolution of the relative weight percentages of crystalline phases during the hydrothermal reaction of Fe powder, NaOH, and thiourea……………………………………………………………..……..104

5.10: In-situ synchrotron powder X-ray diffraction contour plot showing the time-resolved structural evolution of the $KFe_2Se_2$ + LiOH…………………………………………………………..………..…106

5.11: Summary of structural evolution during the hydrothermal reaction of $KFe_2Se_2$ in LiOH…………107

5.12: In-situ synchrotron powder X-ray diffraction contour plot showing the hydrothermal formation of $(H_{0.5}NH_3)Fe_2S_2$…………………………………………………………………………….……..108

5.13: Time-dependent phase composition during the hydrothermal synthesis of $(H_{0.5}NH_3)Fe_2S_2$ ………111

5.14: Lattice parameter evolution of the intermediate and product phases during the hydrothermal reaction of Fe, thiourea, and guanidine……………………………………………………………………112

5.15: In-situ synchrotron powder X-ray diffraction contour plot showing the solvothermal reaction of Co metal thiourea, and ethylenediamine ………………………………………………………...…..114

5.16: Phase evolution during the solvothermal synthesis of [Co(en)3](CoS)12·en……………………… 115

5.17: Time evolution of the lattice parameters of [Co(en)3](CoS)12·en obtained from sequential Rietveld refinements ………………………………………………………………………………………116

5.18: In-situ synchrotron powder X-ray diffraction contour plot showing the solvothermal reaction of Co metal, thiourea, and 1,2-diaminopropane ……………………………………………………………...117

5.19: Time-resolved evolution of crystalline parameters during the solvothermal synthesis of CoS–1,2-dap …………………………………………………………………………………………118

5.20: In-situ synchrotron powder X-ray diffraction contour plot of the solvothermal reaction between Fe, thiourea, and 1,2-diaminopropane ………………………………………………………………120

5.21: Time-resolved structural evolution during the solvothermal synthesis of FeS(1,2-dap) from Fe, thiourea, and 1,2-diaminopropane ………………………………………………………………121

# List of Abbreviations

| | |
|---|---|
| APS | Advanced Photon Source |
| CD | circular dichroism |
| CISS | chiral-induced spin selectivity |
| DC | direct current |
| *en* | ethylenediamine |
| FC | field-cooled |
| MBA | methylbenzylamine |
| MPMS | Magnetic Properties Measurement System |
| PXRD | powder X-ray diffraction |
| QMC | Quantum Materials Center |
| SQUID | Superconducting Quantum Interference Device |
| TGA | thermogravimetric analysis |
| TMC | transition metal chalcogenides |
| TMD | transition metal chalcogenide |
| TMDC | transition metal dichalcogenide |
| TTMC | tetragonal transition metal chalcogenide |
| TRSB | time-reversal symmetry |
| $T_c$ | Critical Temperature |
| XRD | X-ray diffraction |
| ZFC | Zero Field-cooled |
| vDW | van der Waals |
| 1,2-dap | 1,2-diaminopropane |

# Chapter 1: Introduction

## 1.1 Transition metal chalcogenides

Transition metal chalcogenides (TMCs) are a class of materials with the composition of transition metal from groups 4 -12 in the periodic table (such as Mo, W, T, Fe) and chalcogen elements (S, Se and Te). These compounds exhibit a diversity of electronic and quantum properties – varying from insulators such as $HfS_2$, semiconductors such as $MoS_2$, semimetals such as $WTe_2$, true metals such as $NbS_2$, to even low-temperature superconductor such as $TaSe_2$ and $NbSe_2$. [1, 2] The wide variety of elements and properties make the materials of great interest in fundamental and technological research including electronics, catalysis, energy storage and quantum materials research. Many transition metal chalcogenides adopt a layered structure. Typically, the transition metal atoms are arranged in one layer sandwiched between two layers of chalcogen atoms combined with chemical bonding. The bonded metal and chalcogen atoms form the metal chalcogenide sheets weakly combined by van der Waals forces. The organization of atoms in one layer results in different structure phases, mainly in *1T* octahedral or *2H* prismatic geometry in single or multiple layers. [3]

TMCs include three subsets according to the stoichiometry between the transition metal and the chalcogen elements: transition metal monochalcogenides, with the form of M*Ch* (M = Fe, Cu, Ag, etc; Ch = S, Se and Te), the widely-explored transition metal dichalcogenides (TMDs), with the form of $M\mathit{Ch}_2$ (M = Mo, W, Nb, Ta, etc.), and the less studied transition metal trichalcogenides (TMTs), with the form of $M\mathit{Ch}_3$(M = Nb, Ta, Ti, V, Cr, etc.). [4-8]

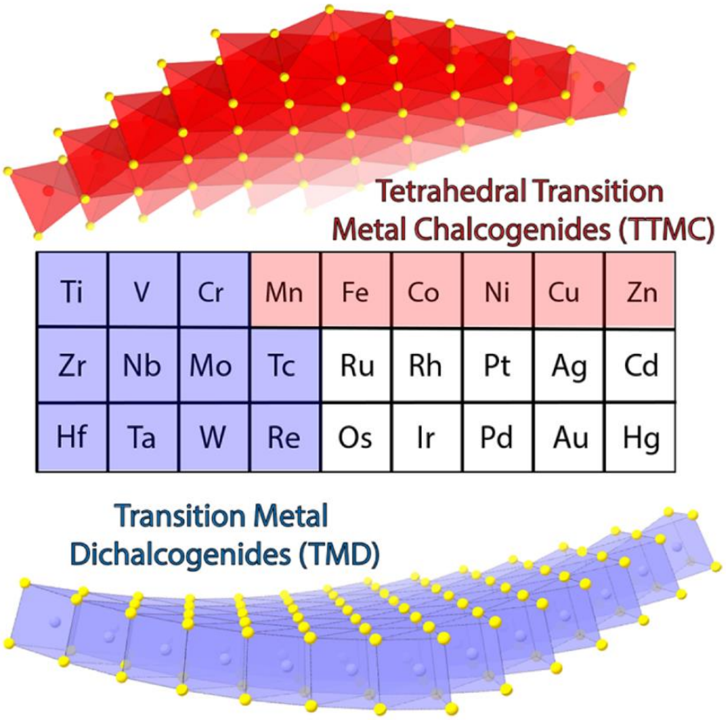

| | | | | | | | | |
|---|---|---|---|---|---|---|---|---|
| Ti | V | Cr | Mn | Fe | Co | Ni | Cu | Zn |
| Zr | Nb | Mo | Tc | Ru | Rh | Pt | Ag | Cd |
| Hf | Ta | W | Re | Os | Ir | Pd | Au | Hg |

Figure 1.1: Classification of transition metal chalcogenides (TMCs) based on crystal structure and transition metal identity. TMCs consist of transition metals (groups 4–12) bonded to chalcogen elements (S, Se, Te). A widely studied subclass is transition metal dichalcogenides (TMDs), which adopt layered hexagonal or trigonal structures based on octahedral (1T) or trigonal prismatic (2H) $MCh_6$ coordination units. These typically involve early transition metals (e.g., Mo, W, Nb, Ta). In contrast, tetrahedral transition metal chalcogenides (TTMCs) feature $MCh_4$ tetrahedral motifs within orthorhombic or tetragonal frameworks, favoring late 3d metals (Mn to Zn). [2]

In this dissertation, another way is chosen to sort the TMCs we discuss, depending on the crystal structure of these solid state materials since the crystal structure will affect the dimensionality of the electronic interactions of the layers. TMDs are comprised of hexagonal or trigonal crystal structures with a major structural motif of $M\mathit{Ch}_6$. Another species of TMCs are termed as tetrahedral transition metal chalcogenides (TTMCs), whose structures are tetragonal or orthorhombic with a major structural motif of $M\mathit{Ch}_4$.[2] The metal atoms in one layer of the chalcogenide sheet always form a 2D hexagonal net in TMDs, while TTMCs organize their metal atoms in a 2D square lattice. Compared to TMDs which prefer the early transition metals (mainly group 4 to 7) [9-14], TTMCs favor the late transition metal in the first row (that is Mn, Fe, Co, Ni, Cu and Zn) due to the small interstitial position of the tetrahedral site and therefore TTMCs are more electron rich than TMDs.[15-20]

Regardless of TMDs and TTMCs, their unique geometry offers opportunities for researchers to apply physical and chemical methods to modify the layer structures and improve or change the properties of the materials. One method is the exfoliation of these layered materials into mono- or few-layer sheets which largely maintain their properties and give rise to additional characteristics caused by confinement effect. Another approach is through intercalation chemistry which is mainly discussed in this dissertation.

## 1.2 Compound intercalation

In 1959, Rüdorff first used the phrase "intercalation compound" to discuss about the chemical derivatives of graphite and since then, researchers begin to extend the concept of intercalation to a broader range of layered-structure materials.[21] Generally, intercalation is defined as the insertion process of guest species into the vacant sites of host materials. The crystal structure of the host does not change significantly before and after intercalation.[22] Potential materials for intercalation consist of structural elements like channels and cavities with a diameter of 3-11 Å (for example, zeolites) or chains and layers combined together by weak van der Waals forces. [23-25] Compared with a densely packed solid, these elements result in much more unoccupied lattice sites for higher mobility of the inserted chemicals, and therefore permits intercalation synthesis in relatively lower temperature (about 100 to 200 °C) and even in room temperature, which enable the production of compounds which are unstable at high temperatures (more than 500 °C). The weak interaction between layered or chain structure brings another advantage that they can expand in one or two dimensions without serious restrictions, which allows the insertion of relatively large molecules or ions such as metal complexes and organic cations. The layered host has a more stable structure than the one-dimensional chains. The additional intercalants weaken the interaction between the chains and layers. In many cases, this weakening is enough to disintegrate the chain-structured solids. Nevertheless, the two-dimensional structure can still stabilize the layers to avoid the disintegration. Therefore, layer-structured compounds are more favored for intercalation study due to both easy synthesis and comparatively stable final products. If the gaps between the layers are not expanded too largely after intercalation, the topological relationship between the host materials and their intercalated products are almost preserved, indicating that the original stacking sequence of the host remains unaffected by the intercalation process. [26-29]

Plenty of intercalation techniques have been developed for the synthesis and applications of those inserted layer materials based on the driving force of the techniques and the involved intercalation kinetics.[30] For instance, electrochemical intercalation is widely applied for tuning the electronic, optical, and structural properties of layered materials as well as in energy storage applications such as Li-ion batteries. [31-39] Electrochemical potential created by external voltage is the driving force of the technique. In some cases, therefore, different stages of the intercalation corresponding to different stacking sequences of the intercalant layers can be more precisely controlled by adjusting the voltage to modulate the properties of the final product. However, this technique is not suitable for insulating materials and intercalants without charges due to their low electrical conductivity. The host materials need to play the role of anode if the guest species are

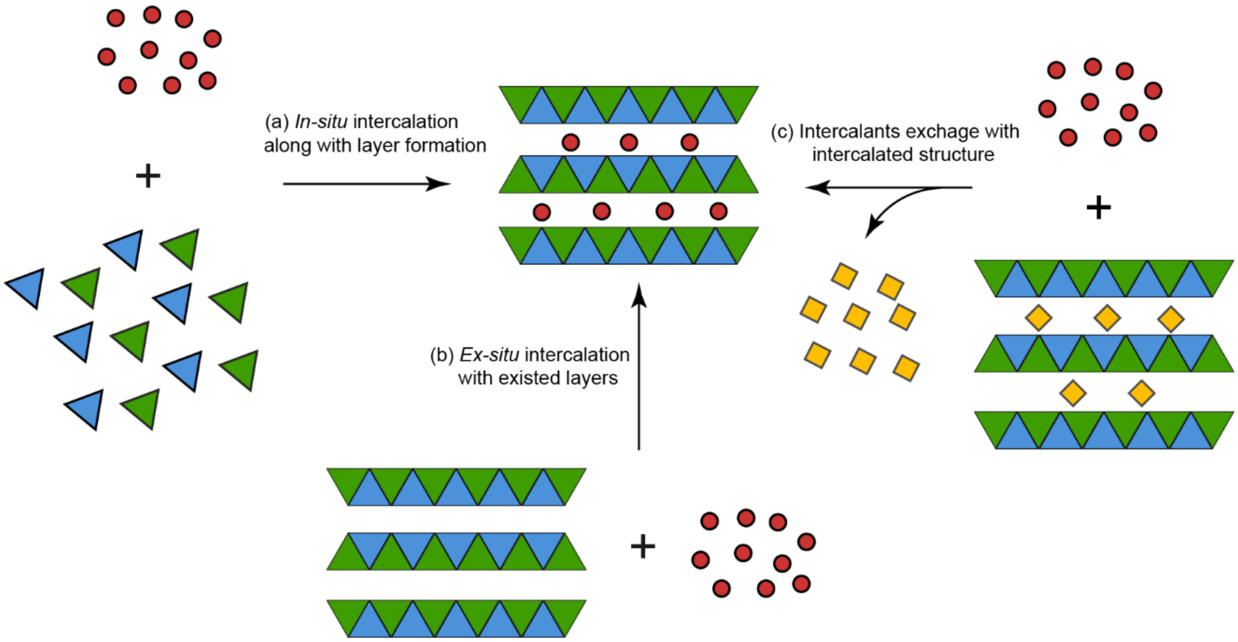

Figure 1.2: Three approaches of intercalation in synthesis based on the starting materials. a) *in-situ* intercalation together with the formation of layered structures, starting from element materials. b) ex-situ intercalation with existed layers. C) intercalant exchange with intercalated structures.

negatively charged or cathode if guest species are positively charged. In addition, some guest ions have a chance to oxidize or reduce after applying external voltage before the intercalation begins.

Another technique is gas-phase intercalation especially when intercalants are in vapor form. This method has been widely used to insert alkali metals, halogens, and other gaseous species into graphite, TMDs, and other 2D materials. There are typically two categories of gas-phase intercalation. [40] One is isothermal vapor intercalation, where the host materials and the guest particles are kept at the same temperature. This method usually provides uniform intercalation, but the control of the levels of the intercalation could be difficult. To overcome such problems, two-zone vapor transport intercalation is applied. The intercalant source and the host materials are kept in separate temperature zones, which can also improve the intercalation efficiency. Since vapors are involved in the synthesis through such technique, the reaction systems require vacuum or inert gas to prevent unwanted reactions from air, which increases the difficulty of the setup establishment and limits the reaction scalability for large-area material processing. [41-48]

If the intercalants are liquid themselves or soluble in certain solvents, the straightforward wet chemical intercalation can be considered as the method to insert those species into the hosts by directly placing the host materials in the liquid containing intercalants at a controlled temperature. The guest materials vary widely from inorganic ions ($Li^+$, $Na^+$, $Cu^{2+}$, etc.), organic molecules (amines, hydrazine, pyridine), and even zero-valent metals (Cu, Ag, Co, etc.).[49-56] The intercalants may spontaneously diffuse into the layered host due to electrostatic interaction that can overcome the van de Waals force between the layers. A famous example of wet chemical intercalation is Li intercalation by immersing the hosts in the active alkyl lithium (n-butyl or tert-butyl lithium) since Li atom favors to donate electron. n-Butyl lithium intercalation in $MoS_2$, $WS_2$ and graphite enables high-quality monolayer nanosheets for battery and optoelectronic applications. The organic molecules follow Lewis acid-base interactions, where organic molecules also donate electrons to TMDs. A brief way to determine whether the organic compounds can serve as a stable intercalants is to check their $pK_a$. Generally, organic molecules with $pK_a > 4$ form stable intercalation compounds while those with $pK_a < 3$ do not. Among those charge transfer, our group has proven evidence that the weak hydrogen bonding could likewise be a driving force in amine intercalation chemistry and help stabilize the intercalated layered structure.[51] When a strong hydrogen donor like O—H or N—H is interacted with a weak acceptor, a non-conventional or "weak" hydrogen bond can occur.

## 1.3 Hydrogen Bonding

Pauling (1935) was the first chemist to apply the term "hydrogen bond" freely to account for the residual entropy of ice. In his following work *the nature of the chemical bond* (1939), Pauling stated unambiguously that if an hydrogen atom is attracted by relatively strong forces of two other atoms instead of one under certain conditions, it may be considered the forces act as a bond between them.[57] In a configuration of X—H···A, the hydrogen atom plays the role as the bridge of the two other atoms. Besides, the second core idea from the work is that the hydrogen bond is an electrostatic interaction because the H atom can only form one covalent bond with only one stable orbital. Pauling presumed that only under the condition that X and A are very electronegative, would the interaction be termed a hydrogen bond when the H atom is sufficiently deshielded to produce rather strong electrostatic attraction between H and A. Accordingly, X and A would be restricted as the following elements: F, O, Cl, N, Br and I. Such an opinion is still widely accepted and applied in nowadays general chemistry textbooks. [58-60] In 2011, International Union of Pure and Applied Chemistry (IUPAC) defines hydrogen bonds as "The hydrogen bond is an attractive interaction between a hydrogen atom from a molecule or a molecular fragment X—H, in which X is more electronegative than H, and an atom or a group of atoms in the same or a different molecule, in which there is evidence of bond formation. [61] This definition is consistent with Pauling's idea that X in X—H must be more electronegative than hydrogen and also implies that hydridic hydrogen bonds, where H is bonded to electropositive elements, are not explicitly included.

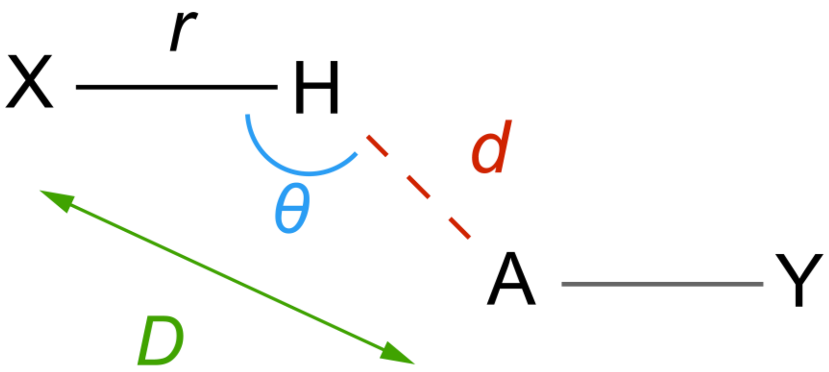

Figure 1.3: The general structure of a hydrogen bond with geometrical parameters $d$, $D$, $r$, $\theta$ and $\varphi$, where X—H is the donor and A is the acceptor.

However, back in 1960, Pimentel and McClellan further developed the both core ideas of hydrogen bonding and gave the modern definition of the phenomenon for the first time: A hydrogen bond is said to exist, when (1) There is evidence of a bond; and (2) there is evidence that this bond sterically involves a hydrogen atom already bonded to another atom. [62] It is noticeable that in this definition, there is no specific requirement for the nature of atom A and X. Therefore, the concept of hydrogen bonding can further evaluate to include more diverse groups like S—H, C—H. This definition makes the concept of hydrogen bonding more universal and is also important to understand the hydrogen interaction of metal chalcogenides in this dissertation.

The general hydrogen bond consists of a donor X—H and an acceptor A. Figure 1.2 shows the geometrical parameters a hydrogen bond has. In a crystallographic view, the most frequently applied parameters are $\theta$, $d$ and $D$. Table B1 gathers relevant structural parameters for hydrogen bonds including S or Se as acceptors and O–H or N–H as donors in some organic compounds. Although there will be still some differences, this survey enlightens our understanding when hydrogen bonding occurs in our metal chalcogenides.

Table 1.1. Mean values for over 700 organic structures contaiong the hydrogen bond to S or Se. Study by Allen *et al*. [58]

| Type | $d$ (Å) | $D$ (Å) | $\theta$ (°) |
|---|---|---|---|
| O–H· · · S | 2.67(1) | 3.39(1) | 134(1) |
| N–H· · · S=C | 2.51(1) | 3.43(1) | 157(1) |
| N–H· · · S | 2.75(1) | 3.58(1) | 142(1) |
| N–H· · · Se | 2.38(1) | 3.30(1) | 153(1) |

From the crystallographic studies of ($Li_{1-x}Fe_xOH$)FeS, the relevant O—H · · · S interaction in the structure point towards hydrogen bonding. [63] The N—H donor is also proven to be effective at hydrogen bonding.[13] Unlike Clarke’s work where both alkali metal cations and ammonia molecules are intercalated into the gap of layered FeSe, our group succeeded in finding an ammonia intercalation route which is free from alkali metal co-intercalation. Instead of pursuing a top-down intercalation synthesis of Fe*Ch* (*Ch* = S, Se) in liquid ammonia, our group carried out a bottom-up synthesis where FeCh sheets were built under hydrothermal conditions and resulted in compound $(H_{0.5}NH_3)FeCh$. Through a deuterated process in $(H_{0.5}NH_3)FeS$, it was surprising to find that within the gallery of FeS, $NH_3$ molecules and $D^+$ protons were observed instead of $NH_4^+$ cations. The proton in $(H_{0.5}NH_3)FeS$ was in equal distance between two $S^{2-}$ anions and the ammonia molecules was directed towards the $S^{2-}$ in the layers to form hydrogen bonding. In Table 1.2, some data of interaction between hydrogen donors and acceptors in layered iron chalcogenides are collected. Comparing with Table 1.1, it is not difficult to make a compelling argument for hydrogen bonding in these layered materials.

Table 1.2 Parameters involving hydrogen for several intercalated Fe*Ch* [63-66]

| Compounds | Type | $d$ (Å) | $D$ (Å) | $\theta$ (°) |
|---|---|---|---|---|
| $(Li_{0.8}Fe_{0.2}OH)FeSe$ | O–H· · · Se | 3.072 | 3.635 | 119.6 |
| $Li_x(NH_2)_y(NH_3)_{1-y}Fe_2Se_2$ | N–H· · · Se | 2.725 | 3.721 | 174.2 |
| $Na_x(C_2N_2H_8)_yFe_2Se_2$ | N–H· · · Se | 2.784 | 3.553 | 159.1 |
| $[Fe(en)3]_2Fe_{16}S_{20}$ | N–H· · · S | 2.65-2.82 | 3.53-3.73 | 161.6-170.0 |
| $(H_{0.5}NH_3)FeS$ | N–H· · · S | 2.578 | 3.556 | 170.9 |

## 1.4 Hydrothermal and solvothermal reactions

Among those wet chemical intercalation with TMCs, the technique of hydrothermal synthesis is widely applied. The term hydrothermal origins purely from geological science. It was first introduced by Sir Roderick Murchison in the 19th century to describe the role of water in geological transformations.[67] The concept of hydrothermal synthesis is deeply inspired by natural hydrothermal vents found along ocean ridges. In these geological settings, seawater is superheated by volcanic activity to temperatures exceeding 400 °C, dissolving metal ions and facilitating the precipitation of minerals like iron sulfides and manganese oxides upon cooling. [70] These vents act as natural high-pressure chemical reactors and are essential for sustaining unique deep-sea ecosystems. Laboratory hydrothermal methods aim to replicate these extreme yet productive environments to synthesize complex inorganic materials under controlled conditions. Early hydrothermal experiments were conducted by Robert Bunsen (1839) and Schafthaul (1845), leading to the first artificial quartz crystal synthesis. Karl Josef Bayer (1892) developed the hydrothermal bauxite leaching process, which remains the primary method for aluminum extraction.[68,69] During World War II, the demand for large quartz crystals led to extensive research in hydrothermal crystal growth.

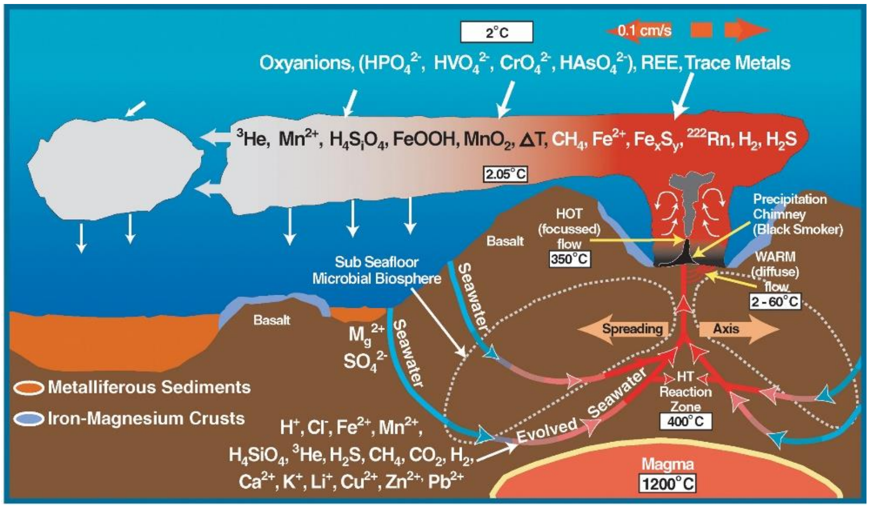

Figure 1.4: Illustration of a natural hydrothermal system at a mid-ocean ridge, highlighting the key geochemical processes that inspire laboratory hydrothermal synthesis. Seawater infiltrates oceanic crust and is heated by magma to temperatures up to 400 °C in the high-temperature (HT) reaction zone. This results in extensive leaching of metal ions (e.g., $Fe^{2+}$, $Mn^{2+}$, $Cu^{2+}$, $Zn^{2+}$) and the formation of mineral-laden hydrothermal fluids. Upon venting, rapid cooling and redox changes lead to precipitation of metal sulfides and oxides, mimicking the conditions used in hydrothermal autoclaves for controlled crystallization. The diagram also illustrates the chemical gradients (temperature, pH, redox, solute concentration) that govern phase stability, crystal growth, and material deposition—principles directly relevant to hydrothermal materials synthesis. [71]

Like hydrogen bonding, the definition of hydrothermal technique has evolved over time and still does not reach unanimity.[72-77] In general, hydrothermal refers to heterogeneous chemical reactions occurring in aqueous solvents under high-pressure and high-temperature (HPHT) conditions. [81] The slightly different criteria of the definition is based on temperature, pressure and reaction environment. A hydrothermal reaction typically involves: 1)Water acting as a reaction medium; 2) Elevated temperature (usually >100°C) to facilitate solubility and reaction kinetics; 3) Elevated pressure (>1 atm), often generated in a sealed system, to maintain the solvent in a liquid or supercritical state; and 4) Dissolution and recrystallization of materials that are otherwise insoluble under normal conditions. Hydrothermal reactions are widely used for material synthesis, crystal growth, and mineral formation, often mimicking natural geological processes. For example, hydrothermal used to produce high-quality nanocrystals with controlled size and morphology like metal oxides ($TiO_2$, $Fe_3O_4$, etc.) or enables low temperature fabrication of piezoelectrics, ferroelectrics, and superconductors in TMCs. However, some of the above products are synthesized in a even lower temperature or pressure and the solvents as the reaction medium is not water anymore. Considering the expanding role of hydrothermal technology, researchers now suggest a broader definition: Any heterogeneous or homogeneous chemical reaction occurring in the presence of a solvent (whether aqueous or nonaqueous) above room temperature and at a pressure greater than 1 atm in a closed system. Nevertheless, given the prefix hydro- refers to water-related concept, chemists favor to use a broader term solvothermal to describe the reaction especially when the liquid medium is not water. Depending on the specific solvents, several other terms such as glycothermal, alcothermal, ammonothermal, lyothermal, carbonothermal, are invented to more precisely describe the hydrothermal conditions in special circumstances.[77]

When subjected to high temperature and pressure, those solvents exhibit unique physical and chemical properties that make it an effective reaction medium for hydrothermal synthesis. The dielectric constant (ε) of water, for example, drops as temperature increases, making it behaves more like an organic solvent (e.g., alcohols or acetone). [79] This allows it to dissolve non-polar organic molecules and metal oxides, which are normally insoluble in water at room temperature. At supercritical conditions (T > 374°C, P > 22.1 MPa), water transitions into a state with gas-like diffusivity and liquid-like density, leading to enhanced mass transfer and reaction rates. At hydrothermal condition, the solubility of solids and minerals in water also enhance. High-temperature water dissolves metal oxides, silicates, and carbonates by forming hydroxo- and fluoro-complexes (e.g., $Si(OH)_4$, $Al(OH)^-_4$). Some other chemical properties of water may change as well. The ionization constant of water ($K_w$) increases with temperature, making hydrothermal water behave as a stronger acid and base since the concentration of both $H^+$ and $OH^-$ increase. This enhances acid-catalyzed and base-catalyzed reactions, making it effective for oxide dissolution and mineral precipitation. Under supercritical conditions, water becomes a highly reactive oxidant due to the increased availability of OH· radicals. This property is exploited in supercritical water oxidation (SCWO) to decompose hazardous organic wastes efficiently.[76,80]

TABLE1.3 Viscosity (η), dielectric constant(ε) and density (ρ)of water in high temperatures. [79]

| Temperature (°C) | η (mPa) | ε | ρ (g $cm^{-3}$) |
|---|---|---|---|
| 25 | 0.890 | 78.3 | 0.997 |
| 200 | 0.136 | 35.1 | 0.871 |
| 250 | 0.108 | 27.4 | 0.806 |
| 300 | 0.087 | 20.4 | 0.715 |
| 350 | 0.022 | 1.2 | 0.045 |
| 400 | 0.025 | 1.2 | 0.038 |
| 450 | 0.027 | 1.1 | 0.024 |

Mineralizers play a crucial role in hydrothermal reactions, acting as solvents, catalysts, and transport agents in hydrothermal synthesis. [84] They can increase the solubility of sparingly soluble compounds by forming soluble complexes, and control the morphology, phase, and size of crystals during hydrothermal growth. Also mineralizers enable low-temperature synthesis of metastable phases that are difficult to obtain via conventional solid-state reactions. Complexation occurs when mineralizers form soluble complexes with metal ions, increasing their solubility and transport. For example, $SiO_2$ dissolves in HF via the formation of $SiF_6^{2-}$, enabling quartz crystal growth. pH control is another crucial function, where some weak acidic salts like $NH_4Cl$ decrease the pH and therefore help oxidize metals to their ions. Alkaline mineralizers like NaOH and KOH dissolve oxides and hydroxides, enhancing crystal growth. This is evident in the synthesis of $YBa_2Cu_3O_7$ (YBCO) superconductors, where NaOH helps dissolve CuO and $Y_2O_3$, facilitating phase formation. Additionally, redox regulation plays a vital role, with nitrates and sulfates acting as oxidizers to stabilize specific oxidation states, such as $Fe^{3+}$ in ferrite synthesis, ensuring controlled magnetic properties. Finally, selective precipitation occurs when carbonates and phosphates induce the crystallization of specific metal cations, controlling phase purity. An example of this is the hydrothermal growth of hydroxyapatite (HAp), where phosphate-based mineralizers help form the desired phase. These mechanisms collectively influence solubility, phase control, and reaction kinetics, making mineralizers essential in hydrothermal synthesis.[79]

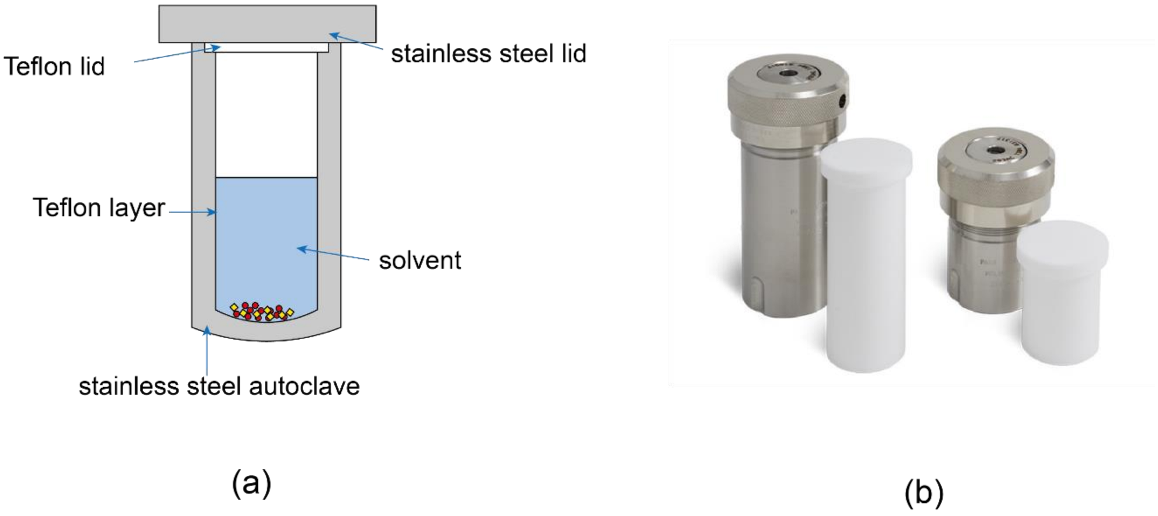

Figure 1.5: (a) Schematic of a typical Teflon-lined stainless steel autoclave used in hydrothermal synthesis. (b) Commercially available Parr-style 47 mL and 25 mL autoclaves and their corresponding Teflon liners.[83]

The apparatus of hydrothermal or solvothermal reactions is usually termed as autoclave or bomb. The choice of an autoclave depends on temperature, pressure, and corrosion resistance in a given solvent. Common materials for autoclave include stainless steel, nickel-based superalloys and titanium alloys, and liners and coatings (such as Teflon, silver, platinum) are used to protect autoclaves from corrosive solvents. [86] Teflon (PTFE) lined stainless steel autoclaves are one of the most popular apparatus in local laboratory hydrothermal synthesis, especially in corrosive environments where traditional metal autoclaves can degrade. These autoclaves offer chemical resistance, ease of use, and compatibility with a wide range of solvents. The outer stainless steel body of the autoclaves provides structural strength to withstand high pressures (up to 250 bar) and temperatures (~300°C), and the inside Teflon liner are chemically inert to protect the steel body against acidic, basic, and oxidative solutions involved in the hydrothermal reactions. Steel discs and springs are applied for pressure balance and protect the body from leaking incident. Some designs use a sharp ring-like sealing mechanism, where Teflon expands under heat to create a hermetic seal. The smooth non-stick surface of Teflon ensures samples do not adhere to the liner and make the recovery of the samples less difficult. Compared to those noble metal-lined (platinum, gold) autoclaves, Teflon and steel are more affordable materials. However, Teflon starts to degrade and releases fluorinated compounds above 300 °C, which indicates that the hydrothermal reaction with Teflon liner is limited to a relatively low temperature. Besides, Teflon is soft and prone to deformation under prolonged high pressure conditions. Due to the porous structure of Teflon, some solvent residue can stay in the liner wall although the liner is thoroughly cleaned. [79] Therefore, Teflon liners have a lifetime and has to be replaced with a new one after certain cycles of reaction running or when a new sort of solvent is decided to be used in the reaction.

## 1.5 Objective and outline

This chapter introduces the background and the motivations of the experiments in the dissertation. The work focuses on the synthesis, structure analysis and measurement of physical properties.

In Chapter 2, we discuss the synthetic and characterization methods applied throughout the work in the dissertation.

In Chapter 3, we describe several amine intercalations into TTMCs such as FeS, CoS and FeSe through solvothermal methods. Particularly, a rare polar metal is synthesized through solvothermal method. We discuss its crystal structure and electron structure. The metal−amine complex Co(en)3, where en =ethylenediamine, intercalates between layers of cobalt sulfide (CoS) to form a polar, ferromagnetic metal. We solve the structure of the hybrid compound [Co(*en*)3](CoS)12·*en* in the polar group $Pca2_1$ with lattice parameters $a$ = 14.778(3) Å, $b$ = 11.066(3) Å, and $c$ = 20.095(5) Å using single-crystal X-ray diffraction. The $[Co(en)_3]^{2+}$ complexes order between CoS layers and break their inherent fourfold symmetry. Moreover, the chiral $Co(en)_3$ complexes hydrogen bond to the terminal sulfides of the layers and break inversion symmetry, thereby inducing a polar state. The shortest hydrogen bond of the amino group is H···S = 2.41(1) Å. From 1.8 to 300 K, the title compound displays metallic electrical resistivity and an anomaly at 43 K. Through magnetization measurements, we find that $Co(en)_3$ exhibits spontaneous ferromagnetic order below 43 K. First-principles calculations reproduce the ferromagnetic structure and illustrate decoupling between the conducting electrons and the inversion-lifting distortion. Our work shows that hybrid materials created from intercalation chemistry of functional 2D hosts provides a pathway for uniting contraindicated properties.

In Chapter 4, we describe chiral amine intercalations into two TMDs $NbSe_2$ and $TaSe_2$ through solvothermal methods. The synthetic strategy and superconductivity of non-chiral and chiral amine intercalated $TaSe_2$ is mainly discussed. We found that the rigid methylbenzylamine

(MBA) molecules are far more challenging to be intercalated into the layers compared with smaller and more flexible ethylenediamine molecules. However, with a trace amount of ethylenediamine, the intercalation of MBA becomes possible. We used circular dichroism and thermogravimetric analysis to demonstrate that the MBA intercalation with the existence of ethylenediamine is a co-intercalation process, with ethylenediamine playing a role of intercalation lubricants. Through magnetic susceptibility study, we learnt that the intercalation of ethylenediamine increases the critical temperature of $TaSe_2$ from below 1 K to ~5.2 K, and the chiral molecule R-MBA can further increase to ~7 K. However, resistance measurement failed to show corresponding results, possibly because the samples are pellet pressed from powders instead of sample crystals.

In Chapter 5, we employed in-situ synchrotron powder X-ray diffraction to monitor the real-time crystallization of layered Fe- and Co-based chalcogenides under hydrothermal and solvothermal conditions. Eight reactions, spanning bottom-up and top-down strategies, were systematically examined to elucidate how precursor chemistry, solvent properties, and redox environment influence phase evolution and lattice dynamics. Hydrothermal systems, especially those based on LiOH and $NH_4^+$, displayed rapid transformation and well-defined intermediate or templated structures, while solvothermal systems using ethylenediamine or 1,2-diaminopropane exhibited markedly slower kinetics and more complex coordination competition. Time-resolved lattice parameter tracking revealed distinct crystallization mechanisms—including synchronous framework growth and stepwise intercalation—highlighting the influence of ion size, solvent viscosity, and chelate geometry. Comparisons across systems uncovered general principles governing layered chalcogenide formation, and provided predictive insight for accessing metastable or polar intercalated phases via soft chemical routes.

Chapter 6 summarizes the key findings of this dissertation and outlines potential directions for future research informed by these results.

# Chapter 2: Methods

## 2.1 Synthetic Methods.

In this section, we will only discuss the general approaches of the amine intercalation into the tetragonal transition metal chalcogenides (TTMCs, i.e. FeS, FeSe, CoS and CoSe) and the transition metal dichalcogenides (TMDs, i.e. $NbSe_2$ and $TaSe_2$) through solvothermal reactions. More specific details of the synthesis will be described in the experimental sections of the respective chapters.

### 2.1.1 *In-situ* intercalation

The amine intercalated iron chalcogenides and cobalt chalcogenides can be prepared using a solvothermal based in-situ method, or so-called bottom-up method, starting from the element materials involved in the products with some modulation of the condition of the the synthetic conditions, such as temperature and reaction time. For a typical reaction, Fe or Co metal powder, a chalcogen source (such as sulfur powder, selenium powder, thiourea and selenourea) and a mineralizer $NH_4Cl$, will be mixed with certain amine (ethylenediamine, 1,2-diaminopropane, 1,3-diaminopropane, 1,2-diaminocyclohexane) in a Teflon-liner stainless steel autoclave in a glove box to ensure an inert atmosphere in the autoclave. The sealed mixture is heated to 140 to 200 °C for 3 to 7 days. Black polycrystals or single crystals of the product will be found after washing with the same amine as in the reactions.

For the iron-based amine intercalated product, the reaction favors a higher temperature about 180 to 200 °C for better product crystallinity. However, the cobalt based amine intercalated product has to be at a relatively lower temperature below ~150 °C. The previous research in our group has found out that Co will react with chalcogens to form cubic bulk structure $Co_9Ch_8$ above 150 °C instead of layer-structure materials.[85]

Although the amines used in the experiments are reagent-grade pure, there will inevitably be water impurity in these liquids due to the process of industrial production. $NH_4Cl$, as an acidic salt, can therefore still decrease the pH of the solvothermal reaction system and help dissolve iron or cobalt metal. The amines are expected to serve as the guest species into the gaps between the layers. However, they are also good ligands which are prone to combine with the transition metal to form complex cations With $NH_4Cl$ to provide $Cl^-$ anion, complex salts can likewise be synthesized as a side product. In the cobalt-based product, white crystals of $Co(diam)_3Cl_2$ (diam = ethylenediamine, 1,2-diaminopropane, 1,3-diaminopropane, 1,2-diaminocyclohexane) have been found among the main dark product. Nevertheless, iron complex salts are not found in the product of iron-based amine intercalated synthesis, because the iron complex salts have a higher solubility in the respective amine solvents than their cobalt analogues.

### 2.1.2 *Ex-situ* intercalation.

The chiral amine intercalated niobium dichalcogenides and tantalum dichalcogenides can be prepared using a solvothermal based *ex-situ* method, or so-called top-down method. The starting materials include 2H $NbSe_2$ and 2H $TaSe_2$ which are already layered structure materials. The chiral amines include the pair of (*R*) -(+)-α-methylbenzylamine (R-MBA) and (*S*) -(-)-α-methylbenzylamine (S-MBA), as well as the pair of trans-1,2-diaminocyclohexane (trans-1,2-dach) and cis-1,2-diaminocyclohexane(cis-1,2-dach). Nonchiral amine ethylenediamine and the racemic solvents of methylbenzylamine (MBA) and diaminocyclohexane (1,2-dach) are also applied for comparison. For a typical reaction, the polycrystals of pre-synthetic 2H $NbSe_2$ and 2H $TaSe_2$ are mixed with certain amine mentioned above in a Teflon-liner stainless steel autoclave in an argon atmosphere glove box and then sealed. The autoclave is heated to120 °C for 2 to 5 days.

## 2.2 X-ray diffraction.

X-rays are a form of electromagnetic radiation with wavelengths between approximately 0.1 to 100 Å, falling between gamma rays and ultraviolet light in the spectrum. They are generated whenever electric charges undergo acceleration or deceleration. X-rays are commonly used in crystallography due to their wavelength being comparable to interatomic distances, making them ideal for studying atomic structures. There are two main methods of generating X-rays. The first one relies on X-ray tubes, where high-energy electrons impact a metal target, emitting X-rays. They are widely available but have limitations in brightness. Such tubes are the simplest and are available in a laboratory of any size and therefore serve as the conventional laboratory X-ray source. The other one is synchrotron radiation sources. These produce extremely bright X-ray beams by accelerating electrons in a circular orbit, controlled by a magnetic field. Synchrotron sources offer high intensity and tunable wavelengths, making them valuable for advanced diffraction studies.

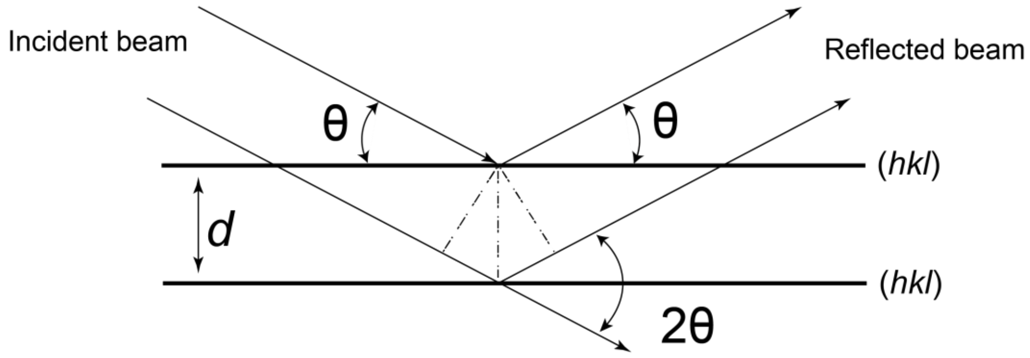

Figure 2.1: Schematic illustration of Bragg's Law for X-ray diffraction from a crystalline material.

When X-rays interact with free electrons, they cause elastic scattering, generating a new wave of the same frequency. This scattering is described by Thomson scattering and forms the basis for understanding how X-rays interact with materials. In X-ray powder diffraction, the intensity of scattered X-rays is proportional to the sum of Thomson scattering contributions from all electrons in the crystal. This explains why heavy elements scatter X-rays more strongly—they have more electrons contributing to the scattering. The atomic scattering factor (f) quantifies an atom's ability to scatter X-rays as a function of diffraction angle. In a crystalline lattice, diffraction peaks only occur at specific angles, forming the basis for X-ray crystallography. Bragg's Law developed by W.H. Bragg and W.L. Bragg describes the conditions for constructive interference in crystal diffraction:

$$n\lambda = 2d\sin\theta \tag{2.1}$$

where $d$ is the interplanar spacing of the crystal, θ is the angle of incidence or Bragg angle, n is an integer, the order of the diffraction, and $\lambda$ is the wavelength of the incident X-ray.

### 2.2.1 Laboratory Powder X-ray diffraction

Powder X-ray diffraction (PXRD) arises when X-rays interact with a polycrystalline sample, where numerous randomly oriented grains contribute to scattering, leading to diffraction in concentric cones known as Debye-Scherrer rings. The diffraction pattern is a one-dimensional projection of a three-dimensional reciprocal lattice, containing structural information about the material. The Bragg reflections in a powder pattern provide information on the crystal structure, unit cell parameters, and symmetry. Powder diffraction data are plotted as intensity vs. diffraction angle (2θ).  A powder diffraction pattern consists of Bragg reflections superimposed on a background. The three main components of the pattern are: 1) peak positions which provide unit cell parameters, 2) peak intensities which reveal atomic positions and thermal vibrations, and 3) peak shapes which indicate crystallite size, strain, and instrumental broadening. There are also background effect caused by instrument noise, sample fluorescence or amorphous phases to be considered.  Peak positions are mainly determined by unit cell dimensions and Miller indices (*hkl*). Temperature variations can cause thermal expansion, which may also shift peak positions. The strain and stress of the crystal can lead to peak broadening and asymmetry. Besides, sample displacement and instrument alignment introduce systematic peak shifts and then cause error and inaccuracy to the peak position. The characteristic peaks can help facilitate phase identification by comparing the data from automated databases such as International Center for Diffraction Data (ICDD) or Inorganic Crystal Structure Database (ICSD). The lattice parameter refinement can precisely determine the unit cell dimensions.

Lattice parameter refinement is a crucial step in X-ray powder diffraction (XRD) analysis, used to determine precise unit cell dimensions. It involves minimizing the differences between observed and calculated Bragg peak positions with considering systematic errors, such as zero-shift and sample displacement errors. Both the Pawley and Rietveld refinement methods are widely used in X-ray powder diffraction analysis for extracting structural information. Both techniques involve least squares fitting of calculated diffraction profiles to experimental data but differ in their approach to handling integrated intensities. The purpose of Pawely refinement is to extract peak positions, shapes, and intensities without assuming a structural model. It uses a full pattern decomposition approach to fit peak intensities and requires a known unit cell. The integrated intensities are treated as independent least squares variables. This method is not only useful for indexing and preliminary phase identification, but also can refine unit cell parameters and peak shape without structure bias. However, since Pawley refinement does not require an atomic model, it can not provide information about atomic positions or structure factors. When the peaks overlap to each other, this method will have more errors and require careful constraints. Rietveld refinement, on the other hand, analyze a full structural model, including atomic positions, to offer a more detailed crystallographic information, and therefore requires a reasonable initial structure model for accurate results. It uses profile fitting with a non-linear least squares approach. The method refines lattice parameters, peak shape, atomic positions, site occupancies, thermal vibrations, and background correction and explain peak overlap, preferred orientation, and instrumental effects in the data. [88]

In our work, room temperature powder X-ray diffraction data were collected on a Bruker D8 X-ray diffractometer ($\lambda$ = 1.5418 Å, with Cu $K_\alpha$ radiation as the X-ray source) at X-ray Crytallographic Center (XCC) in University of Maryland. For a routine quick measurement to identify the phases, the PXRD data were scanned with a step size of 0.02° from 5° to 70° in a Poly(methyl methacrylate) (PMMA) holder, usually taken about 15 minutes. The data for further Rietveld refinement were collected with a step size of 0.01°. All crystallographic analyses were carried out with the Brucker software suite. Bruker Diffrac. Suite TOPAS 5 was used for Lebail/Pawley and Rietveld refinements.

### 2.2.2 Single crystal X-ray diffraction

Experimentally, a suitable single crystal was selected and measured on a Bruker Smart Apex II CCD diffractometer or Bruker D8 Venture Duo single crystal diffractometer. The crystal was kept at 150(2) K during data collection. The integral intensity were correct for absorption using SADABS software using integration method. Resulting minimum and maximum transmission are 0.453 and 0.951 respectively. The structure was solved with the ShelXT (Sheldrick, 2015a) program and refined with the ShelXL (Sheldrick, 2015c) program and least-square minimization using ShelX software package. Number of restraints used in the experiments was 138.

### 2.2.3 Synchrotron X-ray diffraction

Synchrotron X-ray diffraction (SXRD) is a powerful technique that utilizes high-brilliance X-ray beams produced in synchrotron facilities to achieve high-resolution diffraction patterns. This method is essential for studying crystal structures, phase transitions, and materials under extreme conditions. The X-ray beam is generated by accelerating electrons or positrons in a circular orbit using magnetic fields at relativistic speeds. The emitted radiation is highly coherent, intense, and tunable, allowing researchers to select specific wavelengths for diffraction experiments. SXRD has much higher brilliance, up to twelve orders of magnitude more intense than conventional X-ray tubes. The parallel beam of SXRD reduces beam divergence and improves angular resolution. The facility of SXRD can provide time-tracking experiments, or *in-situ* X-ray diffraction experiments, which allows researchers to track the structural change in materials in real time.

## 2.3 Neutron diffraction.

The theoretical prediction that neutrons could be diffracted by crystals was first made by Elsasser (1936). The first experimental confirmations were conducted by Halban & Preiswerk (1936) and Mitchell & Powers (1936) using neutron sources from radium-beryllium reactions. The practical use of neutron diffraction expanded significantly with the advent of chain-reacting nuclear reactors, which provided a high flux of thermal neutrons. [89]

Neutron diffraction is an essential technique in crystallography and material science, as an important complementary to XRD. Neutrons are uncharged particles, which allows them to penetrate deeply into materials without significant absorption or scattering by electrons. Their wavelength is comparable to atomic spacing in crystals (1–2 Å), making them suitable for diffraction experiments. Neutrons interact primarily with atomic nuclei, rather than electron clouds, making their scattering properties fundamentally different from X-rays. The scattering function of neutrons is constant across Bragg angles, unlike X-rays, where it depends on atomic number. Since neutron scattering varies by isotope which have distinct neutron scattering lengths, it enables isotopic substitution studies, which are useful in hydrogen-containing materials and also distinguish elements with similar atomic number.[88] Also, Neutrons can effectively detect light elements such as hydrogen, lithium, and boron, which do not have sufficient electrons for X-ray diffraction and are nearly invisible to X-rays, This makes neutron diffraction a powerful tool for hydrogen bonding study. Neutrons behave as quantum mechanical waves, with their wavelength given by:

$$\lambda = \frac{h}{mv} \tag{2.2}$$

where $h$ is Planck's constant, $m$ is neutron mass, and $v$ is velocity. Thermal neutrons (energy ~ 0.025 eV) have a wavelength of 1–2 Å, which matches typical interatomic distances in crystals. The relatively low frequency of neutrons (~$10^{13}$ Hz) aligns with thermal vibrations in solids, making neutron scattering valuable for phonon studies.

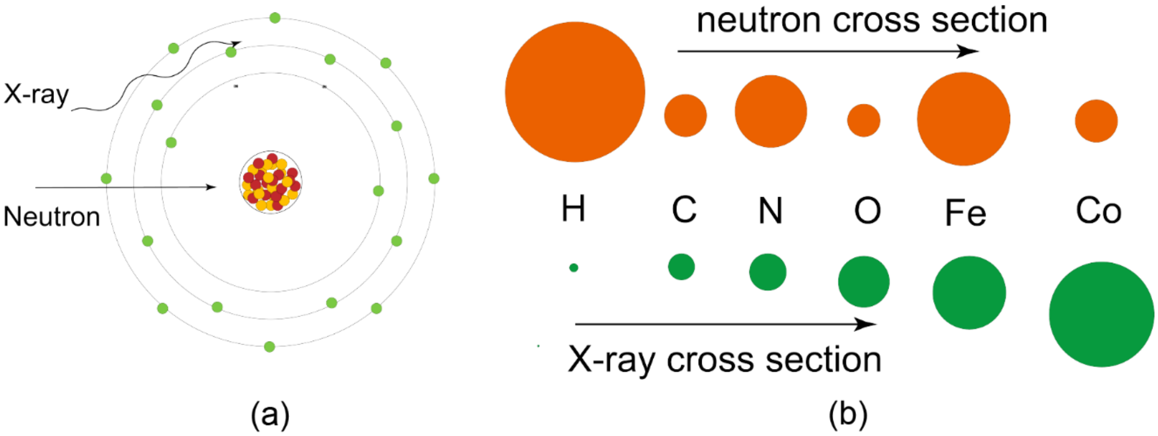

Figure 2.2: (a) Schematic illustration comparing how X-rays and neutrons interact with matter. X-rays primarily scatter off electron clouds, making them more sensitive to heavier elements with more electrons. In contrast, neutrons interact with atomic nuclei, enabling detection of lighter elements and isotope-specific information. (b) Qualitative comparison of neutron (orange) and X-ray (green) scattering cross sections for selected elements.

Neutrons are produced in nuclear reactors, where fast neutrons from fission are slowed down by moderators (e.g., graphite, heavy water) to become thermal neutrons. The reactor core provides a steady and intense flux of thermal neutrons, which can be extracted for diffraction experiments using collimators. Neutron beams are inherently polychromatic with broad energy distribution. To obtain a monochromatic beam, one method is to apply mechanical velocity selectors to filter specific neutron speeds. The other way is to select specific wavelengths through Bragg diffraction with crystal monochromators. In early experiments, metallic halide crystals with very small mosaic spreads, such as LiF, NaCl, and $CaF_2$, were used as monochromators. Later, metallic crystals (e.g., lead, copper) were found to be more efficient, providing higher reflected intensities. The monochromators have two positions, that is reflection mode and transmission mode. Reflection mode is more frequently used and requires larger crystals, which usually allows better intensity control.  Foreshortening techniques, which is first demonstrated in X-ray studies, is also applied to optimizes reflection geometry for better neutron intensity. Collimators are essential for defining the neutron beam direction and improving resolution. A typical collimation setup includes apertures with a few centimeters wide and long collimators to ensure good angular resolution in diffraction patterns. Collimated neutron beams are usually Maxwellian-distributed, with a typical peak wavelength ~1.5 Å. Similar to X-ray diffraction, neutron diffraction can also be divided into two types, powder diffraction and single crystal diffraction. Powder neutron diffraction requires a large sample (~2–3 cm in height, ~1 cm thick) and cylindrical or slab geometry ensures uniform neutron exposure. Single crystal neutron diffraction uses much smaller samples and provides higher resolution and avoids peak overlap issues seen in powder diffraction. However, neutron absorption remains a challenge, which can affect data quality, and therefore careful material selection is required. Boron trifluoride proportional counters are commonly used for neutron detection. These detectors operate based on neutron capture by boron-10. The counter size is typically ~5 cm diameter, 50 cm length. 80% detection efficiency can be achieved when enriched with $^{10}$B isotope. The counter are positioned ~60 cm away from the sample to minimize background noise and shielded with neutron-absorbing materials (e.g., cadmium, boron-loaded plastics) to reduce extraneous signals. The detector is mounted on a rotating arm. Diffraction data are either logged at small angular intervals using electronic scaling circuits, or continuously recorded with a pen recorder (ratemeter-based). The scanning speed can be as slow as ~5° per hour in order to capture weak diffraction peaks. Neutron spectrometers are much larger than X-ray diffractometers because they require long collimation paths, larger shielding requirements and low neutron flux to necessitate long exposure times.

Neutron diffraction is a unique tool for studying magnetic structures, as it directly interacts with spin and orbital moments. More detailed discussion about the types of magnetic materials will be included in the next section. Paramagnetic materials have randomly oriented magnetic moments at high temperatures. Neutron scattering from paramagnets is primarily incoherent, since the uncorrelated spins do not produce long-range magnetic order. The differential magnetic scattering cross-section depends on spin quantum number (*S*) of the ions, neutron magnetic moment interaction, and magnetic form factor which accounts for the distribution of unpaired electrons. Antiferromagnetism (AFM) occurs when neighboring spins are antiparallel, leading to a net-zero magnetization. Below the Néel temperature ($T_N$), neutron diffraction reveals superlattice reflections, which indicate a doubling of the magnetic unit cell. The magnetic Bragg Peak by neutron diffraction will disappear above $T_N$. The intensity of these peaks follows a Brillouin function and confirms the expected spin-ordering behavior. Neutron diffraction allows direct determination of the spin alignment direction, which is difficult to achieve with other techniques. In some materials, the orbital angular momentum also contributes to the magnetic structure. Neutron diffraction differentiates between spin-only and spin-orbit-coupled systems by analyzing the form factor deviations due to orbital contributions and the changes in Bragg peak intensities at different scattering angles. In ferromagnetic materials, such as Fe, Co and Ni, all spins align parallel and result in a strong net magnetization. Ferrimagnetic materials also have net magnetization, caused differently by two opposing spin sublattices with unequal moments. Neutron diffraction studies provide insights into spin alignments and magnetic domain structures and help determine the magnetic moment per atom by analyzing Bragg peak intensities. Magnetized materials selectively scatter neutrons based on spin polarization. Neutron polarization experiments can separate spin-up and spin-down states and are used to study spin-wave excitations in magnetically ordered materials.[89]

The powder neutron diffraction patterns in this dissertation were measured at POWGEN beamlines of the Spallation Neutron Source (SNS) in Oak Ridge National Laboratory. In each measurement, ~3 to 5 grams sample powders were loaded in a vanadium PAC can and sealed by copper can collar and aluminum can lid in He atmosphere.

## 2.4 Magnetic susceptibility measurement

Magnetic susceptibility $\chi$, is the quantity that relates a material's magnetization *M*, to the strength of an applied magnetic field, *H*. Conventionally, M and H have a linear relationship as

$$M = \chi H \tag{2.3}$$

equation 2.2 shows, which is typically valid in higher temperatures and low fields. Magnetic susceptibility $\chi$ will tell the researchers the magnetic identity of the materials they synthesize. There are two different applied field for the magnetic susceptibility measurement. The first one is direct current (DC) field, which can veil the static magnetic properties. The other one is an alternating current (AC) field to measure the dynamic properties.

In the past, researchers Gouy and Faraday balance techniques were the more popular methods to determine magnetic susceptibility by measuring the apparent weights of the materials.[91-92] Nowadays, more precise measurements can be made by Superconducting Quantum Interference Device (SQUID), which can offer temperature below the boiling point of helium (~2 K). A SQUID can detect extremely small changes in magnetic flux with two parallel Josephson junctions that form a superconducting loop. A superconducting magnet and a cryostat are also applied in the instrument to perform field and temperature-dependent susceptibility. The term field cooled (FC) and zero-field-cooled (ZFC) are used respectively to describe whether a material is cooled down with or without an applied magnetic field. In the ZFC process, the sample is first cooled down to a low temperature without applying an external magnetic field. Once the desired low temperature is reached, a small external magnetic field is applied, and then the sample is gradually heated while measuring its magnetization as a function of temperature. This method helps study the intrinsic magnetic response of a material in the absence of an initial magnetic field, revealing information about magnetic ordering, phase transitions, and pinning effects in superconductors. In the FC process, the sample is cooled down from high temperature while an external magnetic field is applied. After reaching low temperature, the magnetization is measured while heating the sample, keeping the external field constant. FC measurements reveal how a material's magnetic properties evolve when cooled under a magnetic field. This method provides insight into domain dynamics, magnetic anisotropy, and superconducting vortex behavior. In many materials, especially superconductors and spin glasses, the ZFC and FC curves differ significantly, indicating irreversible magnetic behavior or trapped magnetic flux. In a superconductor, ZFC often shows a sharp drop in magnetization due to flux pinning, while FC exhibits stronger diamagnetism due to trapped magnetic flux.

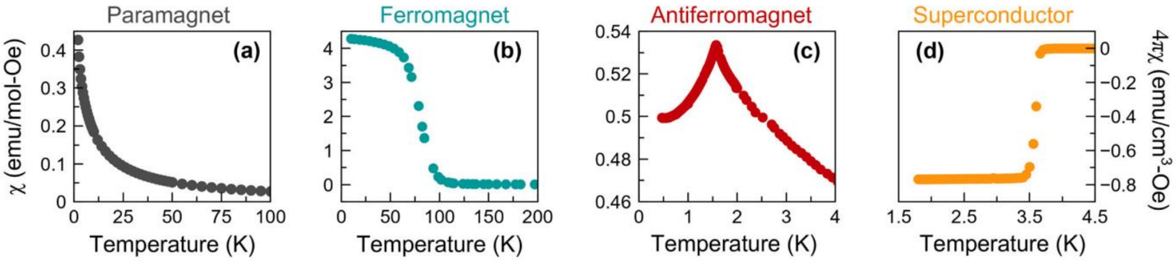

Figure 2.3: Representative magnetic susceptibility (χ) vs. temperature (T) curves for four distinct magnetic ground states: (a) Paramagnet – χ decreases monotonically with increasing temperature, following Curie–Weiss-like behavior; (b) Ferromagnet – a sharp drop in χ is observed at the Curie temperature, indicating spontaneous magnetization below ~70 K; (c) Antiferromagnet – χ shows a characteristic peak at the Néel temperature (~2 K), corresponding to antiparallel spin ordering; (d) Superconductor – a sharp diamagnetic onset below Tc (~3.6 K) is observed in volume susceptibility (4πχ), signaling the Meissner effect and the onset of superconductivity.[92]

Magnetic susceptibility measurements in this dissertation were performed on a 7 T Quantum Design SQUID (SQUID MPMS3) at Quantum Materials Center (QMC), University of Maryland. Powder samples were held in a clear plastic capsule sealed with cotton. At a MPMS 3 mounting station, two clear plastic straws were made into a double layered holder, the inner layer of which caught the capsule at the point of ~ 66 mm from the bottom of the holder. The plastic materials of the capsule and the holder can be polycarbonate, polypropylene, Delrin (acetal copolymer), and Kel-F (PCTFE), which have cryogenic compatibility and low background moment due to their nonmagnetic material characteristics. Colored holders should be avoid since the dyes of the color are generally magnetic. One end of the holder was sealed with Kapton type, while the other end was attached to a carbon fiber rod to help the holder insert into the well-like chamber of the instrument. A temperature-dependent magnetic susceptibility ($\chi$ vs T) at selected field strengths and field-dependent isothermal magnetization (M vs H) were measured at direct current to help identify the type of magnetic order and detect if there is phase transition in the sample. A typical $\chi$ vs T measurement starts with a ZFC process followed by a FC process.

## 2.5 Electron transport measurement

Electrical resistivity and conductivity are fundamental properties that determine a material's ability to transport electric charge. These properties play a crucial role in material science, electronics, energy storage, and power transmission. Conductivity measures how well a material allows electrical current to flow, while resistivity quantifies its opposition to current. The relationship between these properties is given by $\sigma=1/\rho$, where $\sigma$ represents conductivity and $\rho$ represents resistivity. Different materials exhibit varying electrical behavior based on their atomic and electronic structures. Metals such as silver and copper have high conductivity due to the presence of free electrons in their conduction bands, while semiconductors exhibit tunable conductivity, influenced by temperature and doping. Insulators, like glass and rubber, have extremely high resistivity, making them poor conductors of electricity. Beyond classical conductors and insulators, ionic conductors and superconductors provide specialized functionalities in battery technology and quantum materials. Temperature plays a significant role in resistivity and conductivity. In metals, resistivity increases with temperature due to enhanced electron-phonon scattering, whereas in semiconductors, resistivity decreases as more electrons transition to the conduction band.

Advanced theories such as Bloch-Grüneisen relations and Matthiessen's Rule explain how different scattering mechanisms impact electronic transport. Understanding electrical resistivity and conductivity has led to advancements in nanoelectronics, superconductors, and power grid optimization. These concepts are crucial for designing high-efficiency materials for electrical wiring, semiconductor devices, and next-generation energy systems.

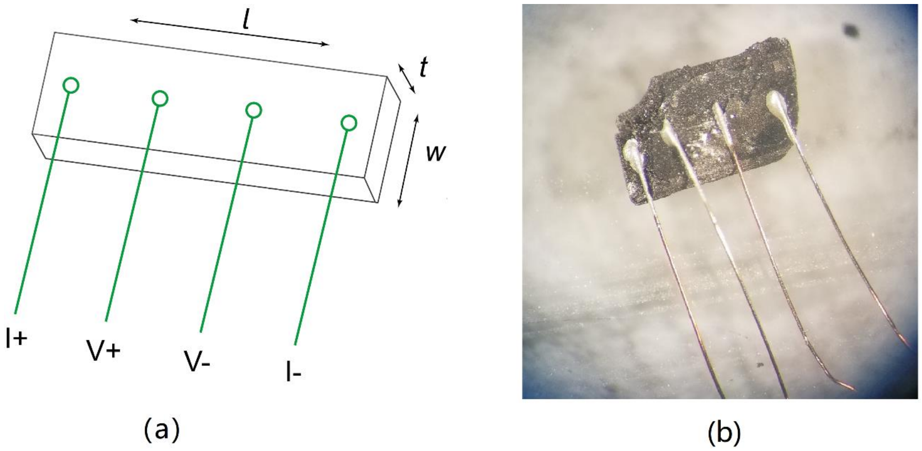

Figure 2.4: Schematic and optical image of a four-probe resistivity measurement setup. (a) A schematic illustration showing the standard configuration for four-probe measurements on a rectangular sample, with current applied through the outer contacts (I+ and I–) and voltage measured across the inner contacts (V+ and V–). The sample dimensions *l* (length), *w* (width), and *t* (thickness) are labeled. (b) Optical image of a real sample wired for measurement using silver paste and thin gold wires.

## 2.6 Thermogravimetric analysis

Thermal analysis (TA) refers to techniques that monitor the physical and chemical changes of materials as a function of temperature and time. Thermogravimetric analysis (TGA) specifically measures mass loss during heating, cooling, or isothermal holding conditions. The temperature program in TGA may include constant heating rate (non-isothermal method), stepwise heating with isothermal holds (quasi-isothermal method) and cooling cycles for phase transition studies. The mass changes can be caused by the decomposition of materials, evaporation of volatile compounds, oxidation or reduction reactions in reactive atmospheres, and adsorption or desorption processes in porous materials. However, TGA can not detect phase transition, polymorphic transformations or reactions without mass change without complementary techniques such as differential scanning calorimetry (DSC) or differential thermal analysis (DTA). The microbalance of a TGA system can measure mass changes from 1 mg to several grams in a furnace, which can controls temperature reaching up to 1600 °C. Gas flow system can decide which kind of gas into the furnace to create different atmosphere, including inert ($N_2$, Ar), oxidizing ($O_2$, air) or reducing ($H_2$, CO) environment. There are mainly three different configurations of sample holders: top-loading style where sample hangs on a support rod, bottom-loading holders whose sample pan is placed on a hook, and side-loading which is used in horizontal furnaces. The temperature near the sample is monitored and regulated by thermocouple.

## 2.7 Circular dichroism

Circular dichroism (CD) refers to the differential absorption of left- and right-circularly polarized light by chiral molecules. CD spectroscopy is widely used in biochemistry, molecular biology, and supramolecular chemistry to study chiral molecules. The phenomenon of optical activity was first discovered in the early 19th century in solutions of chiral compounds such as tartaric acid. The development of CD spectroscopy as a quantitative tool began in the mid-20th century, particularly in the study of biopolymers and small organic molecules. Chiral molecules interact differently with left- and right-circularly polarized light, leading to nonzero rotational strengths in electronic transitions. The observed CD signal is proportional to the difference in absorption:

$$\Delta A = A_L - A_R \tag{2.4}$$

where $A_L$ and $A_R$ are the absorbances of left- and right-circularly polarized light. CD spectra provide insight into electronic transitions, molecular symmetry, and the environment of chiral centers. The core components of a CD instrument include a monochromator to select a specific wavelength of light for measurement, a photo elastic modulator (PEM) to convert linearly polarized light into circularly polarized light to alternate between left and right circular polarization, and a photomultiplier detector (PMT) to measure the difference in light absorption for both polarizations. CD instruments require frequent calibration to ensure accurate measurements. The standard calibration method uses (+) 10-camphorsulfonic acid (CSA), which has well-characterized CD bands at 192.5 nm and 290.5 nm. Other calibration approaches involve measuring oxygen-free optical rotatory dispersion (ORD) standards or using reference samples such as quartz plates. Variations in temperature, humidity, and optical alignment can introduce errors, so periodic recalibration is necessary. Sample concentration should be optimized to avoid saturation effects in the detector. Typically, 0.1-1.0 mg/mL concentrations are used for protein and DNA samples. Cuvette path lengths range from 0.01 mm (for UV studies) to 10 mm (for visible spectra). Aggregation, bubbles, or particulate matter can introduce artifacts. CD spectra are highly sensitive to temperature variations, requiring thermostatted sample holders. Common setups include Peltier temperature controllers for stability during kinetic and denaturation studies.

# Chapter 3: Solvothermal synthesis of amine intercalated Fe and Co chalcogenides and polar ferromagnetic breaking the crystal symmetry.

The work described within this chapter was mainly published in *Chemistry of Materials*, **2021,** *33* (13), 4936-4947. Brandon C. Wilfong, Daniel Hhickox-Young, James M. Rondienlli, Peter Y. Zavalij and Efrain E. Rodriguez were the contributing authors of the manuscript. H.Z. synthesized the samples, collected and analyzed the powder XRD data. B.W. and H.Z. performed the MPMS measurements. D.H.Y and J.M.R. calculated the electronic structure. P.Z. performed single crystal diffraction experiments and solved the crystal structure.

## 3.1 Introduction

Polar structural transitions in metals are rare.[93] In 1965 Anderson and Blount predicted a *ferroelectric-like metal* in the A15-type superconductor $V_3Si$.[94] By ferroelectric, they referred to the loss of a center of symmetry in the crystal structure and the appearance of a polar axis. The coexistence of such a polar distortion with metallic conductivity was long deemed unachievable due to the propensity for free charges to screen or disrupt dipole formation. They are potentially promising quantum materials. In the field of superconductivity, non-centrosymmetric materials can host unconventional, pairing mechanisms.[95] Furthermore, the lack of inversion symmetry in these materials can lead to antisymmetric spin-orbit coupling and to nonreciprocal effects and directional anisotropy in physical properties.[96] Implications for spintronic applications include the stabilization of spin states that are topologically protected. The preparation of polar magnetic metals therefore remains an important endeavor for materials chemists. Although compositional order has been used to enforce a metallic polar structure in a variety of intermetallic compounds,[1] metals that exhibit both centric (high) and acentric (low) symmetry phases are much less common. The presence of a symmetry-breaking transition is desirable due to the possibility of dynamic control over the various properties enabled by broken inversion symmetry.

Recent work on transition metal oxides demonstrates that we can find new polar or ferroelectric metals through crystal chemistry.[97-99] either high pressure or epitaxial strain on model systems, materials scientists have recently made progress in this field.[93, 98] Shi *et al* were among the first to establish a ferroelectric distortion in a metal.[100] Through coordinated displacement of $Li^+$ cations in the crystal structure of $LiOsO_3$, the oxide breaks inversion symmetry below 140 K. Another strategy is to find a known perovskite that is metallic and to place it under epitaxial strain to populate polar domains.[98] In each case, the atomic orbitals contributing states at the Fermi level tend to be decoupled from the inversion-lifting mechanism. This observation led to the development of the weak coupling hypothesis, an operational principle which states that weak coupling between the conduction electrons and the polar distortion is a prerequisite for the existence of a polar metal. [101]

Here, we report how the seemingly contraindicated properties can arise in a single material by judicious combination of inorganic and organic building blocks. The hybrid inorganic-organic perovskites, for example, unexpectedly display both ferroelectricity and semiconductivity.[102-104] Many postulate that this combination of enhanced optoelectronic properties in hybrid perovskites.[105-109] arise from uniting an ionic salt with an organic molecule. To that end, our strategy here was to prepare a hybrid material based on a layered material, which we term tetrahedral transition metal chalcogenide (TTMC)[2, 63-66, 110,111] as the metallic host. As shown in Figure 3.1, TTMCs contain a metal sublattice that is completely square. They typically accommodate smaller, first-row transition metals such as iron,[112] cobalt,[113,114] and nickel.[115] A common feature of layered metal chalcogenides is their extensive intercalation chemistry,[116] which can be exploited to manipulate their properties. In this study, we selected layered cobalt sulfide (CoS) as the TTMC host, which is also a known ferromagnet[113, 114]—introducing yet additional functionality.

We can intercalate molecules into our layered TTMC to form a new hybrid material. Intercalated Co(*en*)$_3$ units (where *en* = ethylendiamine) are octahedral and similar to the classic coordination complexes of Alfred Werner.[116-118]

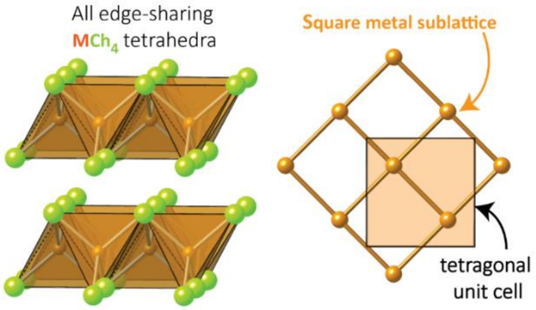

Figure 3.1: Tetrahedral transition metal chalcogenides (TTMCs), which are composed of all edge-sharing $MCh_4$ tetrahedra where $Ch$ = S, Se, or Te and $M$ = Fe, Co, Ni, or Cu. The metal sublattice is a perfectly square one, which results in a tetragonal cell.

These complexes are chiral and the amino group of the bidendate ligand interacts with the sulfides of the CoS layers via hydrogen bonding. Hydrogen bonding as a mechanism for ferroelectricity is as old as the field itself since its discovery in Rochelle salt $NaKCH_4O_6 \cdot 4H_2O$.[119,120] Since the layered TTMC provides metallicity while the hydrogen bonding of the intercalate complexes induces a polar distortion, the resulting compound satisfies the weak coupling hypothesis. The extended solid combines with the molecular complexes to achieve the sought after polar metallic phase. While a high-symmetry parent structure has not yet been observed, one is expected to occur at high temperature due to the potential for thermal fluctuations to destabilize hydrogen bonds. As the first system to demonstrate a polar metallic phase stabilized via hydrogen-bonding, and the first reported ferromagnetic polar metal, intercalated TTMCs represent a new class of polar metals which may exhibit previously unreported functionality.

## 3.2 Experimental and Computational Methods

### 3.2.1 Sample Synthesis.

To prepare the title compound, we used solvothermal methods. We first combined 10 mmol of Co powder (Alfa Aesar, 99.5%), 10 mmol of thiourea (Sigma-Aldrich, 99.0%) and 3.8 mmol of $NH_4Cl$ (Fisher, 99.5%). The $NH_4Cl$ is the mineralizer. The powder reagents were then suspended in 20 mL of ethylenediamine (Sigma-Aldrich, 99.0%). We sealed the mixture in a Teflon cup within a stainless-steel autoclave. We filled the Teflon vessel to about 43% by volume. The loading of the autoclave was performed entirely in an $N_2$-filled glovebox.

The autoclave was then heated to 140 °C and kept there for 3 to 5 days. After the solvothermal reaction was complete, we cooled the autoclave to room temperature and recovered the contents in the glovebox. The supernatant above the product appeared either an orange or red color. We poured the solid product along with the supernatant into a funnel lined with filter paper. We then washed the product with ethylenediamine (*en*) several times and left it to dry in the glovebox.

We found the contents left on the filter paper to be a mixture of black powder, irregular black crystals, and yellow crystals. We physically separated the crystals from each other to get enough samples for X-ray diffraction and other characterization studies. The black crystals correspond to the title compound and the yellow crystals to a side product, $[Co(en)_3]Cl_2$, which we describe later. More information on synthesis and side products can be found in Supplementary Information (SI).

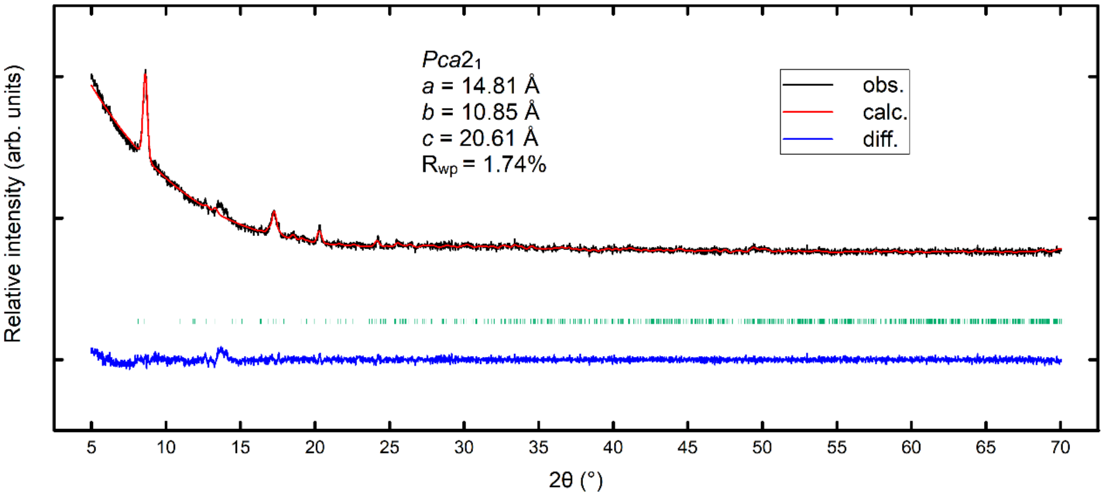

Figure 3.2: The powder XRD patterns of ground polycrystalline $[Co(en)_3](CoS)_{12} \cdot en$ collected at room temperature. Le Bail fit of the $[Co(en)_3](CoS)_{12} \cdot en$ structure in the orthorhombic space group *Pca*2₁. Tick marks represent the corresponding phase.

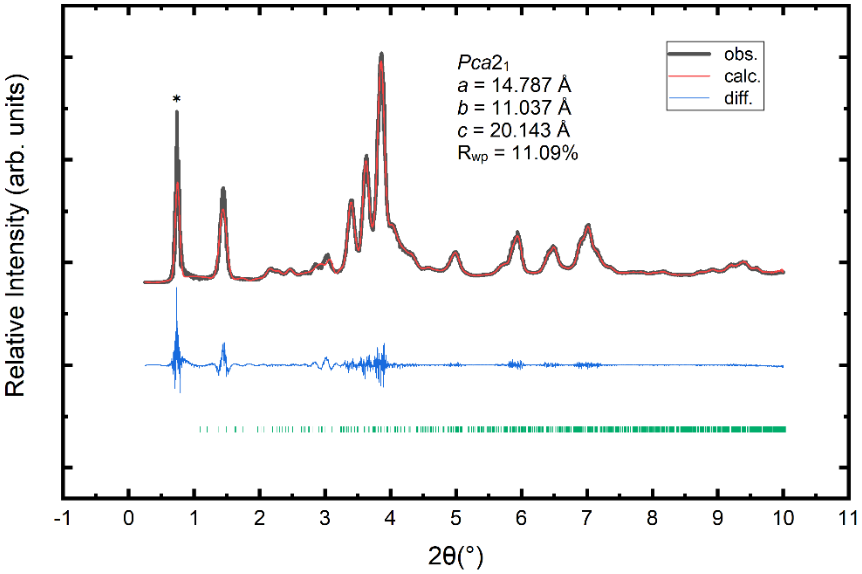

Figure 3.3: The synchrotron XRD patterns of polycrystalline $[Co(en)_3](CoS)_{12} \cdot en$ collected at Beamline 11-ID-B in Advanced Photon Source, Argonne National Laboratory. Le Bail fit of the $[Co(en)_3](CoS)_{12} \cdot en$ structure in the orthorhombic space group *Pca*2₁. Tick marks represent the corresponding phase. Asterisk denotes diffraction peak attributed to Kapton tube used in holding the polycrystalline sample.

We also attempted the same solvothermal synthesis with Co metal, $NH_4Cl$ in ethylenediamine but with sulfur powder in place of thiourea as the sulfide source. The resulting supernatant was green in color. This synthetic route did not yield crystals of sufficient quality to carry out single crystal X-ray studies. We were, however, able to recover a black powder to characterize. Furthermore, it is likely that the structure of this product is slightly different from that of en-CoS. The powder XRD patterns (Figures 3.2 to 3.3) reveal a slightly larger *c*-parameter in this product than in en-CoS. Both products, however, are unstable above 200 °C as solvothermal reactions above this temperature always resulted in the conversion of the layered CoS into pentlandite $Co_9S_8$ (Figure S4).

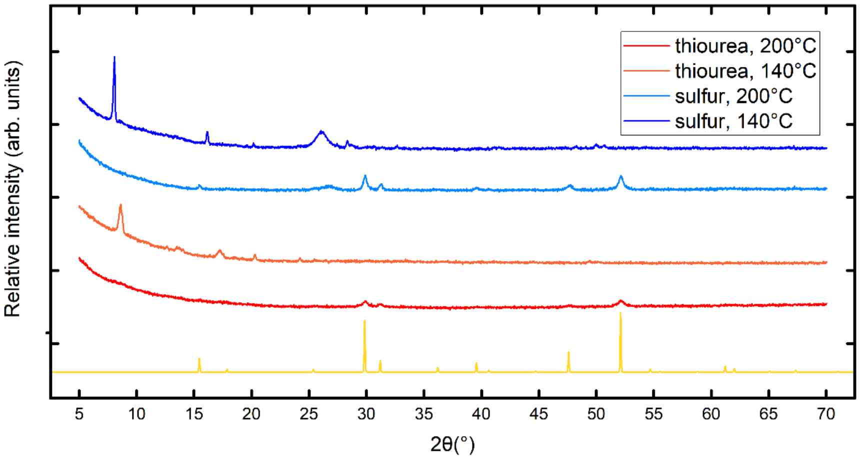

Figure 3.4: The powder XRD patterns of ground polycrystalline samples of the solvothermally prepared products under different reaction conditions (temperature, sulfur source). Patterns were collected at room temperature. The yellow curve at bottom represents the calculated powder XRD patterns of cubic $Co_9S_8$ through CrystalDiffract$^{TM}$, indicating that the product of the solvothermal synthesis at 200°C is more likely to be $Co_9S_8$ instead of the title compound. The selenide analog of the former compound was also reported by Zhou X., *et al.* in a thermal transformation from tetragonal CoSe from below 150°C to 200°C.[86]

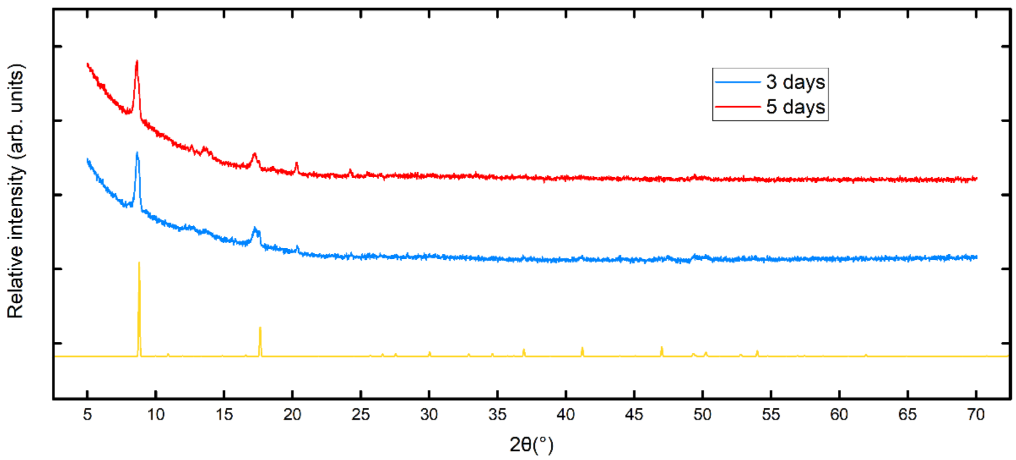

Figure 3.5: The powder XRD patterns collected at room temperature of ground polycrystalline sample of the solvothermally prepared product for different number of days. Thiourea was used as the sulfur source and the reaction was carried out at 140°C. The yellow curve at bottom represents the calculated powder XRD patterns of $[Co(en)_3](CoS)_{12} \cdot en$ from CrystalDiffract™.

### 3.2.2 Diffraction study

Powder X-ray diffraction (PXRD) powder patterns were collected using a Bruker X-ray diffractometer applied with Cu Kα radiation (λ = 1.5418 Å, step size = 0.020°, 2θ = 5 - 70°). Additional PXRD was collected on beamline 11-IDB at the Advanced Photon Source (Argonne National Laboratory). A wavelength of 0.2114 Å was used (58.66 keV) with Perkin Elmer XRD1621 amorphous silicon detector. To determine the structure, we performed single crystal XRD experiments on a Bruker Smart Apex II CCD diffractometer with Mo Kα radiation of λ = 0.71073 Å (2θ = 3.68 – 52.98°). A crystal with approximate dimension of 0.153 mm × 0.11 mm × 0.007 mm in size was selected and kept at 150(2) K during data collection. The structure was solved and refined with the ShelX software package.

Table 3.1: Single crystal X-ray diffraction data for $[Co(en)_3]Cl_2 \cdot en$ and $[Co(en)_3]Cl_2$.

| Structure | $[Co(en)_3]Cl_2 \cdot en$ | $[Co(en)_3]Cl_2$ |
|---|---|---|
| Space group | *C2/c* | *Pbca* |
| Empirical formula | $C_{15.91}H_{56}Cl_4Co_2N_{14}$ | $C_{16}H_{24}Cl_2CoN_6$ |
| $a$/ Å | 33.4529(14) | 8.1835(7) |
| $b$/ Å | 8.7631(4) | 17.1315(15) |
| $c$/ Å | 23.7869(10) | 20.4500(18) |
| $\alpha$/ ° | 90 | 90 |
| $\beta$/ ° | 100.3681(7) | 90 |
| $\gamma$/ ° | 90 | 90 |
| Crystal system | monoclinic | orthorhombic |
| Volume(Å$^3$) | 6859.3(5) | 2867.0(4) |
| Z | 8 | 8 |
| Calculated density (g·cm$^{-1}$) | 1.362 | 1.437 |
| $\lambda$, Mo K$\alpha$/ Å | 0.71073 | 0.71073 |
| $2\theta$ range/ ° | 3.482 to 54.998 | 3.984 to 59.994 |
| Crystal size/ mm$^3$ | 0.31 × 0.30 × 0.09 | 0.28 × 0.14 × 0.10 |
| No. reflections collected | 47592 | 43289 |
| No. independent reflections | 7890 | 4182 |
| $F$ (000) | 2972.0 | 1304.0 |
| Final R indexes [I>2$\sigma$(I)] | $R_1 = 0.0367$, $wR_2 = 0.0891$ | $R_1 = 0.0228$, $wR_2 = 0.0531$ |
| Final R indexes [all data] | $R_1 = 0.0477$, $wR_2 = 0.0938$ | $R_1 = 0.0314$, $wR_2 = 0.0557$ |
| Temperature/K | 120(2) | 150(2) |

### 3.2.3 Magnetic measurements

We conducted temperature and field dependent DC (direct current) magnetization measurements with a Quantum Design Magnetic Property Measurement System (MPMS3). We placed as-recovered polycrystalline samples in a gel cap holder, which was then inserted into a clear drinking straw. The magnetization of the sample was then taken upon zero-field-cooling (ZFC) from 300 K to 1.8 K and then upon heating from 1.8 K to 300 K in the field-cooled (FC) state. We applied a small field of 100 Oe for the FC measurement. Isothermal magnetization measurements were conducted on the same instrument at a series of temperatures with applied fields between $H = \pm 7$ T. Magnetization was converted to molar magnetic susceptibility and magnetic moment (in Bohr magnetons) per Co atom using the derived structure, molar mass, and density from single crystal X-ray diffraction experiments.

### 3.2.4 Resistivity measurements

Electrical resistance measurements were performed using a Quantum Design Physical Property Measurement System (PPMS-9T) on pressed pellets of as-recovered polycrystalline samples. The polycrystalline samples were cold pressed into a pellet under 2000 psi of uniaxial stress. To form a pellet of uniform density, we dynamically pumped on the die apparatus during the pressing. We performed temperature dependent resistance measurements using the four-probe technique by attaching gold wires onto the pressed pellet with silver paint. The pressed pellet had dimensions of 2 mm x 2 mm x 0.5 mm. Once in the PPMS, the sample's resistance was measured from 1.8 K up to 300 K upon applying a current of 0.1 mA. No magnetic field was applied.

### 3.2.5 First-principles calculations

Calculations were performed using density functional theory (DFT) as implemented in the Vienna *ab initio* simulation package (VASP)[123,124] using a planewave basis set with an energy cutoff of 600 eV. The Perdew-Burke-Ernzerhof (PBE) exchange-correlation functional revised for solids (PBEsol)[125] was used along with the projector-augmented wave method to treat the separation of the core and valence electrons.[126] The *en* molecules were excluded from our calculations, but all Co and S atoms as well as the lattice parameters were held fixed to their positions as determined by XRD. The Brillouin zone was sampled using a $4\times5\times3$ Γ-centered mesh and Gaussian smearing (width of 0.1 eV). Electrostatic doping simulations are performed by modifying the number of electrons in the simulation. Charge neutrality is preserved through a compensating background charge.

## 3.3 Results

### 3.3.1 Crystal structure.

Unlike most of the intercalated TTMCs (e.g. FeSe), the title compound does not crystallize in a tetragonal space group. The underlying sublattice of TTMCs is that of a square net, so it must contain a 4-fold axis and crystallize in either *P*4/*nmm* or *I*4/*mmm*.[2, 64] Because the intercalation of *en* molecules with nominally $D_3$ point symmetry lifts the 4-fold symmetry, we initially solved the structure in the orthorhombic *Pnma* (space group no. 62) with lattice parameters of a pseudo-tetragonal cell shown in Figure 3.6 ($a$ = 3.69 Å , $b$ = 3.69 Å, $c$ = 20.10 Å, and $\alpha = \beta = \gamma = 90$ °). In addition to observing the orthorhombic distortion, we also observed several weak reflections not indexed by the small cell. In the precession images simulated from the experimental single crystal data (Figure 3.6), we index these superstructure reflections to obtain a supercell of dimensions $a$'= 3$a$, $b$' = 4$b$, and $c$'=$c$. We note that the superstructural reflections (blue circles, Figure 3.6) are several orders of magnitude weaker than the main reflections (green circles, Figure 3.6) of the pseudo-tetragonal cell (Figures3.7). Therefore, while we were able to carry out LeBail fit of the orthorhombic cell to the PXRD patterns (Figures3.2,3.3), we would not have been able to solve the structure with PXRD.

We solved the crystal structure in *Pbcn* (space group no. 60) for the supercell since the quadrupling of the *b*-axis (in setting *Pbnm* for space group no. 62) causes the *n*-glide plane to turn into a *c*-glide. The residual from the solution in *Pbcn*, however, was too high with an $R_1$ = 17 %. We therefore allowed the intercalated *en* molecules to further order in the structure. Such ordering of the intercalated molecules breaks the center of inversion in the unit cell. Choosing among the maximal non-isomorphic space groups of *Pbcn*, we found the non-centrosymmetric $Pca2_1$ (space group No 32). We then solved the structure in $Pca2_1$ and this reduced the residual to $R_1$ = 6.41 %. Note that $Pca2_1$ switches the *a*- and *b*-axes from *Pbcn* (i.e. *Pcan* as the parent structure setting).

The stoichiometry of the compound is $[Co(\mathit{en})_3](CoS)_{12}\cdot\mathit{en}$, but for the rest of the manuscript we will abbreviate its name to **en-CoS**. Solved in polar space group $Pca2_1$, the structure of en-CoS is shown in Figure 3.8. Details of the structural solution from the single crystal X-ray experiment are in Table 3.1. The crystallographic information file (CIF) and XRD powder pattern are available in the SI. The structure consists of $CoS_4$ tetrahedra that share all their edges to form the CoS layer. For every 12 CoS units in the cell, there is one $Co(\mathit{en})_3$ complex and one free *en* molecule. There are 4 formula units of $[Co(\mathit{en})_3](CoS)_{12}\cdot\mathit{en}$ per unit cell.

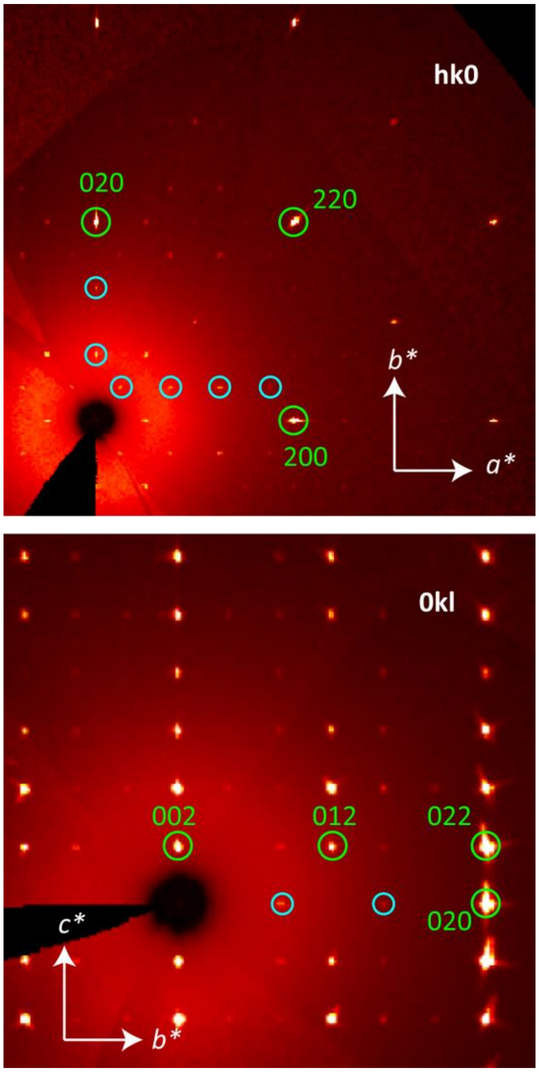

Figure 3.6: Precession images of single crystal x-ray diffraction. (top) Reflections in the *hk*0-plane indexed by a pseudo-tetragonal cell encircled in green. Reflections are brighter than the satellite reflections encircled in blue by three orders of magnitude. The four satellite reflections in blue along ***a**** indicate a cell quadrupled in the a-direction with

respect to the pseudo-tetragonal cell. (bottom) Reflections in the 0*kl*-plane. The satellite reflections in the ***b****-direction indicate a tripled cell with respect to the pseudo-tetragonal cell.

We argue that the complex Co(*en*)$_3$ is divalent based on two observations. First, bond valence calculations give a value close to two for the cobalt center. Relevant Co—N bond distances are given in Table 3.2, which we input into the bond valence calculations.[127] Second, the yellow crystals that we recovered along with en-CoS contain only divalent Co. One is orthorhombic with stoichiometry of [Co(*en*)$_3$]Cl$_2$ and the other has monoclinic symmetry with stoichiometry [Co(*en*)$_3$]Cl$_2$·*en*. The [Co(en)$_3$]Cl$_2$ · en crystals are highly air sensitive, and we believe it is similar to the compound that Kovnir et al. found when attempting to solvothermally prepare CoSe in neat ethylenediamine.[127] The PXRD results for a range of synthetic conditions can be found in Figures 3.4-3.5. For the rest of this manuscript, we describe the complex as Co(*en*)$_3$ with the implication of a Co$^{2+}$ state.

The polar nature of the crystal structure can be seen by the breaking of mirror symmetry normal to the *c*-axis, making the polar axis directly aligned with the [001] zone axis. The Co(*en*)$_3$ complex breaks this mirror symmetry by preferentially orienting itself closer to one CoS layer over the other. As a measure of this polarity, the Co center in the Co(*en*)$_3$ complex is about 0.135(5) Å closer to one CoS layer than the other (Figure 3.8). Likewise, for the *en* molecules, they are oriented in such a fashion so that they are closer to one layer of CoS over the other. The conformation of the free *en* molecule, however, is partly disordered. The free *en* molecules can have the CH$_2$—CH$_2$—NH$_2$ motif oriented in one of two directions. Close to 84 % of the *en* molecules adopt one orientation, and 16 % the other. We represent these two orientations in Figure 3.8b. Interestingly, the amino group closest to the CoS layer is fully ordered.

In space group *Pca*2$_1$, there is only one Wyckoff position, 4*a*, and the only symmetry present in this site is the identity operation. Therefore, all atoms are in general positions of the unit cell. The Laue group of *Pca*2$_1$ is *mm*2 ($C_{2v}$), which places this structure in the polar, achiral category.[129]

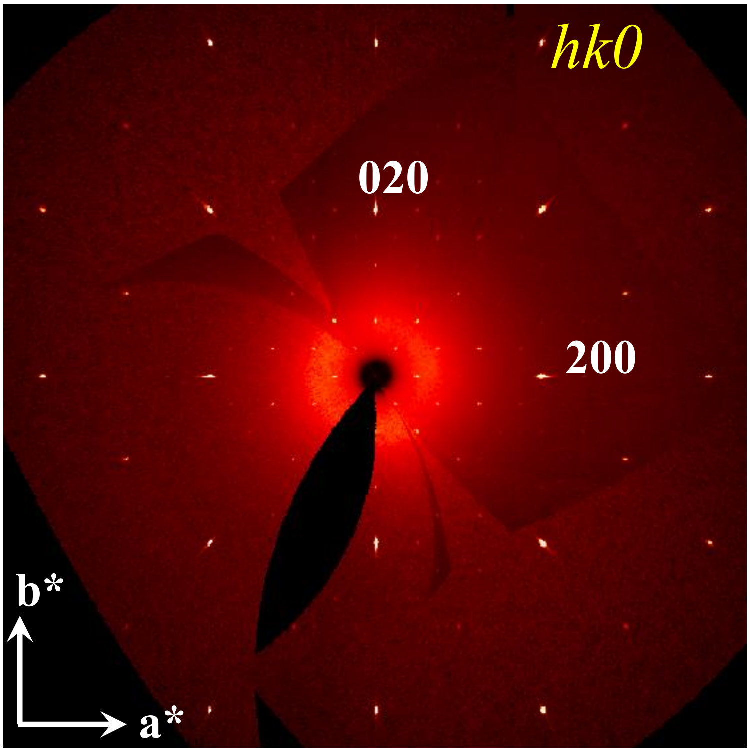

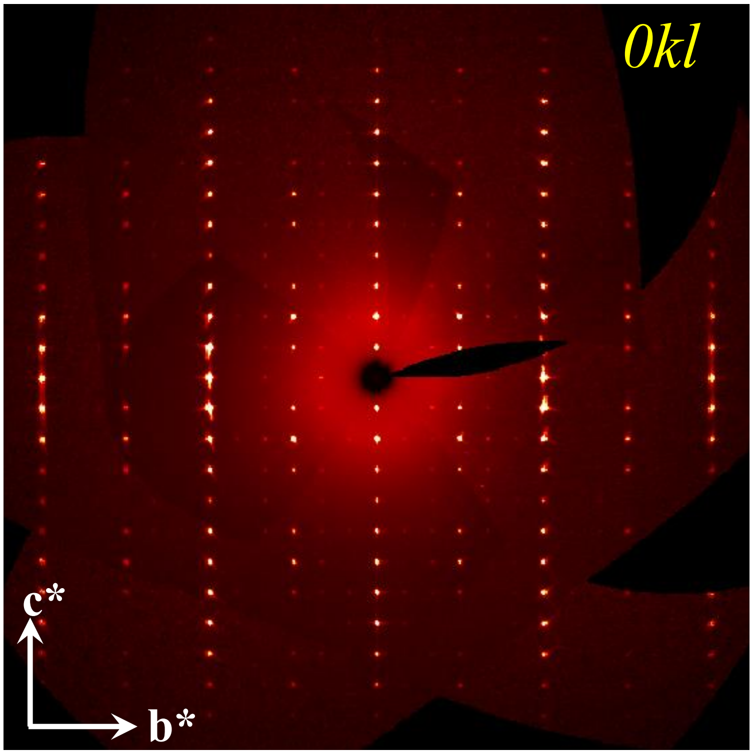

Figure 3.7: Full precession images of the hk0- and 0kl-planes from single crystal diffraction.

The single crystal exhibits a racemic mixture for the twinned domains in proportion of 55 % to 45 %. The twinning is associated with the choice of the polar axis along the *c*-direction. In other words, in one domain, the Co(*en*)$_3$ and *en* molecules are closer to the lower CoS layer, and in the other domain, to the upper layer. This preference for one polarity over the other characterizes a ferroic material and is usually associated with some external field through the transition temperature, whether magnetic, electric, or strain. Upon field cooling, one domain is preferentially populated over the other. In this case, likely some strain during crystallization causes one domain to be slightly favored over the other.

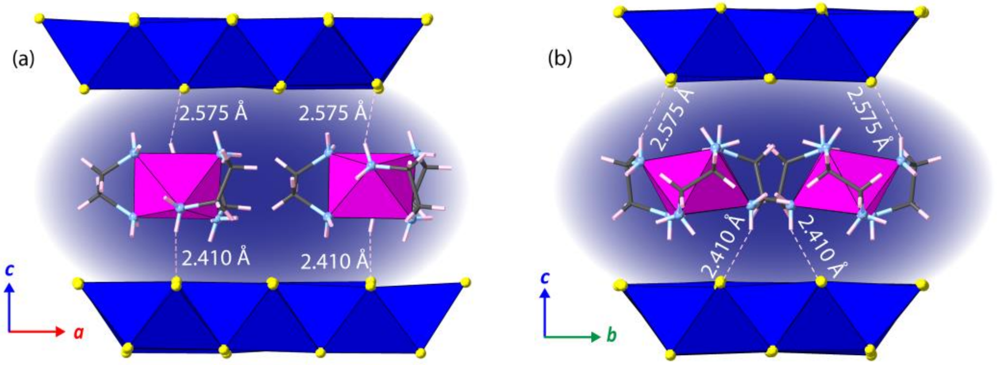

Figure 3.8: The two N—H…S hydrogen bonds that determine the polarity of en-CoS from single crystal structure. (a) View along the [010] zone axis, where the two closest hydrogen bonds to the sulfide layer from the [Co(*en*)$_3$]$^{2+}$ complex occur through two N—H groups above and below the complex. By choosing one closer hydrogen bond over the other, the structure breaks inversion symmetry. (b) View along the [100] zone axis demonstrates how the hydrogen bonds lead to a bending of the CoS layers along a direction parallel to the [001] axis.

Remarkably, the Co(*en*)$_3$ molecules order between the CoS galleries. The complexes also arrange in a pseudo-hexagonal cell as shown in Figure 3.9. The parameters for this pseudohexagonal cell show the distortion of the acute angle from 60°. The Co(*en*)$_3$ molecules likely pack in such a manner to be commensurate with the pseudo-tetragonal cell of the CoS layers. The complexes can have point group symmetry $D_3$ if not considering the ethylene conformation. The most efficient manner to pack the $\mathrm{Co}(\mathit{en})_3$ molecules is to have their 3-fold axes parallel to the *c*-axis (Figure 3.9). This arrangement has the triangular faces parallel to the CoS layers. Although the symmetry of the complexes may be $D_3$, the overall crystal point symmetry is not $D_3$ (or 32) due to reasons discussed later.

Table 3.2 Relevant bond distances (Å) and bond angles (°) for the $\mathrm{Co}(\mathit{en})_3$ complex in $[\mathrm{Co}(\mathit{en})_3]\mathrm{Co}_{12}\mathrm{S}_{12}\cdot\mathit{en}$. The bond angles correspond to the bite angles of the bidentate ligand on the Co center. Atom labels can be found in Figure S9.

| | |
|---|---|
| Co — N1 | 2.16(4) |
| Co — N4 | 2.16(2) |
| Co — N5 | 2.26(2) |
| Co — N8 | 2.21(4) |
| Co — N9 | 2.19(2) |
| Co — N12 | 2.10(3) |
| N1 — Co — N4 | 78.6(11) |
| N5 — Co — N8 | 79.4(10) |
| N9 — Co — N12 | 81.0(6) |

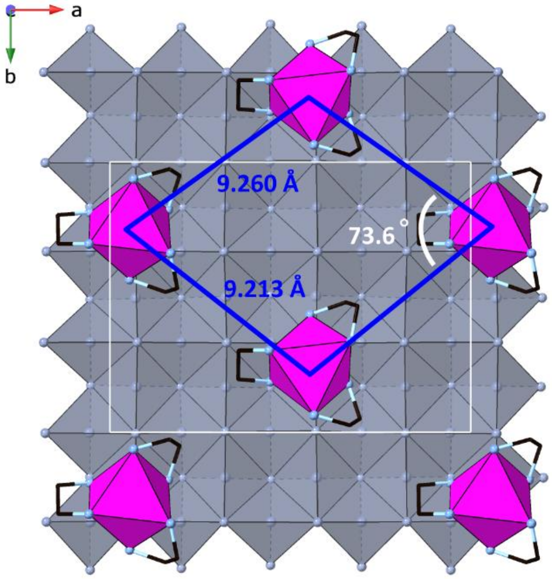

Figure 3.9: Single crystal structure of en-CoS viewed down the *c*-axis. The $\mathrm{Co}(\mathit{en})_3$ complexes are arranged so that the trigonal faces of the octahedra are parallel to the CoS layers shown in grey background. Both enantiomers are found in a

single layer, and they pack in a way to form a pseudo-hexagonal cell. The hydrogen atoms of the *en* molecules are not shown for clarity. The white lines indicate the orthorhombic lattice of en-CoS whereas the blue lines a pseudo-hexagonal cell for the packing of the Co(*en*)$_3$ octahedra.

### 3.3.2 Magnetism

Figure 3.10a presents the temperature dependent molar magnetic susceptibility for powders of en-CoS from 1.8 K - 300 K. The system displays clear paramagnetic behavior in the high temperature region above 50 K until around 43 K. At this point, the ZFC and FC curves diverge from paramagnetic behavior, which is indicative a ferromagnetic transition. The inset of Figure 3.10a shows this transition region where the molar magnetic susceptibility increases sharply at 43 K and the ZFC-FC bifurcation increases as the temperature decreases. The hysteric behavior of the ZFC-FC bifurcation below the transition temperature also implies a ferromagnetic transition. We were able to reproduce the 43 K transition in several batches of solvothermally prepared en-CoS.

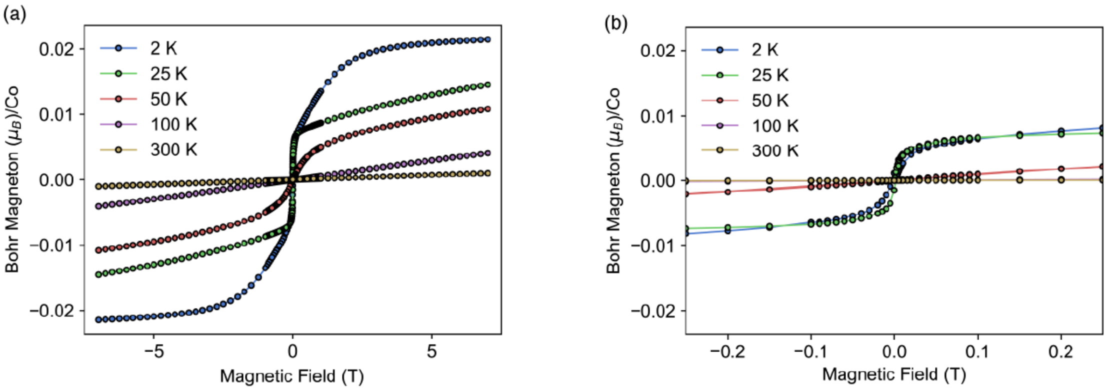

Figure 3.10: Field dependent magnetic measurements of a polycrystalline en-CoS sample. (a) Field dependent magnetization from -7 T to 7 T at a range of temperatures above and below the ferromagnetic transition. (b) A zoomed-in region at low applied field of the field dependent magnetization showing the soft ferromagnetic behavior.

Figure 3.10b shows the inverse molar magnetic susceptibility with Curie-Weiss law fit applied from 100 K - 300 K in the paramagnetic region. The extracted Curie-Weiss fit parameters include the following: $\chi_0$, which accounts for parasitic Pauli paramagnetic and diamagnetic contributions; the Curie constant $C$; and the Weiss field $\theta$. Their values are included in Figure 3.10b. The Curie temperature $T_C$ of 43 K appears to be slightly below $\theta$. The positive value of the Weiss field is expected for ferromagnetic interactions. That $T_C$ is close to 80 % of $\theta$ likely comes from the interplanar exchange interactions being weaker than those within the plane.

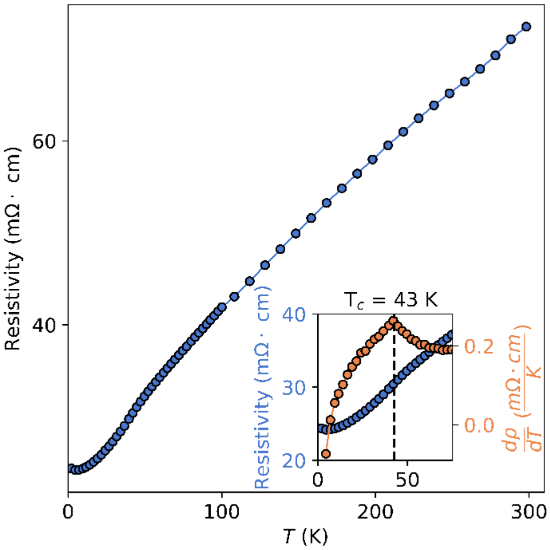

Figure 3.11: Temperature dependent resistivity of a pressed pellet of as-recovered polycrystalline en-CoS samples at zero applied field. The resistivity vs. temperature curve (blue) shows metallic behavior with a deviation from linearity around the 43 K Curie temperature emphasized in the inset by plotting the slope of the resistance vs. temperature curve (orange) indicating a discontinuity concomitant with the Curie temperature.

From the extracted Curie constant, we calculate the effective moment on each Co atom in the system assuming the Co atoms in the CoS layer and the Co($en$)$_3$ complexes equally contribute. From this approach, we find an effective moment of ~ 0.289 $\mu_B$/Co, which is significantly lower than in the related $KCo_2S_2$ ferromagnet.[113,130] The Weiss constant is positive, +51.94 K, indicating predominantly ferromagnetic fluctuations in the paramagnetic state and yields further justification for the assignment of ferromagnetism in this compound. For completeness, we also calculated the effective moment assuming that only the interlayer Co(*en*)$_3$ complex contributes, In such a case, we extract an effective moment of 3.76 $\mu_B$/Co, which closely agrees with the spin-only result for high-spin $d^7$ octahedral coordination.

Isothermal magnetization curves in Figure 3.10 show almost no hysteresis below $T_C$, which is to be expected in a soft ferromagnet. The 2 K and 25 K isotherms do not have a detectable coercive field. Interestingly, a metamagnetic step-like transition is found in the 2K curve upon increasing the external field. This step is likely due to change in ordering or alignment of the interlayer Co(*en*)$_3$ moments at higher applied fields. A probe of magnetization at the atomic scale such as neutron diffraction would be needed to distinguish the behavior of the Co(*en*)$_3$ species and the CoS layer. At 2 K, the magnetic moment approaches saturation at 0.022 $\mu_B$/Co, which is very small. A similarly small moment and magnetization saturation was shown in the CoSe system.[131] The isotherms at 50 K, 100 K, and 300 K show paramagnetic behavior as expected above the Curie temperature of 42 K.

### 3.3.3 Electrical transport

Figure 3.11 shows the temperature-dependent resistivity for a pressed pellet of as-recovered en-CoS. Although we were able to grow single crystals large enough for XRD studies, we were not able to isolate one suitable for transport measurements. However, pressed pellets of polycrystalline en-CoS exhibit metallic, linear resistivity as a function of temperature over the range from 1.8 K up to 300 K. We did not apply an external magnetic field for these measurements.

There is a clear change in linear behavior around the Curie temperature which is emphasized in Figure 3.11 (inset) by plotting the slope of the resistance curve as a function of temperature. From this derivative, a clear discontinuity is shown at the Curie temperature whereby the slope changes from linear behavior to a power law. The change from linear behavior may be due to an abrupt change in scattering processes below the ferromagnetic transition temperature or changes to the Fermi surface.

The related TTMCs of $KCo_2Ch_2$ and CoSe phases also exhibit metallic behavior arising from the filling of Co d-orbitals at the Fermi level. A deviation was seen in the related $KCo_2Ch_2$ and CoSe phases[65,110] concomitant with their respective ferromagnetic transition temperatures. In the $KCo_2Se_2$ phase,[19] this deviation was much more dramatic and is likely due to the increased Co magnetic moments. We are unsurprised that en-CoS is also a metal since most of the Co-based TTMCs are metallic due to partial filling of the electronic density of states composed by mostly Co *d*-states.

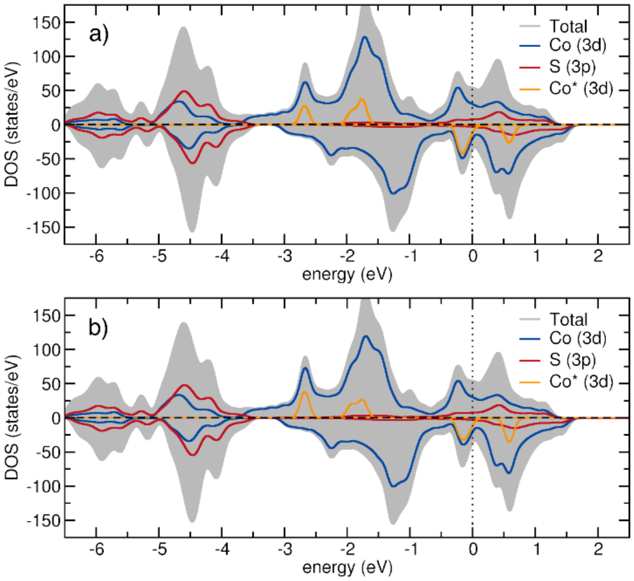

Figure 3.12: Electronic density of states (DOS) for (a) model high symmetry structure with *Pbcn* symmetry and (b) experimental low symmetry structure with $Pca2_1$ symmetry. Co* denotes the intercalate Co atoms.

### 3.3.4 Electronic structure

First principles simulations of en-CoS confirm its metallic ferromagnetic character. We observe a calculated magnetic moment of 0.70 $\mu_B$/Co. We computed multiple AFM orderings for comparison but found that each was at least 0.5 eV/f.u. higher in energy and thus unlikely to be competitive with the FM phase. We computed the electronic density of states (DOS) for the experimental $Pca2_1$ structure as well as the high symmetry *Pbcn* model structure (Figure 3.12). In both cases, we find that the Fermi level falls in the middle of a Co 3*d* band, confirming that the partially filled Co states provide metallic conductivity (Figure 3.10). As expected for a distortion mechanism decoupled from the conduction mechanism, we emphasize that the DOS at the Fermi level is nearly identical between the centrosymmetric and noncentrosymmetric structures. There is a modest redistribution of intercalate Co states under displacement, which we attribute to changes in FM coupling strength between the CoS layers and intercalates.

We observe that the intercalate Co sites appear to be in a high-spin configuration, as evidenced by both the DOS and a calculated moment of 2.12 $\mu_B$/Co. However, our calculations did not include the *en* ligands, which would impact the orbital filling of the intercalated sites.

## 3.4 Discussion

### 3.4.1 Hydrogen bonding

Intercalated metal chalcogenides typically adopt centrosymmetric phases due to the nature of the intercalate. Most guest species are single metal cations or disordered guest molecules. Their interaction with the host species is either an isotropic Coulombic attraction or a weak dispersion force. The title compound en-CoS is rare in that the intercalates are ordered between the CoS layers. The ordering of the Co(*en*)$_3$ complexes not only breaks the tetragonal symmetry inherent in TTMCs (Figure 3.1) but also the inversion symmetry between layers. The cell volume is also increased by a factor of 12 (4*a* x 3*b*) due to this long-range order. What intermolecular force leads to long-range order of the complexes between the CoS layers? Our answer to this question forms the hypothesis of this paper: 1) The Co(*en*)$_3$ complexes engage in hydrogen bonding with the terminal $S^{2-}$ anions in the CoS layers, and 2) the Co(*en*)$_3$ complexes are $C_2$-symmetric, chiral and preferentially bond with CoS layers to break inversion symmetry.

Our group has found evidence that amine intercalation into metal chalcogenides is partially stabilized by the formation of hydrogen bonds.[64,66] The non-conventional, or "weak", hydrogen bond can occur when a strong donor such as O—H and N—H is paired with a weak acceptor.[132,133] The weak acceptor is typically an atom of moderate electronegativity or a π-bond. An example of a species of a moderate electronegativity includes S=C<, $S^{2-}$, or S<. In organic structures, for example, the arrangement of N—H···S=C< is well characterized from crystallographic studies.[34] A simple example is the polymeric structure found in thiourea as it forms infinite N—H···S=C intermolecular chains. Incidentally, the hydrogen bonding network in thiourea leads to ferroelectricity.[134]

We use the empirical rule that the interatomic distances between the hydrogen and acceptor must be shorter than the sum of the van der Waals radii of H and the acceptor (*e. g*. S or Se). This criterion leads to an H···S distance less than 3.00 Å (and 3.10 Å for H···Se). A survey from 1997 by Allen *et al.* on H-bonding provides a histogram of typical distances and angles in organic compounds with S=C and S< acceptors moieties.[135] Allen *et al.* chose 2.9 Å as their van der Waals cut-off. First, N—H donors are roughly five times more common than O—H donors. This points to amino groups being more effective donors for sulfur than hydroxyl groups. Second, the bonding configuration of sulfur is important to consider since the polarity of the covalent bond between the sulfur and the carbon influences distances. For thioketone acceptors (S=C<), the mean distance of H···S is 2.51(1) Å with N—H donors. For thioether acceptors (S<), however, the mean distance increases to 2.75(2) Å. Clearly, how much negative charge lies on sulfur has a big influence on its ability to effectively accept hydrogen. In en-CoS, the Co—S bond must be sufficiently polar then to accept the N—H groups of the *en* ligands.

The classic Werner complex $[Co(en)_3]^{3+}$ is known to participate in hydrogen bonding, which has been exploited for catalysis recently.[116,118] In en-CoS, the H···S interatomic distances from the $Co(en)_3$ complex qualify as hydrogen bonds. The full listing of N—H···S distances are given in Table 3. We chose to set the cutoff to be 2.8 Å where only two bonds are short enough to be plausible hydrogen bonds of moderate strength. The two important bond distances are H···S = 2.410(10) Å and 2.575(10) Å (Table 3.3). When viewed down the [010]-axis, these two hydrogens, H8 and H1, are well aligned with a row of sulfide anions in the CoS layer (Figure 3.13a). The other hydrogen bonds are in the range of 2.73 Å to 2.79 Å, and we do not consider these to play a major role in the formation of the polar space group. A double well potential could describe the configuration of the $Co(en)_3$ complex within the layers, which means that the complex has to 'choose' which sulfide layer to be closer to. In such a case, the equilibrium position is not halfway between the two CoS layers but rather closer to one layer over the other. As can be seen in Figure 3.13, this broken symmetry leads to one hydrogen bond being shorter by 0.165 Å over the other. The N—H···S bond angles listed in Table 3.3 are also in line with the mean bond angles found by Allen et al. for organic molecules with 142(2)° for thioethers and 157(1)° for thioketones.[135]

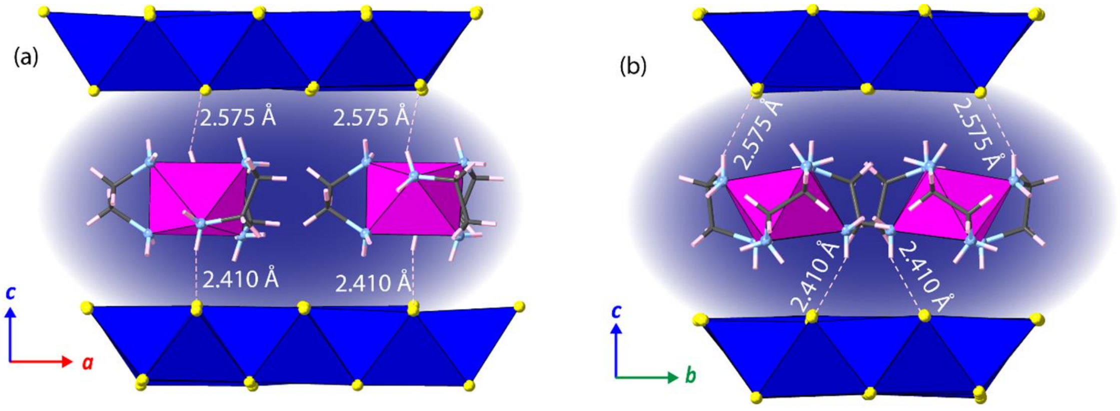

Figure 3.13: The two N—H…S hydrogen bonds that determine the polarity of en-CoS from single crystal structure. (a) View along the [010] zone axis, where the two closest hydrogen bonds to the sulfide layer from the $[Co(en)_3]^{2+}$ complex

occur through two N—H groups above and below the complex. By choosing one closer hydrogen bond over the other, the structure breaks inversion symmetry. (b) View along the [100] zone axis demonstrates how the hydrogen bonds lead to a bending of the CoS layers along a direction parallel to the [001] axis.

The free *en* molecule also participates in hydrogen bonding since the closest H···S distances is 2.659(11) Å. This short distance occurs for one end of the free *en* molecule. The other end of the free *en* molecule is disordered, and the H···S distances exceed 2.8 Å. We therefore do not consider the disordered end of the *en* molecules to engage in hydrogen bonding. The packing of both molecules is likely influenced by intermolecular forces such as maximizing the hydrophobic interactions of the hydrocarbon backbones of the *en* molecules, both as ligands and uncoordinated solvent of crystallization.

Table 3.3. Hydrogen bond distances (Å) and bond angles (°) for the Co(*en*)$_3$ complex in [Co(*en*)$_3$]Co$_{12}$S$_{12}$·*en*. Only hydrogen bonds that are at least 93.3 % of the sum of the van der Waals radii of H and S are included. Atom labels can be found in Figure S9.

| | |
|---|---|
| H8 — S2 | 2.410(10) |
| H1 — S10 | 2.575(10) |
| H12 — S7 | 2.659(11) |
| H4 — S1 | 2.725(11) |
| H9 — S6 | 2.753(10) |
| H5 — S11 | 2.793(10) |
| ∠ N8 — H8···S2 | 149.11 |
| ∠ N1 — H1···S10 | 142.47 |

### 3.4.2 Role of metal-amine complex

The solvothermal synthesis in chelating amines has led to successful crystal growth of a plethora of hybrid materials. In particular, transition metal amine complexes can be inserted in group 13, 14, and 15 chalcogenides through this synthetic strategy. The work of Bensch[136-138] and Dai[139-143] has demonstrated how such coordination complexes can act as structure directing agents for inorganic semiconductors. Recently, Kovnir et al have demonstrated that [Fe(*en*)$_3$]$^{2+}$ complexes can intercalate along with neutral *en* molecules in layered iron sulfides related to superconductors.[142]

The classic Werner complex $[Co(en)_3]^{3+}$ is chiral, which arises from the bidentate nature of the chelating *en* ligand. We note that our complexes are slightly different from that of Werner since ours contains divalent Co ($d^7$) whereas those studied by Werner were trivalent Co ($d^6$). The complex is either the right-handed, Δ-enantiomer, or the left-handed, Λ-enantiomer. Nevertheless, the structure remains polar and is not chiral-polar since both enantiomers are present.

The orientation of the ethylene ($CH_2CH_2$) backbone leads to stereoisomers of the enantiomers. Since the $Co(en)_3$ complexes are ordered in the layers, we were able to assign the chirality of each of the four complexes within the unit cell. As Figure 3.15 shows, the two enantiomers are nearest neighbors and are related to each other by the *a*-glide plane. Consequently, en-CoS contains an equal mixture of right-handed and left-handed enantiomers within each intercalated layer.

The point group symmetry of each $Co(en)_3$ complex is not $D_3$ but rather $C_2$. This lowering of symmetry for both the Δ- and Λ-enantiomers arises from the conformation of the *en* ligand rings. Since they are not planar, each ring can be either left-handed (λ) or right-handed (δ), and which label we apply depends on the enantiomer. For example, the Δ-enantiomer has two rings where the C—C bond is parallel to the $C_3$ axis of the octahedral complex and one ring that is oblique to it (Figure 3.15). This gives it then the label δ for the oblique ring and λλ for the two parallel rings. The $Co(en)_3$ complexes in en-CoS are therefore Δ-δλλ and Λ-λδδ as labeled in Figure 3.15. While the lower energy Δ-λλλ and Λ-δδδ isomers would have retained the dihedral $D_3$-symmetry, the change of one of the *en* ring conformations lowers it to be $C_2$-symmetric.[117]

### 3.4.3 Polar metals

A ferroelectric material exhibits spontaneous polarization of a material upon cooling through a transition temperature.[145,146] Furthermore, one should expect to manipulate the polarization through the application of an external electric field. Such switchability allows for a variety of applications including sensing and memory storage in ferroelectrics. The same attributes apply to ferromagnets, ferroelastics, and other ferroic materials.[147-149] What such polarity means in the context of a metallic conductor, however, is still an open question. Benedek and Birol caution against use of the term ferroelectric metal in the manner Anderson and Blount had applied to $V_3Si$.[150] Without a measurable change in polarization of the material through a transition temperature, the concept of ferroelectricity may not be appropriate for any metallic conductor. Even with the continuing debate on whether ferroelectricity can exist within a metal, it is apparent that polar metals themselves are promising quantum materials.

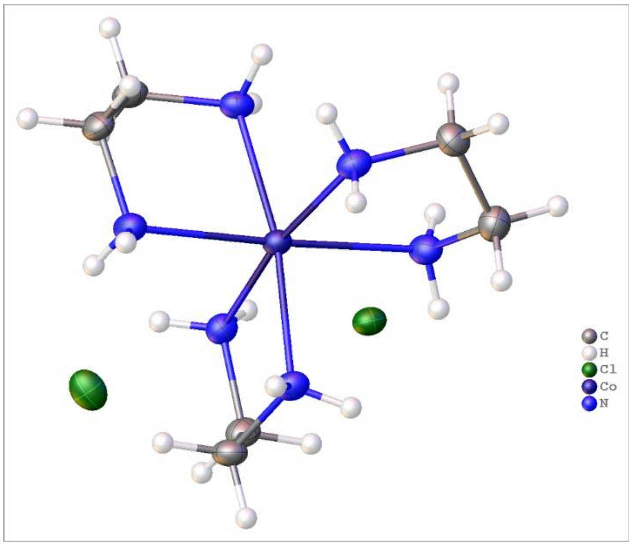

Figure 3.14: Crystal structure of $[Co(\mathit{en})_3]Cl_2$. The divalent complex crystallizes in yellow needles with chloride anions. This is the side product to the main phase, the title compound $[Co(\mathit{en})_3](CoS)_{12} \cdot \mathit{en}$.

We place our findings on en-CoS in the context of known polar metals. The most recent advances in the field of polar metals have focused on transition metal oxides and layered $WTe_2$. Although many groups first focused on electron doping of known ferroelectric materials such as $BaTiO_3$,[150,151] they were not able to conclusively establish that microphase separation was behind the simultaneous observati [100] on of metallic conductivity and ferroelectricity. Not until 2013, with the work of Shi *et al.*, did the ferroics community find an unambiguous example of a ferroelectric metal. Shi *et al*. prepared metallic $LiOsO_3$ through a high-pressure method, and by cooling it below 140 K, they uncovered a second-order phase transition from $R\bar{3}c$ to $R3c$. Subsequent groups report that a $Li^+$ cation order-disorder transition rather than a $Li^+$ ferroelectric displacement drives the breaking of inversion symmetry.[152] Liu *et al.* posit that a double well potential exists for the Li site in $LiOsO_3$,[153] and below 140 K, the system breaks inversion symmetry by falling into one of the two minima. A similar double well potential could likewise describe the orientation of the Δ-δλλ and Λ-λδδ enantiomers of Co(*en*)$_3$. In the case of en-CoS, the double well could be caused by hydrogen bonding of the complexes rather than electrostatics as in $LiOsO_3$.[165]

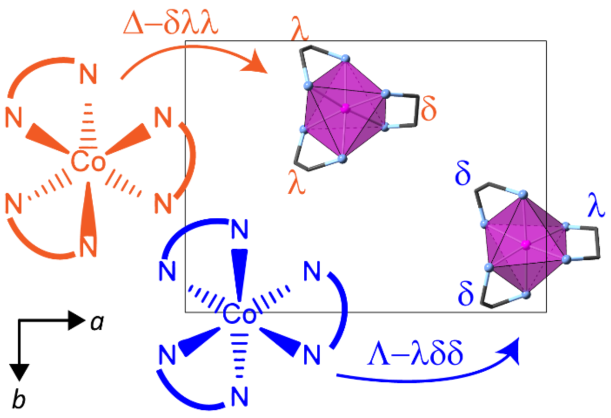

Figure 3.15: The chiral [Co(*en*)$_3$]$^{2+}$ complexes in en-CoS. The two enantiomers, Δ and Λ, have the same conformations for the ethylene backbone. They are found within the same gallery between the CoS layers. Hydrogen atoms of the en molecule are not shown for clarity.

The polar metal that may be closest to en-CoS, however, is $WTe_2$, a transition metal dichalcogenide. $WTe_2$ adopts the polar orthorhombic group $Pmn2_1$ (space group no. 31) on the so called 1T' structure. Note that this polar orthorhombic group also belongs to the same Laue group $mm2$ as $Pca2_1$, which we find for our compound. Unlike other TMDs that are also polar, $WTe_2$ is not a semiconductor but a Weyl semimetal. Like the example of $LiOsO_3$, $WTe_2$ appears to be a plausible example of a ferroelectric metal since its polarization can be switched by application of an electric field. Fei *et al.* first demonstrated this switchability in films of $WTe_2$,[153] and Sharma *et al.* soon demonstrated the same effect in bulk single crystals.[154] A proposed mechanism for its polarity is also a double well potential, which arises from how the $WTe_2$ layers slip with respect to one another. Such double-well potentials may be a general way to understand how metallic compounds can break inversion symmetry to become polar.

### 3.4.4 Band ferromagnetism in en-CoS

The title compound stands apart from the previously discussed polar metals in that it is the only known ferromagnet. The effective moment size indicates itinerant magnetism rather than localized moments in the CoS layers. Nominally, each Co center is close to a valence of $2^+$ and therefore is either tetrahedral $d^7$ in the CoS layers or octahedral $d^7$ in the $[Co(en)_3]^{2+}$ complexes. The tetrahedral Co center would be $S = 3/2$ for either low spin or high spin configuration. For high spin Co in the octahedral complexes, the value for spin would also be 3/2. This spin configuration is likely for $[Co(en)_3]^{2+}$ and would lead to an effective moment of 3.87 $\mu_B$. If we take into account all 13 Co atoms per formula unit of $[Co(en)_3](CoS)_{12}$, then we measured a total effective moment of 0.289 $\mu_B$ per Co center. The positive Weiss field ($\theta = 51$ K) would indicate that Co centers are ferromagnetically coupled to each other.

Past studies on cobalt chalcogenides also point to itinerant ferromagnetism in en-CoS. Greenblatt *et al.* worked extensively on $AM_2Ch_2$ compounds where $A$ = electropositive metal such as $Tl^+$ or $K^+$, $M$ = Mn, Fe, Co, Ni, and Cu and $Ch$ = S or Se.[113,130,156-160] They found long-range magnetic order for the Co-based compounds along with metallic conductivity. For the compounds that are ferromagnetic metals, Greenblatt found their $T_C$'s to be relatively high (> 100

K). For example, $TlCo_2S_2$ is a ferromagnet with a $T_C$ of 152 K where an anomaly occurs in the resistivity just as we found in our compound near its $T_C$.

Two factors affect the moment size in these Co-based TTMCs. The first is interlayer distance, and the second is electron doping into the Fermi level. Greenblatt and Huan found that in $Tl_{1-x}K_xCo_2Se_2$ for $0.55 < x < 1.0$ the *c*-parameter, which controls interlayer distance, increases as $K^+$ substitutes $Tl^+$. Consequently, the $T_C$ and effective moment drop with more $K^+$. A more dramatic change is seen when anion substitution is employed as Guo *et al.* did in their study of $KCo_2Se_{2-x}S_x$ for $0 \leq x \leq 2$. $T_C$ decreases from 120 K to 82 K for $x = 2$ and 0, respectively.[160] We conclude from these past studies that the interlayer distance of nearly 10.05 Å in en-CoS should lead to a small effective moment and low $T_C$.

Since Co-based TTMCs are band ferromagnets, their Fermi surfaces play a role in their magnetic properties. Ronneteg *et al.* calculated the electronic DOS of the ferromagnet $TlCo_2S_2$ and found that the Fermi level ($E_F$) traverses the valence band where it exhibits narrow-band features.[161] By allowing for spin polarization of the DOS, Ronneteg *et al.* find that the system reaches an energetically favorable state when one spin-polarized DOS is lowered with respect to the other. Furthermore, they calculate the Crystal Orbital Hamilton Population (COHP) of the DOS and find that the $E_F$ lies in Co—Co antibonding states, which leads to an electronic instability favoring ferromagnetism. In our previous study of tetragonal CoSe and CoS,[86,131] we also found that $E_F$ lies in near an antibonding peak in the COHP, which would explain why these Co-based materials tend to be band ferromagnets.[86]

Electron doping also plays a role in moment size. In the structurally related $Eu_{1-x}Ca_xCo_2As_2$, the doping level is about 1.0 $e^-$ per Co center.[162,163] From neutron diffraction studies, the moment size is 0.27(6) $\mu_B$ per Co. In our compound, we are likely underfilling the DOS leading to a small moment. Each $Co(en)_3$ complex contributes 2 $e^-$ per formula unit, and since there are 12 Co in the CoS layer, this leads to doping of about 0.167 $e^-$ per Co center.

To better understand the effects of electron doping, we present a series of calculations simulating CoS layers (i.e. without intercalated Co atoms or *en* complexes) fixed to their positions derived from the XRD measurements as a function of electrostatic doping. As shown in Figure 3.16, the calculated magnetic moment increases as the doping concentration increasing, only plateauing at about 0.5 $e^-$ per Co center, well above the approximate number donated by Co(*en*)$_3$ complexes. This supports the observation that the Co orbitals in en-CoS are likely underfilled and implies that the CoS layers contribute strongly to the observed magnetic moment.

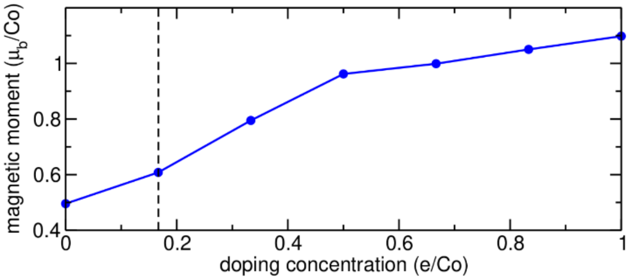

Figure 3.16: Calculated magnetic moment per Co site under electrostatic doping as computed for CoS layers (no intercalated Co sites). The dashed line indicates approximate doping of the CoS layers in [Co(*en*)$_3$](CoS)$_{12}$.

In addition to the small moment, our compound also shares another characteristic with the Co-based compounds—it is a soft ferromagnet. en-CoS expresses almost no discernible hysteresis in the M vs. H curves (Figure 10). The magnetization saturates at 7 T and 2 K, and the total moment is close to 0.022 μB per Co, which is about an order of magnitude smaller than in the other compounds. This small total moment would be in line with our findings that the large interlayer spacing (>10 Å) and low amount of electron doping decrease the ferromagnetic signal compared to other Co-based compounds. The detailed magnetization studies of $ACo_2Se_2$ (for A = K, Rb, and Cs) by Yang et al. demonstrate that these materials are best understood as weakly ferromagnetic systems.[165]

## 3.5 Conclusions

We hypothesize that coordination complexes of the type $ML_n$, where there are $n$ number of amine-based ligands $L$, could be combined with either layered TTMCs or TMDs to form unique hybrid materials. In this paper we chose one of the simplest bidentate ligands, *en*, but in future studies one could also introduce other multidentate ligands such as diethylenetriamine and triethylenetetramine. Indeed, the groups of Kovnir[164] and Johrendt[165] have already used such complexes to form a series of chain-like iron chalcogenides. Our goal is to extend this to a variety of layer-type chalcogenides beyond iron. Through synthetic design, one could go beyond polar metals and form chiral metals or even polar-chiral metals. More work also needs to be done to elucidate the full physics of the polar metallicity in en-CoS. Polar materials should exhibit second harmonic generation (SHG) behavior.[129,167] The implications of such non-centrosymmetric materials for applications of quantum materials are tantalizing.

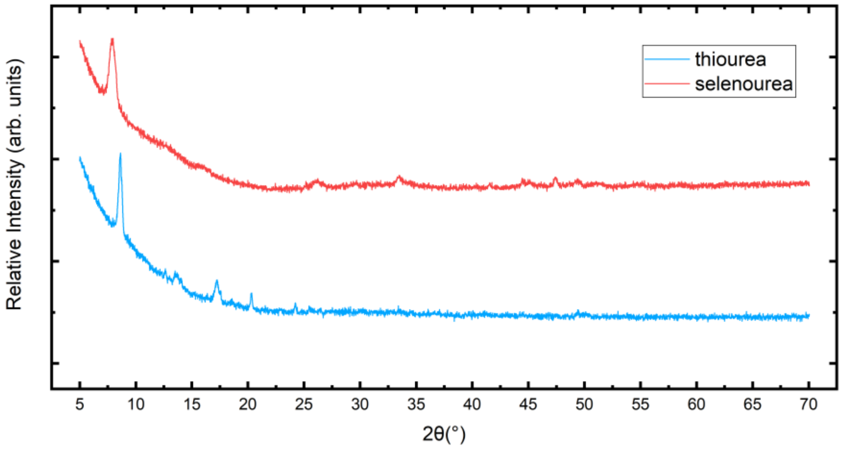

Figure 3.17: The powder XRD patterns of ground polycrystalline samples of the solvothermally prepared products with two different chalcogen sources. Patterns were collected at room temperature.

Finally, we draw some comparisons to iron-based superconductors and the title compound. There are two coincidences between the $[Li_x en_y](FeSe)_2$ superconductor and $[Co(en)_3](CoS)_{12}$ that bear mentioning. First, the level of charge doping. In the phase diagram of the FeSe-based superconductor, the amount electron doping that maximizes the critical temperature is about 0.15 $e^-$ to 0.20 $e^-$ per Fe center.[64,112,168-176] In the title compound, we achieve 0.167 $e^-$ per Co center in electron doping. Second, the transition temperatures. The maximum critical temperatures in bulk intercalated FeSe superconductors ranges between 42 K and 45 K. The Curie temperature of the title compound is 43 K. Finally, the iron-based superconductors such as FeSe and BaFe2As2 are known to undergo orthorhombic distortions.[177,178] In the case of en-CoS, this orthorhombic distortion is not only driven by ordering of the $Co(en)_3$ but also in an orthorhombic distortion of the CoS TTMC layer. Using an order parameter $\delta = (a—b)/(a+b)$, en-CoS shows one close to 8(1) $\times 10^{-4}$ (here $a$ and $b$ are the parameters of the pseudo-tetragonal cell). In comparison, $\delta = 2 \times 10^{-3}$ and $1.5 \times 10^{-3}$ for superconducting FeSe and $BaFe_{2-x}Co_xAs_2$, respectively.The striking similarities in the crystal chemistry and underlying physics point towards universal behavior among TTMCs. By continuing to synthesize more hybrid TTMCs and carrying out careful structural studies, we hope to find the clues that will explain the emergence such unconventional properties.

# Chapter 4: Chiral amine intercalations into TMDs

## 4.1 Introduction

In the previous chapter, we showed that inserting racemic mixtures of chiral $Co(en)_3^{2+}$ complexes into layered hosts can yield polar but non-chiral metallic structures, where inversion symmetry is broken but overall chirality is absent due to the coexistence of Δ- and Λ-enantiomers.[179] This raises a compelling question: What if one could intercalate an enantiopure chiral molecule rather than a racemate? Would such a structure realize a true chiral crystal, and further could this promote chiral or topologically nontrivial electronic states and even lead to some intriguing quantum properties such as the chiral superconducting pairing symmetry?

Superconductivity arises from the formation of bound electron pairs—Cooper pairs—that condense into a macroscopic quantum state with long-range phase coherence. In most conventional superconductors, such as elemental metals, the pairing is mediated by phonons and exhibits s-wave symmetry, where the superconducting gap is isotropic across the Fermi surface. However, in many layered or strongly correlated materials, the pairing mechanism can deviate from this picture, giving rise to unconventional pairing symmetries such as p-wave or d-wave, where the superconducting gap exhibits anisotropy or even nodes in momentum space[180]. These unconventional states often break additional symmetries, including time-reversal or rotational symmetry, and are of great interest due to their potential to host topologically nontrivial electronic states.

The symmetry of the pairing function is intimately tied to the symmetry of the underlying crystal lattice. In particular, the absence of inversion symmetry in non-centrosymmetric superconductors can lead to mixing of spin-singlet and spin-triplet components, resulting in complex gap structures and new emergent phenomena.[195] This has motivated a growing effort to explore whether structural modifications, especially those involving chiral or polar order, can influence the nature of superconductivity in layered materials. In particular, theoretical work has shown that conventional s-wave superconductors, when interfaced with topological insulators or non-centrosymmetric systems with strong spin–orbit coupling, can support effective p-wave pairing and even host Majorana bound states. [181-183]

A particularly intriguing manifestation of unconventional superconductivity is the breaking of time-reversal symmetry (TRSB). In TRSB superconductors, the Cooper pair wavefunction acquires a complex phase, such as in $p_x+ip_y$ state, which can result in spontaneous currents, internal magnetic fields, and topologically nontrivial excitations.[184-187] These complex order parameters typically arise in systems with multicomponent representations of the crystal point group and are favored in lattices with reduced symmetry—particularly those lacking inversion or mirror symmetry.[180, 186,195]

Experimental signatures of TRSB include the emergence of zero-bias conductance peaks, anomalous Josephson effects, spontaneous magnetization, or direction-dependent critical currents. In recent years, TRSB has been observed or suggested in several candidate materials, including $Sr_2RuO_4$, $UPt_3$, $UTe_2$, and more recently, organic superconductor κ-(BEDT-TTF)$_2$Cu(NCS)$_2$ with chiral structures.[194] These observations raise the possibility that structural chirality could influence the symmetry of the pairing state in ways that favor time-reversal symmetry breaking when introduced into a superconducting system.

An additional mechanism by which molecular chirality may influence superconductivity is through the chiral-induced spin selectivity (CISS) effect. CISS describes the phenomenon whereby chiral molecules preferentially transmit electrons of a given spin orientation, generating spin-polarized currents without requiring magnetic fields or ferromagnetic materials[188,189,192] This effect is attributed to the interplay between the chiral geometry of the molecule and spin–orbit coupling of the host structure, leading to spin-dependent transport even in nonmagnetic, room-temperature systems.

Importantly, recent studies have extended the relevance of CISS into solid-state and superconducting systems. For example, Bian et al. demonstrated that chiral amine intercalation into layered $MoS_2$ induces strong spin polarization in charge transport. Nakajima et al. reported spin-polarized Cooper pairs in an organic chiral superconductor, implying that CISS-related mechanisms may couple directly to the superconducting condensate[190,194]. These findings suggest that chirality may not only break spatial symmetries but also influence the spin structure of the pairing state, potentially favoring unconventional or TRSB superconductivity.

In light of these developments, we explored the intercalation of a series of amine molecules—including ethylenediamine (*en*), racemic methylbenzylamine (rac-MBA), (S)-α-methylbenzylamine (S-MBA), and (R)-α-methylbenzylamine (R-MBA)—into the layered transition metal dichalcogenide 2H–$TaSe_2$. These amines offer progression from achiral to enantiopure chiral molecular structures, allowing us to systematically probe the role of molecular symmetry. Upon intercalation, we observe clear superconducting transitions in DC magnetic susceptibility measurements, indicating that the chiral compounds retain or induce superconductivity. These results establish a foundation for further investigating how molecular chirality, steric effects, and symmetry breaking may influence the superconducting state in such hybrid layered materials.

## 4.2 Experimental

### 4.2.1 Sample Synthesis.

Polycrystalline powder $TaSe_2$ was first synthesized as the host structure material. We mixed tantalum (Alfa Aesar, 99.5%) and selenium powder (Alfa Aesar, 99.5%) in 1:2 molar ratio with a total mass of ~2 gram in a quartz ampoule, which was later evacuated and sealed with a hydrogen torch flame. The sealed ampule was heated up to 700 ℃ where it stayed for 1 hour, and then the temperature was increased to 900 ℃ for 5 days. The mixture was afterwards furnace-cooled to room temperature. To improve homogeneity of the product, the resulting powders were ground in an agate mortar and reheated at 900 ℃ for another 5 days.

Through the solvothermal reactions, we performed the intercalation of the selected amines into the layered TMD hosts by using the respective amines as the solvents. All the amines were purchased from Sigma-Aldrich.

*en*- $TaSe_2$. For the typical preparation of the compound, ~2 mmol of $TaSe_2$ powders from the previous process were suspended in 20 mL of ethylenediamine (99.0%) in a 47-mL Teflon cup. The Teflon cup was then sealed in argon-filled glove box to ensure the reaction system was sealed in an oxygen-free atmosphere. The sealed Teflon cup was packed within a stainless steel autoclave and heated at 80 ℃ to 120 ℃ for 2-3 days. The autoclave was air-cooled to room temperature after the heating process and the solid product inside the Teflon cup was washed with ethanol and decanted. If the powders were still suspended in the solvent, then we centrifuged to better isolate the product. The resulting samples were then collected, vacuum dried and stored in argon-filled glovebox for further characterization.

RMBA-$TaSe_2$. Similar preparations as described above by suspending ~ 2 mmol of the $TaSe_2$ powders in 20 mL of R-(+)-methylbenzylamine (98.0%) liquid in a 47-mL Teflon cup. However, ~0.05 to ~0.1 mL of ethylenediamine were added into the mixture. The difference of the reaction with and without this relatively small amount of ethylenediamine will be discussed later in the next section. The Teflon cup was sealed in inert environment within a stainless steel autoclave, which was then heated to 120 °C and kept there for 2 to 3 days. After the completion of the solvothermal reactions, the autoclave was cooled down to room temperature in air and the contents were recovered and washed with ethanol.

SMBA-TaSe2 and racemic-MBA-TaSe2. The synthesis procedure for SMBA or racemic intercalated was identical to that described above for RMBA-TaSe2, except that racemic α-methylbenzylamine (98.0%) or (S)-(-)-methylbenzylamine (98.0%) was used in place of (R)-(+)-methylbenzylamine.

### 4.2.2 Diffraction studies.

Powder x-ray diffraction (XRD) patterns were collected using a Bruker D8 Advance X-ray diffractometer supplied with Cu $K_\alpha$ radiation ($\lambda$ = 1.5418, 2 θ = 5° to 70 °). We typically used a step size of 0.020° and scanning time of 0.50 seconds per degree.

*Magnetic measurements*. We preformed temperature and field dependent direct current (DC) magnetization measurements through a Quantum Design Magnetic Property Measurement System (MPMS3). The sample powders as mentioned above were placed individually in a gel capsule which was then inserted into a plastic straw holder. This process of sample preparation has already been described in Chapter 2: Methods. A zero field-cooling (ZFC) measurement was conducted first, where the temperature decreased from 300 K to 1.8 K under no applied field, and the samples were then heated back to 300 K under a small, applied field (100 Oe). Then, the sample is cooled back down to base temperature under a field-cooled (FC) state. In the same instrument, we later carried out isothermal magnetization measurements at a series of temperature (300 K, 120 K, 20 K and 2 K) with applied fields between $H = \pm 7$ T. Since we still have a full understanding of the structure of the intercalated samples, we remain applying the molar mass of $TaSe_2$ and $NbSe_2$ when magnetization was converted to molar magnetic susceptibility and magnetic moment (in Bohr magnetons).

### 4.2.3 Resistivity measurements.

We used a Quantum Design Physical Property Measurement System (PPMS-9T) for the electrical resistance measurements. The size of one single crystal from the polycrystalline products does not meet the minimum requirements of the electrical resistance measurements and therefore it is a challenge to directly measure the resistivity of one single crystal of the samples. Instead, electrical resistance of a pellet of the samples was measured. The powder samples were first ground in an agate mortar and were pressed into a round pellet under 2000 psi of uniaxial stress. We dynamically pumped on the die apparatus to form a pellet in order to ensure the uniform density of the pellet during the process. The diameter of the round pellet was ~ 1 cm and the thickness was ~0.5 mm. Then we mounted the pressed pellet on the center of a specialized puck with 3 channels. The four-point probe techniques were applied at all the three channels by attaching silver wires onto the pressed pellet with silver paint. We conducted temperature dependent resistance measurements from 1.8 K to 300 K upon an applied current of 0.1 mA and without magnetic field.

### 4.2.4 Circular dichroism study.

The circular dichroism measurements were conducted with Jasco J-810 Spectropolarimeter. ~0.1 gram of the as-recovered ground powders was dispersed into ~20 mL ethanol and the liquid was sonicated for 20 minutes to form a stable suspension for the measurements. The selected wavelength of the measurements is from 800 nm down to 200 nm with a scanning rate of 40 nm per minute. Background was first measured with a quartz cuvette only filled with ethanol, and then the liquid is changed to the suspension mentioned above. Nitrogen gas was kept purging in the chamber where the cuvette was placed to remove dust and moisture which may undermine the measurements in the far-UV range.

### 4.2.5 Thermogravimetric analysis measurements.

We conducted the TGA measurements through a TA-Q500 mainly to explore the stability and decomposition process of the intercalated transition metal dichalcogenides. Around 10 mg of the as-recovered samples was placed in a platinum pan. The temperature was increased from 40 °C to 800 °C at a ramp of 10 °C per minute in nitrogen atmosphere.

## 4.3 Results and discussion

### 4.3.1 Synthesis and crystal structures.

The intercalation of ethylenediamine (*en*) into layered transition metal dichalcogenides such as 2H–$TaSe_2$ was first reported in the late 1970s by Tsang et al. In their method, $TaSe_2$ single crystals were sealed together with liquid ethylenediamine in a quartz tube and heated at 150 °C for several weeks, enabling intercalation under the autogenous pressure of the solvent, which could be regarded as a solvothermal reaction. However, our experiments show that such intercalation could be achieved under milder conditions. The peak shift from ~14.8° to ~8° of 2θ in powder X-ray patterns in Figure 4.2 displays that the solvothermal insertion of ethylenediamine could be even carried out at 80 °C over the course of only 2 days. 80 °C is lower than the boiling point of ethylenediamine and therefore the reaction is not in the narrow sense of the definition, a solvothermal reaction as we have discussed in Chapter 1.

Besides $TaSe_2$, the research relevant to *en* intercalated $NbSe_2$ is also widely reported. These results indicate that ethylenediamine is a very effective intercalant for van der Waals layered compounds. The ease with which ethylenediamine intercalates into TMDs under mild solvothermal conditions can be attributed to a combination of favorable molecular and thermodynamic factors. First, ethylenediamine is a small bidentate molecule with two terminal $-NH_2$ groups, allowing it to engage in weak coordination or hydrogen bonding interactions with the $TaSe_2$ layers. This enhances its affinity for the van der Waals gaps and may lower the energy barrier for intercalation. Second, ethylenediamine's compact molecular size (~5 Å) enables it to penetrate the narrow interlayer space without requiring significant structural distortion or high thermal activation. The short chain structure of ethylenediamine allows the molecule to have multiple conformations, which also lower the difficulties of intercalation. Typically for $TaSe_2$, the strong polarity of ethylenediamine facilitates interactions with local charge distributions, defects, or dipoles present within the host lattice—especially relevant in materials exhibiting charge density wave behavior.

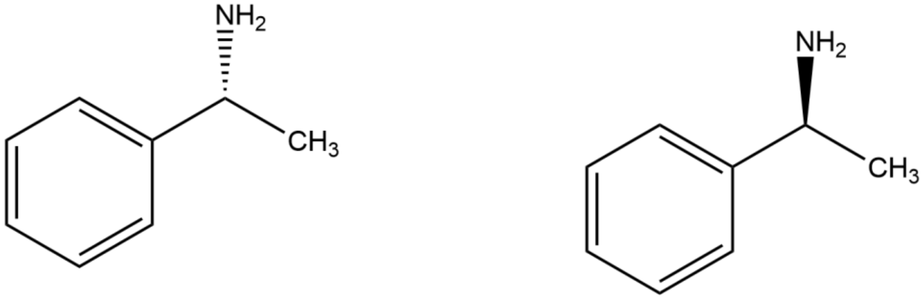

Figure 4.1: Molecular structures of enantiopure α-methylbenzylamine derivatives: (left) R-α-methylbenzylamine (R-MBA) and (right) S-α-methylbenzylamine (S-MBA).

Compared to ethylenediamine, the intercalation of α-methylbenzylamine (MBA), either racemic or chiral, into TMDs has been less frequently reported, and when successful, typically requires significantly longer reaction times or more forcing conditions. Recently, Duan et al. reported the chiral MBA intercalation into 2H-$TaS_2$ through a synthesis in inert $N_2$ atmosphere for

120 hours and into 1T-$TaS_2$ for even 28 days. [196,197] These results suggest that MBA is considerably more difficult to intercalate into TMDs than ethylenediamine. This difference can be attributed to several structural and chemical factors. Due to its benzene ring, MBA is a bulkier and more rigid molecule compared to ethylenediamine, which imposes constraints on its conformational adaptability. Unlike the linear and flexible ethylenediamine, which can readily adopt different conformations to fit within the confined van der Waals gaps, MBA must overcome greater steric and packing barriers during the intercalation. Besides, MBA only has a single -$NH_2$ group. Its reduced polarity and limited hydrogen bonding capability may result in weaker interactions with the host layers, offering less thermodynamic driving force for intercalation. The larger size and lower diffusivity of MBA molecules can also slow the kinetics of interlayer penetration, which may demand longer reaction times or more forcing conditions to achieve complete intercalation.

In our initial batch of solvothermal MBA intercalation experiments, we reacted the $TaSe_2$ polycrystals with R-MBA as the solvent neat. The powder X-ray patterns of the products indicate that intercalation succeeded based on the peak shifts. However, attempts to reproduce the results in subsequent batches were unsuccessful. Even though we increased the reaction time from 3 days to 7 days or increased the temperature from 120 °C to 180 °C, the expected left shift of the (002) peak was not observed again. The liner containers of the solvothermal apparatus we applied here were Teflon cups. In Chapter 1, we mentioned that Teflon materials are abundant of pores, which can easily absorb molecules in the solvents involved. Before our first batch of MBA intercalation, the Teflon cups were used for ethylenediamine reactions. Although the Teflon cups were cleaned with the standard operating procedure before the change to the different solvent, the aging of the Teflon cups would increase the number of pores and ethylenediamine could remain in the inner wall of the cups. Therefore, the residue of ethylenediamine may play an important role in the intercalation of MBA.

To test our hypothesis of ethylene contamination if the first experiments, we conducted a series a controlled synthesis. First, a separate batch of MBA intercalation reactions were conducted in freshly replaced Teflon vessels that had no prior exposure to ethylenediamine to eliminate the possibility of ethylenediamine contamination. Once again, we observed no peak shift in the PXRD patterns, suggesting that no intercalation occurred in the absence of residual ethylenediamine. Then we reused the same Teflon cup and intentionally added a small amount of ethylenediamine into the

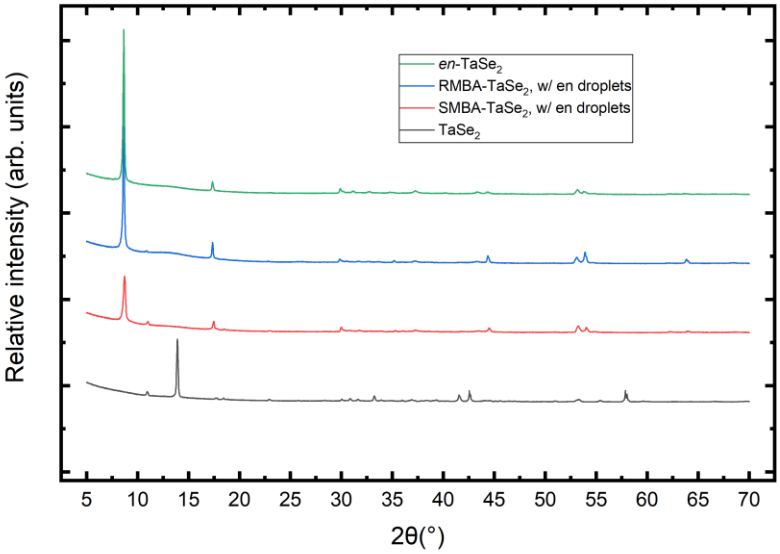

Figure 4.2: Powder X-ray diffraction (XRD) patterns of pristine TaSe$_2$ (black), ethylenediamine-intercalated TaSe$_2$ (en–TaSe$_2$, green, synthesized in 2days at 80°C), and MBA-intercalated TaSe$_2$ samples prepared with trace amounts of ethylenediamine: RMBA–TaSe$_2$ (blue, 3days at 120°C) and SMBA–TaSe$_2$ (red, 3 days at 120°C). All intercalated samples exhibit a clear shift of the (00l) reflections toward lower angles compared to pristine TaSe$_2$, indicating an expansion of the interlayer spacing due to successful molecular insertion. The peak positions of RMBA– and SMBA–TaSe$_2$ are nearly identical to that of en–TaSe$_2$, suggesting a similar degree of interlayer expansion, likely facilitated by the presence of ethylenediamine during synthesis. These structural features are consistent with mixed intercalation and support the role of ethylenediamine as a co-intercalant or promoter.

MBA solution as described in the previous Synthesis section. Interestingly, under otherwise identical conditions, a clear peak shift reappeared in the resulting PXRD pattern. This result supports the hypothesis that a trace amount of ethylenediamine may facilitate or promote the intercalation of MBA into $TaSe_2$. Given the high intercalation efficiency of ethylenediamine discussed earlier, the observed promotion effect of trace ethylenediamine on MBA intercalation likely arises from its ability to transiently modify the interlayer environment of $TaSe_2$. Even in small quantities, ethylenediamine may locally expand the interlayer spacing or weaken the van der Waals interactions between $TaSe_2$ layers, thereby reducing the steric and energetic barriers that hinder the insertion of bulkier, less flexible molecules like MBA. In this context, ethylenediamine may serve as a transient structural opener or intercalation initiator, priming the lattice for subsequent incorporation of MBA. This effect is especially relevant given that MBA, on its own, exhibits limited intercalation under the same conditions. For convenience, we still use the term MBA-$TaSe_2$ or such to refer to the TMDs reacting with methylbenzylamine in this dissertation, although the layered structure chalcogenides may be co-intercalated with both MBA and ethylenediamine.

However, we must note that the powder X-ray diffraction patterns of the MBA–$TaSe_2$ sample prepared with trace amounts of ethylenediamine exhibit nearly identical peak shifts to those observed in the pure *en*–$TaSe_2$ intercalate. This similarity suggests that PXRD can only demonstrate that the intercalation has indeed occurred but does not conclusively demonstrate that MBA is solely responsible for the observed structural expansion. Given the strong intercalating ability of ethylenediamine, it remains possible that the peak shift is dominated by residual or trace amount of ethylenediamine, rather than MBA itself. The most direct way to address the problem is to solve the crystal structures of those amine intercalated $TaSe_2$ samples through single crystal diffraction, just as we did for *en*-CoS in Chapter 3. Although the crystallinity of amine intercalated $TaSe_2$ meet the requirement, unfortunately, the plates of the crystals tended to twin with each other and a single crystal failed to be separated.

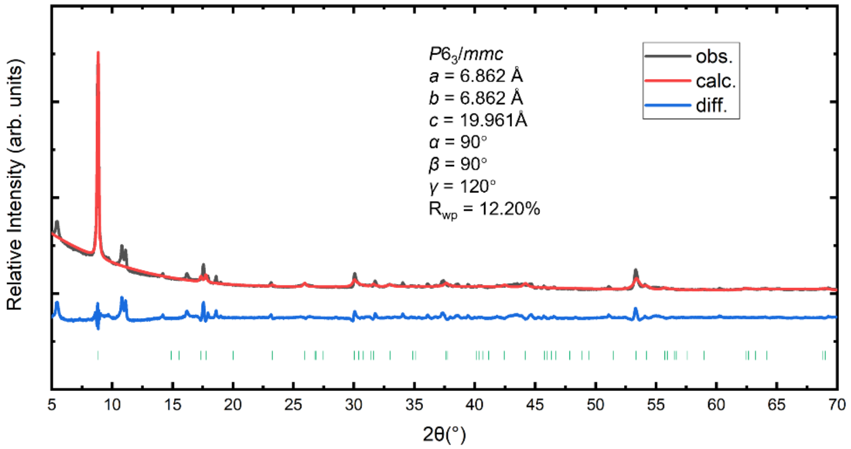

Figure 4.3: Le Bail refinement of the neutron diffraction pattern of the ethylenediamine intercalated $TaSe_2$ sample. The observed data (black), calculated profile (red), and difference curve (blue) are shown.

To further support the presence of MBA in the intercalated product, we performed circular dichroism (CD) and thermogravimetric analysis (TGA) measurements of the samples where chiral MBA is involved in the reactions. As shown in Figure 4.4, the CD spectra of SMBA–$TaSe_2$ and RMBA–$TaSe_2$ (Figure 4.4b) retain approximate mirror-image features that qualitatively resemble those of the corresponding free molecules in solution (Figure 4.4a), although with diminished intensity due to the restrains of the chiral molecules between the layers. The CD signals are centered in the 200–300 nm region, which is consistent with $\pi$–$\pi$* electronic transitions of the aromatic ring in MBA, perturbed by the chiral carbon center. The fact that these spectral features are preserved after intercalation suggests that the MBA molecules remain structurally intact and retain their absolute configuration within the host lattice. Furthermore, the observation of opposite Cotton effects for SMBA- and RMBA-intercalated samples provides compelling spectroscopic evidence that chiral amines are indeed present in the interlayer space, and that their handedness is preserved upon insertion.

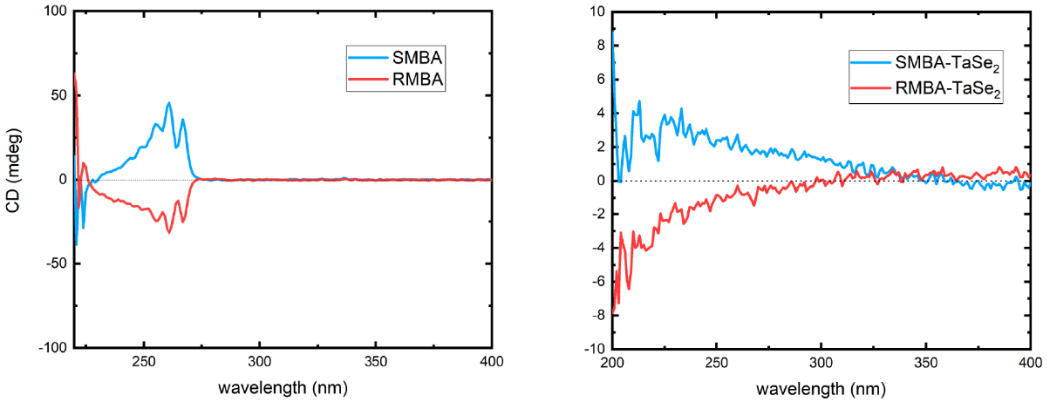

(a) (b)

Figure 4.4: Circular dichroism (CD) spectra of (a) free SMBA and RMBA molecules, and (b) their corresponding intercalated compounds with $TaSe_2$. The spectra of SMBA–$TaSe_2$ and RMBA–$TaSe_2$ retain mirror-like features, albeit with reduced intensity compared to the free molecules, indicating the successful intercalation of chiral MBA molecules.

TGA provides complementary evidence for the successful intercalation of MBA into $TaSe_2$. As shown in Figure 4.5, all samples exhibit mass loss below ~500 °C, corresponding to the release or decomposition of intercalated organic species. The en–$TaSe_2$ control sample displays a relatively uniform weight loss beginning at ~180 °C and extending to ~500 °C, which is consistent with the desorption of intercalated ethylenediamine. In contrast, both RMBA– and SMBA–intercalated samples exhibit a two-stage thermal decomposition. The first, a sharp weight loss from 180 °C to 220 °C, is possibly attributed to the combined release of ethylenediamine and loosely bound or disordered MBA molecules. The second stage, from 220 °C to 480 °C, is broader and slower, corresponding to the decomposition of more strongly intercalated MBA. This different thermal behavior compared to *en*–$TaSe_2$ strongly support the presence of MBA as a major intercalant in these samples, with ethylenediamine acting as a co-intercalant and potential facilitator. Besides, the smaller total mass loss percentage of MBA-$TaSe_2$ than *en*–$TaSe_2$ is consistent with the lower intercalation efficiency of MBA. This observation aligns with the structural and kinetic considerations discussed earlier, including the larger steric footprint and reduced flexibility of MBA molecules, both of which hinder their insertion into the van der Waals gaps of $TaSe_2$. The smaller total organic content, as reflected in the TGA results, thus reinforces the conclusion that MBA intercalation is more challenging and less complete than that of ethylenediamine.

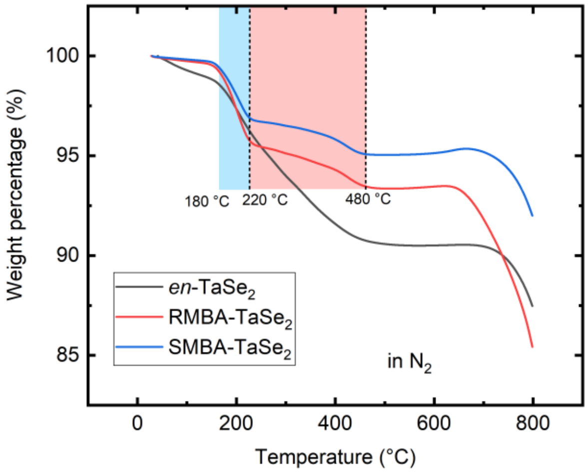

Figure 4.5: Thermogravimetric analysis of *en*–$TaSe_2$, RMBA–$TaSe_2$, and SMBA–$TaSe_2$ under $N_2$ atmosphere. All samples show mass loss below 480 °C due to the release or decomposition of intercalated organic molecules. The en–$TaSe_2$ sample exhibits a gradual weight loss starting near 180 °C, consistent with the slow release of ethylenediamine. In contrast, the RMBA– and SMBA–intercalated samples show a sharper weight loss in the 180–220 °C range (blue shaded region), attributed to the combined release of ethylenediamine and early-stage desorption or decomposition of loosely bound MBA molecules. A second, broader weight loss from 220 °C to 480 °C (red shaded region) is primarily associated with the thermal decomposition of strongly intercalated MBA. The distinct thermal profiles further support the successful intercalation of MBA into $TaSe_2$.

Based on the observed mass loss of approximately 8.0% between 180 °C and 500 °C in the TGA profile of en–$TaSe_2$, and assuming this loss corresponds exclusively to the release of intercalated ethylenediamine (en), we estimate the en : $TaSe_2$ molar ratio to be approximately 0.49. This suggests that nearly one ethylenediamine molecule is intercalated for every two $TaSe_2$ units, indicating a substantial intercalation level consistent with significant expansion of the interlayer spacing.

### 4.3.2 Superconductivity.

Magnetic susceptibility measurements on en–$TaSe_2$ reveal a clear superconducting transition near 5.2 K, as shown in Figure 4.6a. Under zero-field-cooled (ZFC) conditions, $\chi$-T curves exhibits a sharp diamagnetic drop, while field-cooled (FC) data show a similar but less pronounced downturn, consistent with the behavior of a type-II superconductor. The divergence between ZFC and FC curves and the emergence of negative susceptibility confirm the onset of a bulk Meissner state. These results demonstrate that ethylenediamine intercalation induces superconductivity in $TaSe_2$ under mild solvothermal conditions. The RMBA–intercalated $TaSe_2$ sample exhibits a clear superconducting transition at approximately 7 K, as shown in Figure 4.6b. The ZFC curve displays a sharp diamagnetic drop with a susceptibility amplitude significantly larger than that of en–$TaSe_2$, suggesting an enhanced superconducting volume fraction. The separation between ZFC and FC curves and the negative $\chi$ values are consistent with the development of a Meissner state. Compared to the ~5.2 K transition observed in en–$TaSe_2$, the higher Tc in RMBA–$TaSe_2$ points to a potential role of chiral intercalants in modifying the superconducting properties of layered materials.

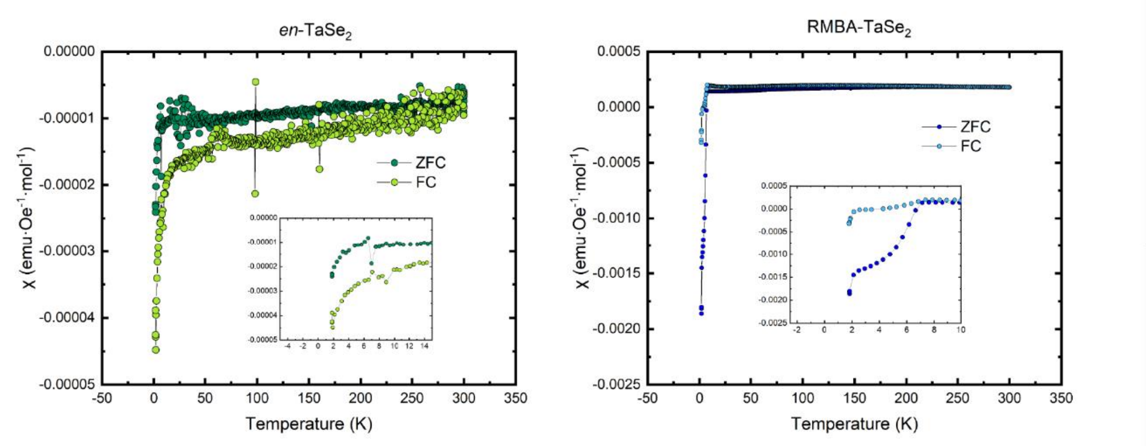

(a) (b)

Figure 4.6: Temperature-dependent magnetic susceptibility of (a) en–$TaSe_2$ and (b) RMBA–$TaSe_2$ measured under zero-field-cooled (ZFC) and field-cooled (FC) conditions with an applied field of 100 Oe.

Magnetic susceptibility measurements reveal notable differences in the superconducting behavior between en–$TaSe_2$ and RMBA–$TaSe_2$. As shown in Figures 4.6, both samples exhibit clear diamagnetic transitions, indicating the onset of superconductivity. However, the transition temperature (Tc) of RMBA–$TaSe_2$ is significantly higher, occurring near 7 K, compared to ~5.2 K for en–$TaSe_2$. Moreover, the ZFC susceptibility of RMBA–$TaSe_2$ reaches a value of approximately $-2.3 \times 10^{-3}$ emu·Oe$^{-1}$·mol$^{-1}$, nearly an order of magnitude larger than that of en–$TaSe_2$ ($-4.5 \times 10^{-4}$ emu·Oe$^{-1}$·mol$^{-1}$). This enhanced diamagnetic response suggests a larger superconducting volume fraction in RMBA–$TaSe_2$, possibly due to improved interlayer coupling or better structural coherence induced by the bulky, rigid chiral intercalant. The sharper transition and stronger shielding further support the idea that chiral molecules such as MBA not only insert successfully into the $TaSe_2$ host lattice, but may also tune the superconducting properties, offering a new handle for manipulating quantum behavior in layered materials. These observations collectively demonstrate that molecular intercalation not only induces superconductivity in otherwise weakly or non-superconducting $TaSe_2$, but that the choice of intercalant—particularly bulky and chiral amines like RMBA—can significantly enhance $T_c$ and improve superconducting volume fraction.

To further probe the superconducting behavior of RMBA–$TaSe_2$, we measured temperature-dependent resistivity (R–T) at three different sample positions. As shown in Figure 4.7, all three measurement channels exhibit a consistent and reproducible drop in resistance beginning near 2.5 K, suggesting the onset of a superconducting transition. However, none of the channels reach zero resistance, and the transitions appear broad and incomplete. This behavior is indicative of filamentary or low-dimensional superconductivity, which may arise from sparse percolating superconducting domains or anisotropic transport pathways.

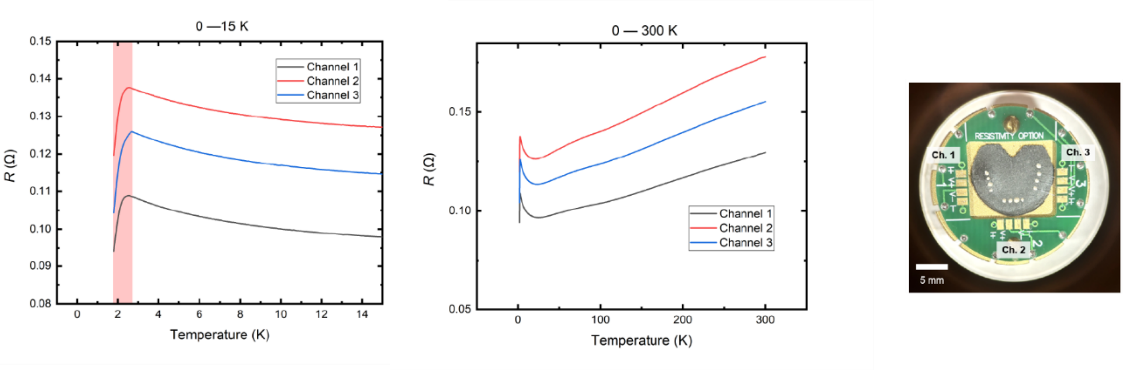

(a)

(b)

(c)

Figure 4.7: (a) Low-temperature resistance (R–T) curves of RMBA–$TaSe_2$ measured at three independent locations (Channels 1–3) from 0 to 15 K. (b) Full-range R–T curves from 0 to 300 K, showing metallic behavior with a shallow minimum near 20 K followed by a monotonic increase with temperature, typical of weakly localized transport in disordered or polycrystalline systems. (c) Optical image of the resistivity puck with RMBA–$TaSe_2$ pressed pellet and electrical contacts labeled for Channels 1, 2, and 3.

Interestingly, despite the clear magnetic transition observed near 7 K in susceptibility measurements, no distinct feature is resolved at this temperature in the R–T curves. This discrepancy may be attributed to the limited volume fraction of the 7 K superconducting phase, which, while sufficient to yield a diamagnetic response, may be insufficient to support coherent percolative transport across the sample. Additionally, the sample used for transport was a pressed polycrystalline pellet, in contrast to the likely layered anisotropy of the underlying crystal structure. Such grain boundaries and random orientations can severely suppress long-range superconducting pathways, particularly in van der Waals materials with strong in-plane transport anisotropy.

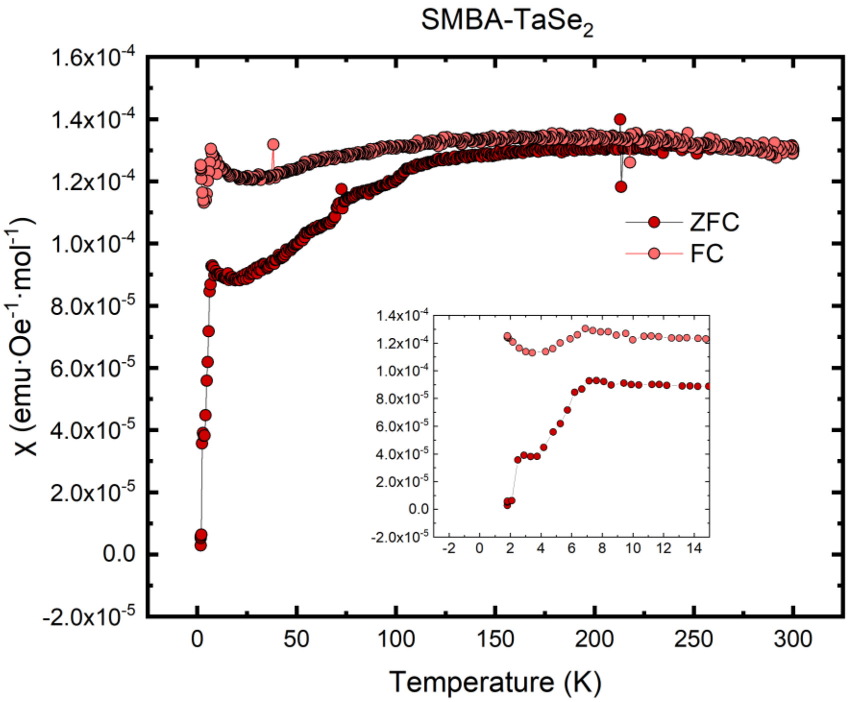

Figure 4.8: Magnetic susceptibility (χ) of SMBA–intercalated $TaSe_2$ (SMBA–$TaSe_2$) measured under zero-field-cooled (ZFC) and field-cooled (FC) conditions. A slight downturn in the ZFC curve is observed near 5 K (inset), reminiscent of a superconducting-like response, but the signal magnitude is more than an order of magnitude weaker than in superconducting samples. No clear diamagnetic transition is present, suggesting the absence of bulk superconductivity.

Unfortunately, the magnetic susceptibility measurements do not show superconductivity in the SMBA intercalated $TaSe_2$. Interestingly, SMBA–$TaSe_2$ exhibited a weak downturn in χ below ~5 K, superficially reminiscent of a superconducting transition. However, the magnitude of the diamagnetic signal is more than an order of magnitude smaller than that observed in RMBA– or en–intercalated samples, and no zero-resistance state was detected. One possible explanation lies in the synthesis history of the host $TaSe_2$. The batch used for SMBA intercalation had undergone full annealing and re-heating steps, which may have restored its ideal layered structure and reduced defect density. Also, racemic MBA- $TaSe_2$ and reproduced RMBA-TaSe2 synthesized with the same batch of $TaSe_2$ does not exhibit superconductivity. In contrast, earlier superconducting samples were intercalated into unannealed or only partially annealed $TaSe_2$, which may retain metastable stacking faults, local strain, or interstitial sites favorable for molecular intercalation and percolative superconductivity. These results suggest that the crystallographic “preparedness” of the host lattice plays a crucial role in enabling bulk superconductivity via molecular intercalation.

## 4.4 Conclusion

In this chapter, we demonstrated that the intercalation of ethylenediamine and α-methylbenzylamine (MBA), including its chiral enantiomers, into the layered host 2H–$TaSe_2$ can induce superconductivity, with the intercalant structure significantly influencing the transition temperature and magnetic response. Ethylenediamine, due to its small size and high polarity, readily intercalates under mild solvothermal conditions and yields superconducting en–$TaSe_2$ with a Tc of ~5.2 K. In contrast, the intercalation of MBA proved more challenging, likely due to its bulkier structure and reduced hydrogen bonding capability. Interestingly, trace amounts of ethylenediamine were found to promote the intercalation of MBA, suggesting a co-intercalation mechanism that lowers the barrier for incorporating larger, less flexible amines.

Circular dichroism and thermogravimetric analysis confirmed the presence and thermal stability of intercalated chiral MBA molecules, while magnetic susceptibility measurements revealed a significantly enhanced superconducting transition temperature of ~7 K in RMBA–$TaSe_2$. The diamagnetic response of RMBA–$TaSe_2$ is markedly stronger than that of en–$TaSe_2$, suggesting a larger superconducting volume fraction or improved structural coherence associated with the chiral intercalant. However, resistivity measurements of pressed polycrystalline pellets revealed only partial resistance drops near 2.5 K, consistent with filamentary superconductivity and indicating that the higher-Tc phase may have limited connectivity or volume fraction.

These findings collectively highlight that molecular intercalation not only enables the induction of superconductivity in non-superconducting or weakly superconducting hosts like $TaSe_2$, but also provides a tunable route for manipulating superconducting properties through control of molecular geometry, polarity, and chirality.

# Chapter 5: In-situ synchro X-ray study on hydrothermal and solvothermal TMC intercalations.

## 5.1 Introduction

Layered-structured transition metal chalcogenides have displayed many interesting physical properties including superconductivity, metallic conductivity, and magnetic properties, due to their structural diversity. These materials are perfect candidate for chemical tuning to change their properties because the layered structure bound through van der Waals forces could be intercalated by a variety of guest chemicals. FeSe, for example, is superconducting itself with a transition temperature of 8 K, which could be raised to 43 K through liquid ammonia reactions to form phases $A_x(NH_3)_x(NH_2)_y$FeSe. Molten slat flux is nowadays a common practice for the synthesis of many quantum materials including transition metal chalcogenides. However, many intercalated species are not stable at such a high temperature which melts the salts and then decomposes. For the intercalation of these chemicals, hydrothermal and solvothermal methods are a milder alternative which is usually conducted is a relatively lower temperature.

Hydrothermal and solvothermal syntheses have become indispensable methods in modern materials chemistry for the preparation of complex crystalline solids. These methods, which rely on conducting reactions in sealed vessels under elevated temperature and autogenous pressure, offer access to metastable phases, unique morphologies, and intercalated structures that are often inaccessible by conventional high-temperature solid-state methods. While hydrothermal synthesis uses water as the reaction medium, solvothermal synthesis broadens the scope by employing organic solvents such as amines, alcohols, or mixed systems. These solvents not only alter dielectric properties and solubility but can also serve as structure-directing agents or intercalants. Their ability to dissolve precursors and stabilize intermediate states provides critical control over nucleation, growth, crystallinity, and ultimately the functional properties of the materials formed [198,199].

Nevertheless, these synthesis methods are often referred to as "black box" reactions, as the reactions occur in opaque and inert autoclaves, and thus the actual sequence of phase transformations, intermediate states, and crystallization dynamics remain largely hidden. This lack of mechanistic insight significantly hampers our ability to rationally design reaction conditions or target metastable phases with desirable properties. Recent developments in in-situ synchrotron-based X-ray diffraction techniques, particularly energy-dispersive XRD (EDXRD) and angular-dispersive XRD (ADXRD), have transformed this landscape, enabling real-time observation of phase evolution, crystallization kinetics, and metastable intermediates during solvothermal or hydrothermal processes [202–205].

Among the most prominent studies, Clarke et al. investigated the intercalation of liquid ammonia and alkali metals into FeSe using time-resolved in-situ XRD, revealing hidden ammonia-rich intermediates and their reversible transformation into superconducting $ThCr_2Si_2$-type frameworks [206]. This approach has provided a clearer understanding of the reaction pathways and structural flexibility of intercalated FeSe compounds under cryogenic and ambient temperatures. Kanatzidis and co-workers introduced the concept of “panoramic synthesis”, applying in-situ synchrotron PXRD to track the complete evolution of solid-state reactions in the Cs/Sn/P/Se system. Remarkably, six new crystalline phases were discovered within a single reaction composition—highlighting how many transient, possibly functional, phases are missed in conventional ex-situ work. This study emphasizes that in-situ diffraction provides not only structural snapshots but continuous temporal fingerprints of material evolution [207]. Similarly, Bensch et al. conducted in-situ EDXRD studies on manganese thioantimonates and demonstrated how subtle changes in temperature shift the nucleation pathway, causing transitions from first-order to diffusion-controlled crystallization mechanisms. Their work confirmed the presence of crystalline intermediates that vanish in ex-situ sampling and underscored the need for kinetic modeling to describe multistage reactions [208]. In the realm of porous and layered materials, O'Hare's group has provided some of the most comprehensive in-situ studies on hydrothermal gallophosphates (e.g., ULM-5) [209], tin sulfides [210], and layered perovskites [211]. Their findings revealed competing reaction pathways dictated by pH, phosphorus source, and solvent identity—sometimes leading to two distinct intermediate phases, which then either undergo solid–solid transformations or partial dissolution-recrystallization. These transformations could not be resolved without time-resolved XRD or complementary in-situ spectroscopies. Building upon these developments, we aim to explore the in-situ crystallization behavior of intercalated transition metal chalcogenides (TMCs) synthesized via hydrothermal and solvothermal methods. Our prior work using Teflon-lined stainless-steel autoclaves successfully produced a range of Fe- and Co-based layered chalcogenides. However, the inability to monitor reaction intermediates hindered our understanding of how structural complexity, redox environment, or precursor solubility dictate final product formation. To address this, we replaced the reaction vessel with quartz capillaries and transferred our synthetic workflow to the 17-BM-B beamline at the Advanced Photon Source (APS). By precisely reproducing temperature-pressure conditions and continuously monitoring diffraction patterns, we tracked crystallization behavior with both time and spatial resolution.

In this chapter, we present eight solvothermal and hydrothermal reactions (See Figure5.1), categorized by transition metal species (Fe or Co), synthetic complexity (bottom-up vs. top-down), and solvent ($H_2O$, ethylenediamine, or 1,2-diaminopropane). We identify and analyze reaction intermediates, determine induction times, and infer kinetic models through peak evolution and phase transformations. Ultimately, our goal is to unravel the mechanistic underpinnings of solvothermal crystallization in layered materials and to provide a basis for rational design of metastable intercalates with desired electronic properties.

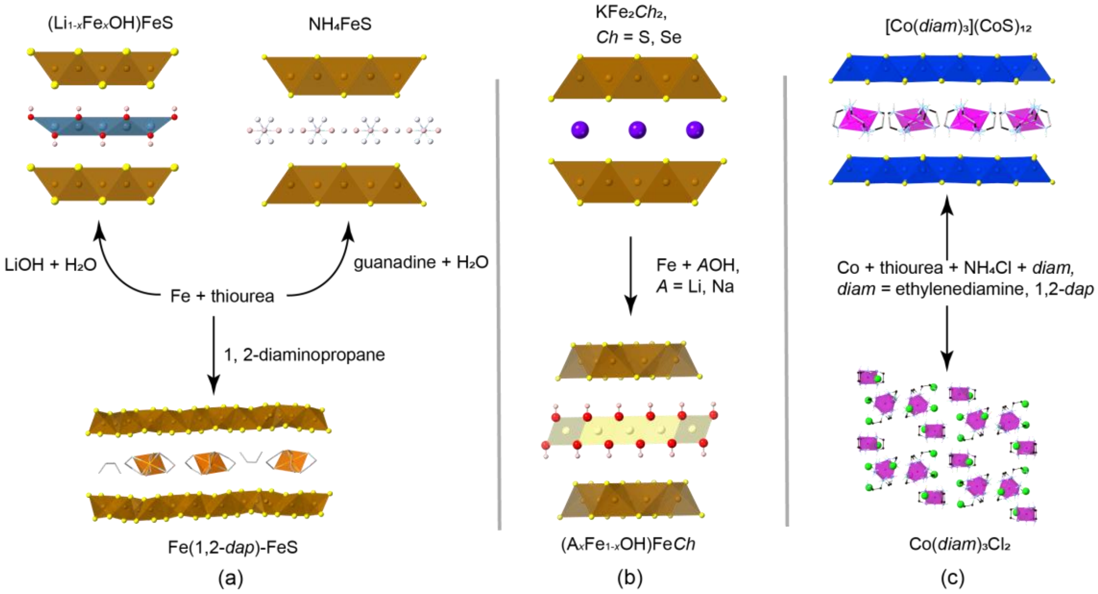

Figure 5.1: (a) Bottom-up hydrothermal/solvothermal synthesis with iron (b) Top-down hydrothermal synthesis with iron and $KFe_2Ch_2$ ($Ch$ = S, Se) (c) Bottom-up solvothermal synthesis with cobalt.

## 5.2 Experiments

### 5.2.1 In-situ experiments

The *in-situ* studies were carried out on 17-BM-B beamline at the Advanced Photon Source (APS) at Argonne National Laboratory. The incident X-ray beam was collected by a PerkinElmer a-Si C-window detector at a distance of 500 mm. A quartz capillary of 5 cm height and 3 mm in diameter was chosen as the replacement of the Teflon cup in each reaction. All the samples were loaded either in an ambient environment or in an argon-filled glovebox, consistently in the same condition as the home experiments. Respectively, all the starting materials are the same in each reaction and the amount of the samples were all cut to 1/30 compared with the home laboratory preparations. The solvent in each reaction was injected into the capillary through a syringe with a Kapton needle. The capillary filled with sample and solvent was then sealed by parafilm and transferred to the beamline, where the capillary was later fixed at a 2-axis robotic arm for program-controlled adjustment of the vertical and horizontal position across the beamline. An ~ 7 to 25 atm pressure of $N_2$ gas was applied to the capillary to simulate the sealed condition in hydrothermal and solvothermal syntheses and was. The temperature was increased rapidly at ~10 K/min by a heat gun under the capillary to reach the same point of each reaction in the home laboratory. The reaction duration for each synthesis was from ~800 min to ~2600 min, depending on the shifts of the beamline time offered by APS in each proposal. The wavelength of the synchrotron X-ray in $NH_4FeS$ and the three solvothermal syntheses was 0.24147 Å and 0.24101Å, respectively. The position of the capillary was adjusted to the point that the incident beam could pass through the interlayer between the solvent and the solid layers, where the reaction would occur. During the measurement, the capillary was translated vertically with respect to the synchrotron beam for 0.3 mm up and down twice by the robotic arm for every averaged PXRD pattern collection cycle in order to obtain the data of the entire solvent-solid interlayer, considering that the layers were not ideally flat. The raw images were first presented in GSAS-II and then exported as xye files for Rietveld and sequential refinements through DIFFRAC.TOPAS. The crystal information files required in the refinements were obtained either from the ICSD database or from the analysis of the single crystal XRD in our home laboratory experiments.

### 5.2.2 Bottom-up hydrothermal/solvothermal synthesis with Fe

*Home laboratory experiments*

$(Li_{1-x}Fe_xOH)FeS$. For a typical preparation of the compound, 10 mmol of Fe powder (Alfa Aesar, 99.5%), 12mmol of the thiourea (Sigma-Aldrich, 99.0%) and 100 mmol of LiOH powder (Sigma-Aldrich, 99.0%) were suspended in 20 mL of distilled water in a 47-ml Teflon cup. The Teflon cup was then sealed under ambient environment within a stainless-steel autoclave and heated at 120 °C for 3-5 days. After cooling down to room temperature, the autoclave was opened and shiny black precipitate was found and washed with $H_2O$ through centrifuge. The product was then collected, vacuum dried, and stored in a nitrogen-filled glovebox for further characterization.

$NH_4FeS$. To prepare the compound, 10 mmol of Fe powder (Alfa Aesar, 99.5%), 12 mmol of the thiourea (Sigma-Aldrich, 99.0%) and 25-50 mmol of free guanidine base (Sigma-Aldrich, 99.0%) were mixed in a 47-mL Teflon cup filled with 20 mL of water and then sealed in an autoclave in ambient environment. The Teflon cup was then sealed in a stainless-steel autoclave and heated at 125 °C for 3-4 days. After cooling down to room temperature, the content in the autoclave was washed and centrifuged ~ 4 to 5 times until the supernatant was clear.

1,2-*dap*-FeS. For the preparation of the compound, 10 mmol of Fe powder (Alfa Aesar, 99.5%), 10 mmol of the thiourea (Sigma-Aldrich, 99.0%) and 3.8 mmol $NH_4Cl$ (Fisher, 99.5%) were mixed in a 47-mL Teflon cup filled with 20 mL of 1,2-*dap* (Sigma-Aldrich, 99.0%) and then sealed in an autoclave. The loading of the autoclave was also performed entirely in an $N_2$-filled glovebox and then heated to 200 °C in a furnace and kept there for 3 to 5 days. After the solvothermal reaction was complete, we cooled the autoclave to room temperature and recovered the contents in the glovebox. The supernatant above the product appeared a green color. We poured the

### 5.2.3 Bottom-up solvothermal synthesis with Co

*Home laboratory experiments*

$[Co(\mathit{en})_3](CoS)_{12}\cdot\mathit{en}$. To prepare the compound, 10 mmol of Co powder (Alfa Aesar, 99.5%), 10 mmol of the thiourea (Sigma-Aldrich, 99.0%) and 3.8 mmol $NH_4Cl$ (Fisher, 99.5%) were combined in a 47-mL Teflon cup filled with 20 mL of ethylenediamine (Sigma-Aldrich, 99.0%). The $NH_4Cl$ serves as the mineralizer. We then sealed the Teflon cup within a stainless steel autoclave. The loading of samples and the sealing of the autoclave was performed entirely in an $N_2$-filled glovebox. The autoclave was then heated to 140°C in a furnace and kept there for 3 to 5 days. We then recovered the contents in the glovebox after the reaction was complete and the autoclave was cooled down to room temperature. We poured the solid product along with the supernatant which appeared to be either brown or orange into a funnel lined with filter paper. The filtered product was washed with ethylenediamine (*en*) several times and left to dry in the glovebox. We found the filtered mixture to contain a black powder, irregular black crystals, and yellow crystals. The black crystals correspond to $[Co(\mathit{en})_3](CoS)_{12}\cdot\mathit{en}$, and the yellow crystals to a side product, $Co(\mathit{en})_3Cl_2$.

1,2-*dap*-CoS. Similar preparation as described above by combining 10 mmol of Co powder (Alfa Aesar, 99.5%), 10 mmol of the thiourea (Sigma-Aldrich, 99.0%) and 3.8 mmol $NH_4Cl$ (Fisher, 99.5%) in a 47-mL Teflon cup filled with 20 mL of 1,2-diaminopropane (1,2-*dap*, Sigma-Aldrich, 99.0%). The Teflon cup was likewise sealed within a stainless steel autoclave which was then heated to 140°C and kept there for 3 to 5 days. After the solvothermal reaction was complete, we cooled the autoclave to room temperature and recovered the contents in the glovebox. The supernatant above the product appeared to be an orange color. We poured the solid product along with the supernatant into a funnel lined with filter paper. We then washed the product with 1,2-*dap* several times and left it to dry in the glovebox. We found the filtered mixture to contain a black and light orange powders. The black powders correspond to 1,2-*dap*-CoS, and the light orange crystals to a side product, Co(1,2-*dap*)$_3$Cl$_2$. We could not get the exact crystal structure of the 1,2-*dap*-CoS yet due to the poor crystallinity. The powder X-ray diffraction shows a similar pattern with the one of [Co(*en*)$_3$](CoS)$_{12}$·*en*, and therefore we assume that 1,2-*dap*-CoS would have a similar layered structure with [Co(*en*)$_3$](CoS)$_{12}$·*en.*

## 5.3 Results and discussion

### 5.3.1 Bottom-up intercalation of (Li$_{1-x}$Fe$_x$OH)FeS

We chose the Fe/thiourea reaction system for our first exploration because the FeS appears to exhibit richer chemistry in intercalation chemistry than that in FeSe or the cobalt system. As Figure 5.1 shows, not only could Fe/thiourea system reacts either hydrothermally or solvothermally from the basic element sources, but intercalated FeS could also exchange its intercalation layers with other compounds under a hydrothermal condition. Cobalt would only stay metal or form cobalt oxide with water despite with the existence of the chalcogen sources (thiourea, selenourea), leading to a limited synthesis route for only solvothermal reactions. Many FeSe analogue could be prepared using a similar route for the intercalated FeS. Although the physical properties of FeSe family are more appealing since FeSe has been wildly reported as a superconductor, FeS species presents higher stability in concentrated bases and could usually be grown into more crystalline products, which are more helpful for both structural and physical analysis. Zhou et. al. also found that c and (Na$_{1-x}$Fe$_x$OH)FeS could be made superconducting as well through resistivity and magnetization measurements. Larger $x$ which indicates higher electron doping, favors higher $T_c$ to the maximum of 8 K in the FeS system, and the ratio change of the Fe occupied in the LiOH intercalation layers were shown through the *in-situ* X-ray diffraction, which gives us a more clear picture how long the hydrothermal reaction should last to synthesize the product which we desire as superconductor.

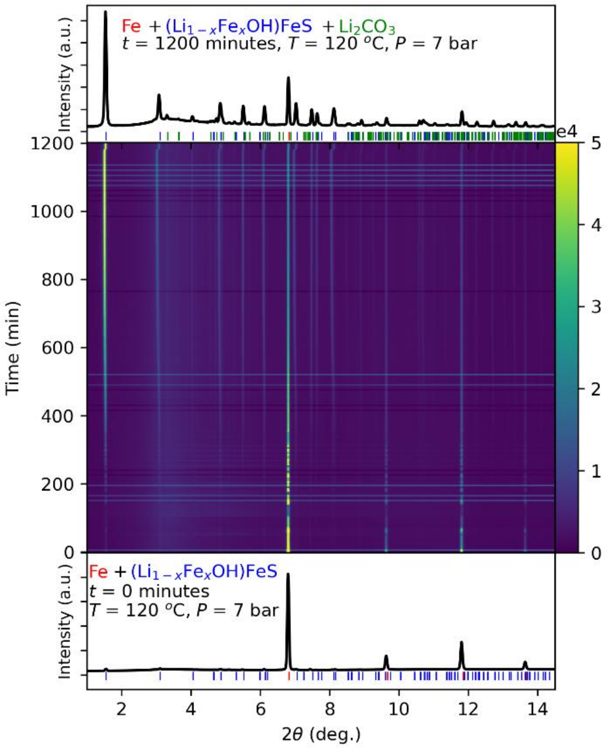

Figure 5.2: In-situ synchrotron powder X-ray diffraction contour plot of the hydrothermal reaction between Fe and thiourea in the presence of LiOH at 120 °C and 7 bar. Over the 1200-minute duration, the reaction proceeds to form (Li$_{1-x}$Fe$_x$OH)FeS as the main layered product, alongside $Li_2CO_3$ as a crystalline byproduct. The diffraction peaks of the product phase appear early and grow steadily in intensity, indicating continuous formation. The well-developed peaks at the final timepoint reflect high crystallinity of the intercalated product. No sharp phase transition or intermediate phase is observed, suggesting a smooth and direct pathway from precursors to the final structure.

In Figure 5.2, we could see the formation of both (LiOH)FeS and $Li_2CO_3$. The $Li_2CO_3$ impurities could come from the reaction between $Li^+$ and $CO_2$ under basic conditions. $CO_2$ were mainly from the decomposition of thiourea at high temperature, which would decomposed to ammonium, $HS^-$ as well as $CO_2$. The consumption of Fe powders and the formation of (LiOH)FeS were relatively slow at the initial point. A reasonable explanation of this is that the oxidation of Fe metal to $Fe^{2+}$ with $H_2O$ is a rate-limited process, considering that the metal was reacted in a highly basic environment. Another possible reason is that the precipitation of $Li_2CO_3$ also consumed a part of the $Li^+$ and slowed down the rate of the (LiOH)FeS formation. The weight percentage of Fe and (LiOH)FeS changed steadily from around the 200th min to around the 600th min when $Li_2CO_3$ reached a limit. Then the reaction rates of Fe and (LiOH)FeS slowed down because the concentration of the reactants had been nearly consumed. The c-axis of LiOHFeS unit cell increased obviously during the reaction. When $Fe^{2+}$, LiOH and $HS^-$ (which was from the decomposition of thiourea at high temperature) combined together to form layer structure materials, $Fe^{2+}$ would not entirely reacted with $HS^-$ to form the FeS layers. Some of the $Fe^{2+}$ would occupy the position of the LiOH in the layered structure and form ($Li_{1-x}Fe_xOH$)FeS. That is, the superconductor ($Li_{1-x}Fe_xOH$)FeS is actually the intermediate phase in the hydrothermal reaction. The doping phase was a metastable phase and $Fe^{2+}$ slowly decreased during the reaction and were replaced by the new $Li^+$ and $OH^-$ to form a more stable structure. LiOH is overall larger than the $Fe^{2+}$ cation, which resulted in the raise of c-axis in the LiOHFeS unit cell. The Fe occupancy rate in LiOH layer with a dropping curve obtained from the sequential refinements likewise supports this point.

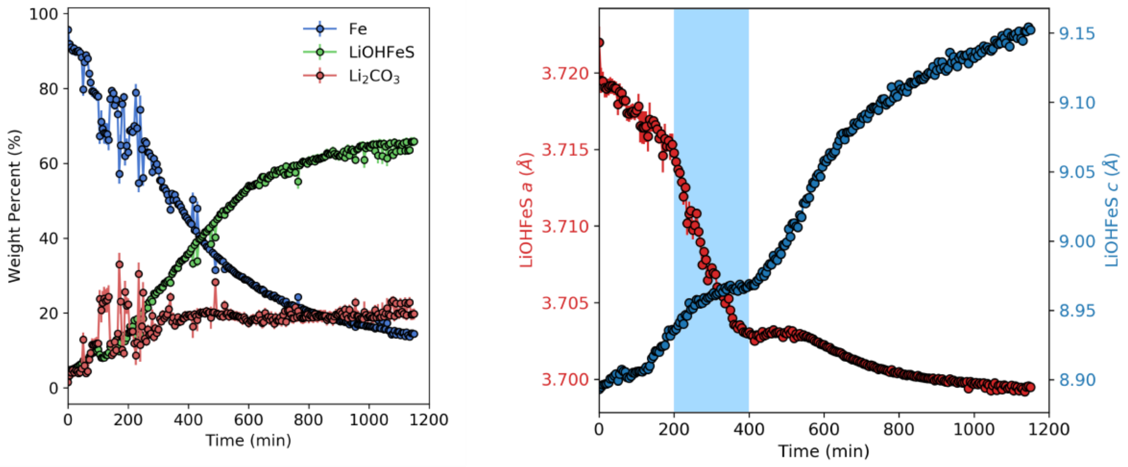

(a) (b)

Figure 5.3: Evolution of phase composition and lattice parameters during the hydrothermal reaction of Fe with thiourea and LiOH at 120 °C and 7 bar. (a) Weight percent of crystalline phases obtained via in-situ Rietveld refinement. ($Li_{1-x}Fe_xOH$)FeS forms steadily over the full reaction window, increasing to ~65 wt%, while metallic Fe is gradually consumed. $Li_2CO_3$ appears early and persists as a minor byproduct. The smooth profiles suggest a direct reaction pathway without pronounced intermediate phases. (b) Lattice parameters of ($Li_{1-x}Fe_xOH$)FeS extracted from time-resolved refinements. The a-axis shows a pronounced contraction during the 200–400 min interval (highlighted in blue),

suggesting densification or structural rearrangement within the FeS layers. Following this stage, the c-axis begins to rise steadily, reflecting progressive intercalation and layer expansion. These trends together indicate a shift from initial nucleation to framework stabilization and ordering.

We could also observe a slowdown increase from ~200 min to ~400 min on the c-axis curve in Figure 5.4a, which could be explained by separating the formation of LiOHFeS into two parts. The first part is the formation of layered structure FeS without any intercalation phases; the second part is the intercalation of both $Fe^{2+}$ and LiOH. Kinetically, $Fe^{2+}$ is relatively small and could easily go into the gap between the FeS layers, which leads to a relatively small increase of the c-axis. Although the meanwhile intercalation of LiOH is slower, the LiOHFeS phase is a much stable phase thermodynamically and the intercalated $Fe^{2+}$ was gradually replaced by LiOH.

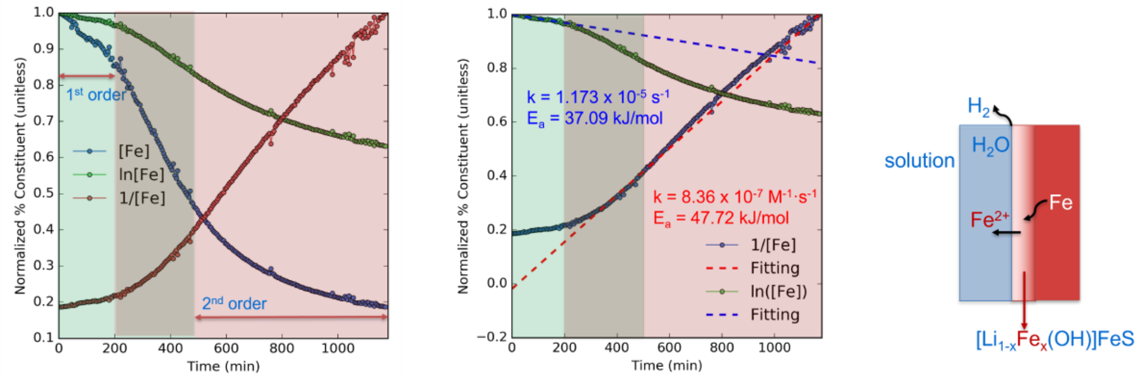

(a) (b) (c)

Figure 5.4: Kinetic analysis and proposed mechanism of Fe consumption during the hydrothermal synthesis of $(Li_{1-x}Fe_xOH)FeS$ at 120 °C and 7 bar.**(a)** Time evolution of normalized Fe content fitted using first- and second-order kinetic models. The early stage (green region, 0–200 min) shows slow consumption of Fe. Between ~200–400 min (gray region), the Fe content follows first-order kinetics, suggesting rate-limiting electron transfer or surface reaction. Beyond 400 min (pink region), the consumption trend transitions to second-order behavior, likely controlled by coupled diffusion and redox processes.**(b)** Linearized kinetic fits of ln[Fe] and 1/[Fe], used to extract apparent rate constants and activation energies (Ea). The first-order process shows a higher rate constant ($1.17 \times 10^{-5}\ s^{-1}$) and lower Ea (37.09 kJ/mol), compared to the slower second-order regime ($k = 8.36 \times 10^{-7}\ M^{-1}s^{-1}$, Ea = 47.72 kJ/mol).**(c)** Schematic model of Fe oxidation and intercalation. Metallic Fe acts as both reductant and $Fe^{2+}$ source, which diffuses into solution, re-coordinates with $OH^-/Li^+$, and inserts into the layered FeS framework to form $(Li_{1-x}Fe_xOH)FeS$. The process likely involves solid–solution interfacial redox and layer-by-layer assembly.

To further elucidate the reaction mechanism, we quantified the disappearance of metallic Fe and performed kinetic modeling (Figure 5.4b). The reaction profile can be clearly divided into two stages. Between 250–400 minutes, the reaction follows first-order kinetics, as evidenced by the linearity of ln[Fe] versus time. This suggests that Fe dissolution is rate-limiting in this early stage, likely governed by the redox displacement reaction:

$$\mathrm{Fe} + 2\mathrm{H_2O} \rightarrow \mathrm{Fe}^{2+} + 2\mathrm{OH}^{-} + \mathrm{H_2(g)} \qquad (5.1)$$

As the reaction proceeds (400–1200 min), the kinetic behavior transitions to second order, where 1/[Fe] exhibits linear dependence on time. This shift implies that the rate-limiting step moves from metal dissolution to a solution-mediated growth mechanism, involving $Fe^{2+}$ transport, intercalation, and the formation of the final layered product.

The extracted rate constants and activation energies further support this interpretation. The apparent activation energy increases from 37.1 kJ/mol in the first-order regime to 47.7 kJ/mol in the second-order regime, consistent with the growing importance of diffusion and nucleation barriers in the later stage. A schematic model (Figure5.4c) illustrates the proposed spatial progression: Fe dissolves locally at the metal–solution interface, generating $Fe^{2+}$ and $H_2$ gas. The $Fe^{2+}$ species diffuse outward and incorporate into the LiOH-containing environment to form $(Li_{1-x}Fe_xOH)FeS$ at the advancing solid–solution front.

The combination of in-situ PXRD and kinetic analysis suggests a two-step mechanism: initial surface-controlled dissolution of Fe, followed by solution-mediated growth and intercalation. The absence of detectable intermediates implies that the system evolves along a relatively simple, yet spatially resolved redox intercalation pathway.

The in-situ X-ray diffraction experiment of $(Li_{1-x}Fe_xOH)FeS$ indicates that the hydrothermal reaction would not take a long time to start and would happen once the temperature reaches the required point. A longer duration of hydrothermal synthesis would not result in the superconductor we desire for, which matches the result in the home laboratory synthesis. For a 5-day reaction compared with a 3-day reaction at the same temperature, the superconductivity decreased. If the reaction temperature was increased from 120 °C to 200 °C, which would increase the reaction rate, the product transfer from superconductor to non-superconductor as well.

### 5.3.2 $KFe_2S_2$ deintercalation with LiOH.

Figure 5.5 presents the in-situ PXRD contour map for the hydrothermal reaction of $KFe_2S_2$ with LiOH and Fe at 130 °C and 6 bar. At t = 0 min, the diffraction pattern reveals strong reflections from the starting material $KFe_2S_2$, as well as pre-existing peaks from the product phase $(Li_{1-x}Fe_xOH)FeS$. This suggests that the transformation may have already initiated during the initial heating and pressurization stages, even before the first dataset was collected. Several broad and unidentified reflections (marked with asterisks) are also observed, indicating the presence of poorly crystalline or short-lived intermediate species.

As the reaction progresses, the $KFe_2S_2$ peaks gradually decay, and the $(Li_{1-x}Fe_xOH)FeS$ peaks steadily grow in intensity, consistent with a topochemical transformation. Between 900 and 1100 minutes, a data gap is present due to an unscheduled beamline interruption at the synchrotron source. Although this break obscures the continuous tracking of the reaction, the pattern at t = 1400 min confirms that the transformation has reached near-completion, with only trace signals from $KFe_2S_2$ remaining. No reappearance of intermediate peaks was observed after data resumed, suggesting that any metastable phase formed during the gap was either fully consumed or transformed.

The evolution of several broad peaks in the early stage, which subsequently vanish, points to the formation of a transient disordered or partially deintercalated intermediate. However, these peaks could not be confidently indexed or assigned, highlighting the limitations of in-situ PXRD in resolving short-range ordering or amorphous content. Furthermore, the apparent absence of any sharp induction point or burst-like crystallization suggests a slow and continuous transformation pathway—likely involving solid-state diffusion of cations and local rearrangement of the Fe–S framework, rather than bulk dissolution–reprecipitation.

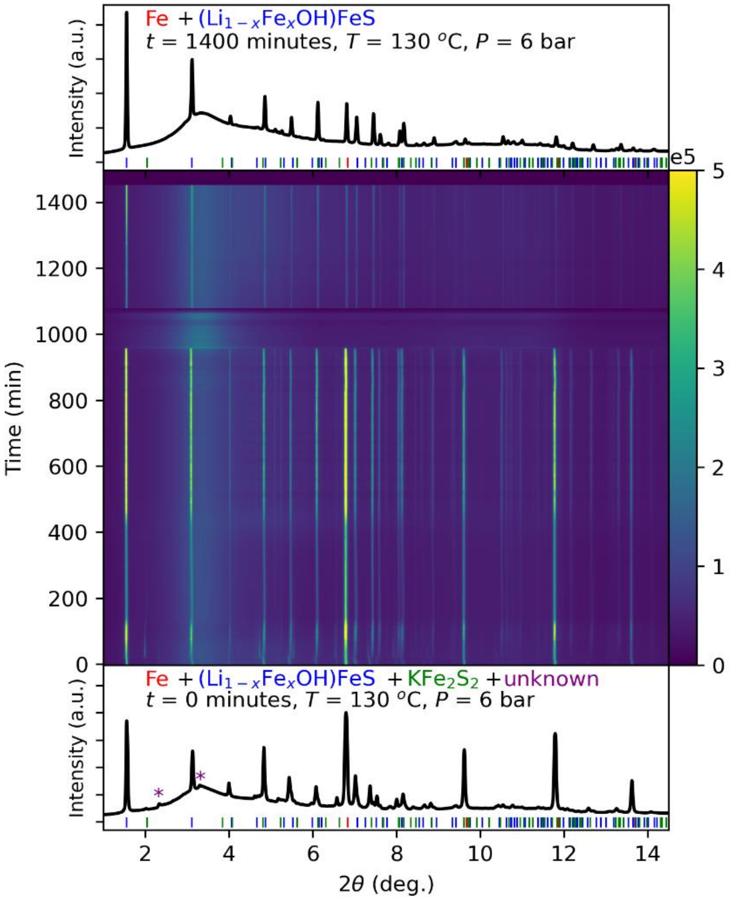

Figure 5.5: Time-resolved in-situ synchrotron powder X-ray diffraction contour plot for the hydrothermal transformation of $KFe_2S_2$ into $(Li_{1-x}Fe_xOH)FeS$ at 130 °C and 6 bar. The lower and upper panels show diffraction patterns at the beginning (t = 0 min) and end (t = 1400 min) of the experiment, respectively. Bragg reflections from $KFe_2S_2$ (green ticks) and Fe (red ticks) decrease over time, while those of the product $(Li_{1-x}Fe_xOH)FeS$ (blue ticks) grow steadily, indicating a topochemical transformation pathway. Several transient and unidentified peaks (asterisks) appear in the early stage and vanish later, likely corresponding to short-lived intermediate phases. Note: The gap between 900 and 1100 minutes reflects a temporary synchrotron outage during which no data were collected.

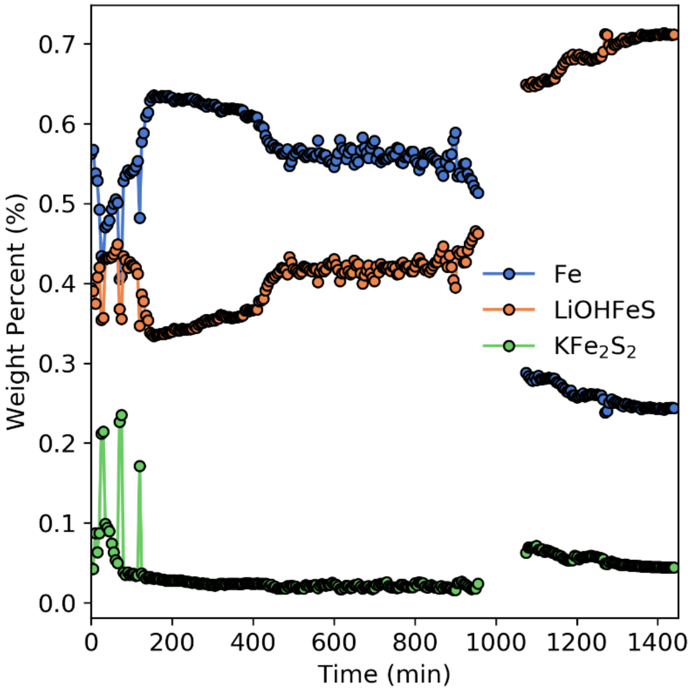

Figure 5.6: Evolution of the weight percentages of Fe (blue), $(Li_{1-x}Fe_xOH)FeS$ (orange), and $KFe_2S_2$ (green) during the hydrothermal transformation at 130 °C and 6 bar, obtained by sequential Rietveld refinement of in-situ PXRD data. $KFe_2S_2$ is rapidly consumed within the first 150 minutes, while the product phase grows steadily throughout the reaction. Fe remains largely unchanged during the intermediate stage but decreases sharply near the end, consistent with accelerated product formation. It should be noted that a small apparent resurgence of $KFe_2S_2$ after the 900–1100 min data gap is attributed to refinement artifacts in a low-signal regime and is not supported by the raw diffraction patterns.

The quantitative phase evolution extracted from Rietveld refinement is shown in Figure 5.7, where the weight percentages of $KFe_2S_2$, Fe, and $(Li_{1-x}Fe_xOH)FeS$ are tracked over the course of the hydrothermal reaction. $KFe_2S_2$ is consumed rapidly within the first 150 minutes, consistent with early deintercalation or structural collapse. Surprisingly, $(Li_{1-x}Fe_xOH)FeS$ is already present at $t = 0$ and increases slightly during this period, while Fe temporarily increases, suggesting some degree of early Fe accumulation or partial oxidation prior to sustained conversion. Between 200 and 900 minutes, all three phases remain relatively constant, indicating a kinetic bottleneck—possibly related to interfacial diffusion or local saturation effects. After a data gap between 900–1100 minutes due to synchrotron shutdown, a marked increase in the product phase and corresponding decline in Fe content are observed, confirming that the bulk of crystallization occurs during this unmonitored period. This delayed but decisive transition reinforces the presence of a long induction period followed by a rapid structural reorganization, characteristic of topochemical transformations in layered systems. It is worth noting that a slight apparent increase in the fitted weight fraction of $KFe_2S_2$ was observed after the data gap (t > 1100 min). Given the irreversible nature of the deintercalation and the absence of corresponding Bragg reflections in the PXRD contour plot, this anomaly is most likely an artifact of the Rietveld fitting process, possibly due to residual peak overlap or overfitting in a low-signal region. The actual disappearance of $KFe_2S_2$ is expected to have occurred prior to this stage.

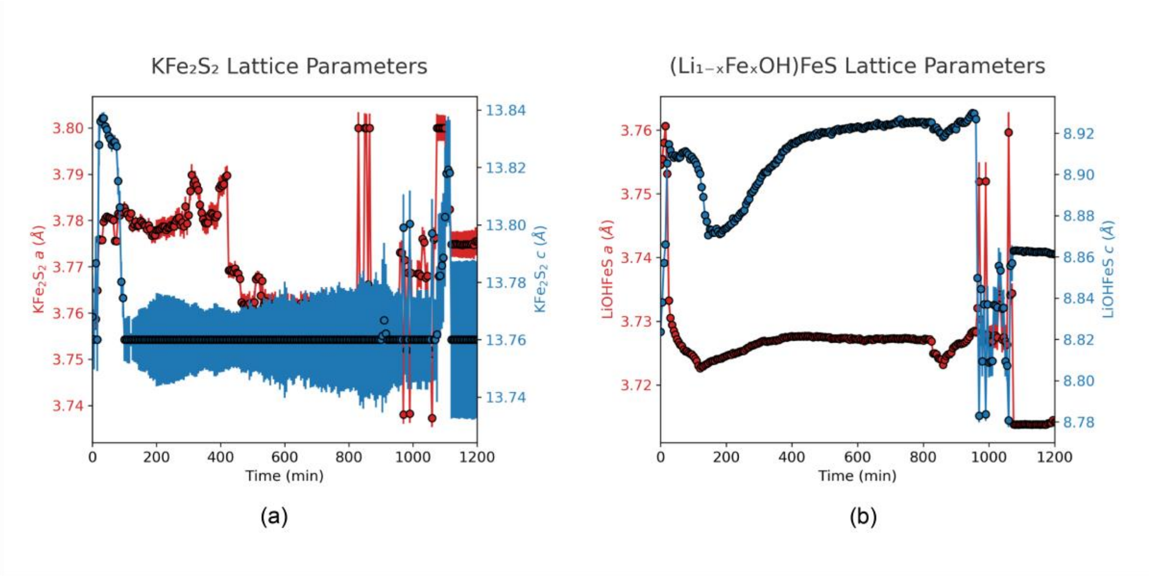

(a)

(b)

Figure 5.7: Time-dependent evolution of the lattice parameters of (a) $KFe_2S_2$ and (b) $(Li_{1-x}Fe_xOH)FeS$ during hydrothermal transformation at 130 °C and 6 bar.

The lattice parameters of $KFe_2S_2$ and $(Li_{1-x}Fe_xOH)FeS$, extracted by sequential Rietveld refinement, are shown in Figure 5.7. Upon heating, $KFe_2S_2$ exhibits a rapid contraction in both a and c axes during the first 150 minutes, consistent with topochemical $K^+$ deintercalation and structural collapse. This is followed by a moderately fluctuating regime, suggesting lattice strain or partial reorganization, before the material is fully consumed. In contrast, the product phase $(Li_{1-x}Fe_xOH)FeS$ shows an initial increase in c-axis length up to ~8.91 Å, indicating progressive intercalation of $Fe^{2+}$ and $OH^-$ layers. The a-axis remains relatively constant, supporting a two-dimensional layered growth. Lattice fluctuations in the later stage (>1000 min) are likely artifacts due to peak overlap or low phase fraction in the refinement, but overall, the results confirm a solid-state transformation route involving layer displacement and chemical substitution rather than dissolution–reprecipitation.

This experiment exemplifies both the strengths and practical challenges of time-resolved in-situ hydrothermal studies. While we were able to capture the major phase transitions and identify the final product formation, the presence of partially formed product at t = 0 and the loss of data during the most dynamic growth period limit a more quantitative kinetic treatment. Nevertheless, the data support a gradual, multi-step top-down conversion mechanism, punctuated by metastable phases and complicated by experimental uncertainties—typical of complex chalcogenide intercalation chemistry under hydrothermal conditions.

### 5.3.3 $KFe_2S_2$ deintercalation with NaOH.

We further investigated the hydrothermal transformation of $KFe_2S_2$ in NaOH under conditions of 130 °C and 4 bar, aiming to explore how alkali metal identity influences the top-down conversion pathway. The in-situ PXRD contour plot (Figure 5.8) reveals a rapid structural response upon heating. At the initial time point (t = 0), reflections from both the precursor $KFe_2S_2$ and product phases—namely $(Na_{1-x}Fe_xOH)FeS$ and FeS—were already present, suggesting that the reaction had initiated during the pre-heating or ramping period. Several unidentified peaks (marked with asterisks) were also observed and remained nearly constant throughout the experiment, potentially corresponding to stable side products or disordered intermediates.

The early reaction stage (0–100 minutes) is characterized by a sharp decrease in $KFe_2S_2$ peak intensity and a concurrent rapid emergence of the NaOHFeS product phase, as well as minor amounts of FeS. However, unlike the more continuous growth behavior observed in the LiOH-based system, the PXRD intensities of both product phases in the NaOH system plateaued quickly and showed minimal further evolution over the remaining reaction time. This trend is corroborated by quantitative Rietveld refinement (Figure 5.9), which shows that $(Na_{1-x}Fe_xOH)FeS$ reaches ~80% weight fraction within the first hour, while $KFe_2S_2$ levels off at ~20% and persists throughout the experiment. FeS remains a minor component (~8%), consistent with a parallel decomposition pathway.

The rapid onset and subsequent stagnation of the reaction suggest that while NaOH triggers a fast initial breakdown of the precursor structure, it may not promote complete topochemical transformation. This contrasts with the LiOH system, where a slow change step from ~200 min to ~850 min was followed by a sharp increase in product crystallinity after 1000 minutes. It is therefore possible that the NaOH system had not yet entered its second-stage transformation within the 800-minute reaction window.

Unfortunately, due to time slot constraints at the synchrotron facility (APS), we were unable to extend the measurement beyond 800 minutes. As such, it remains unclear whether the observed plateau in the NaOH system reflects a true kinetic bottleneck, insufficient structural match for $Na^+$ intercalation, or simply a delayed transformation process that would require longer durations to proceed.

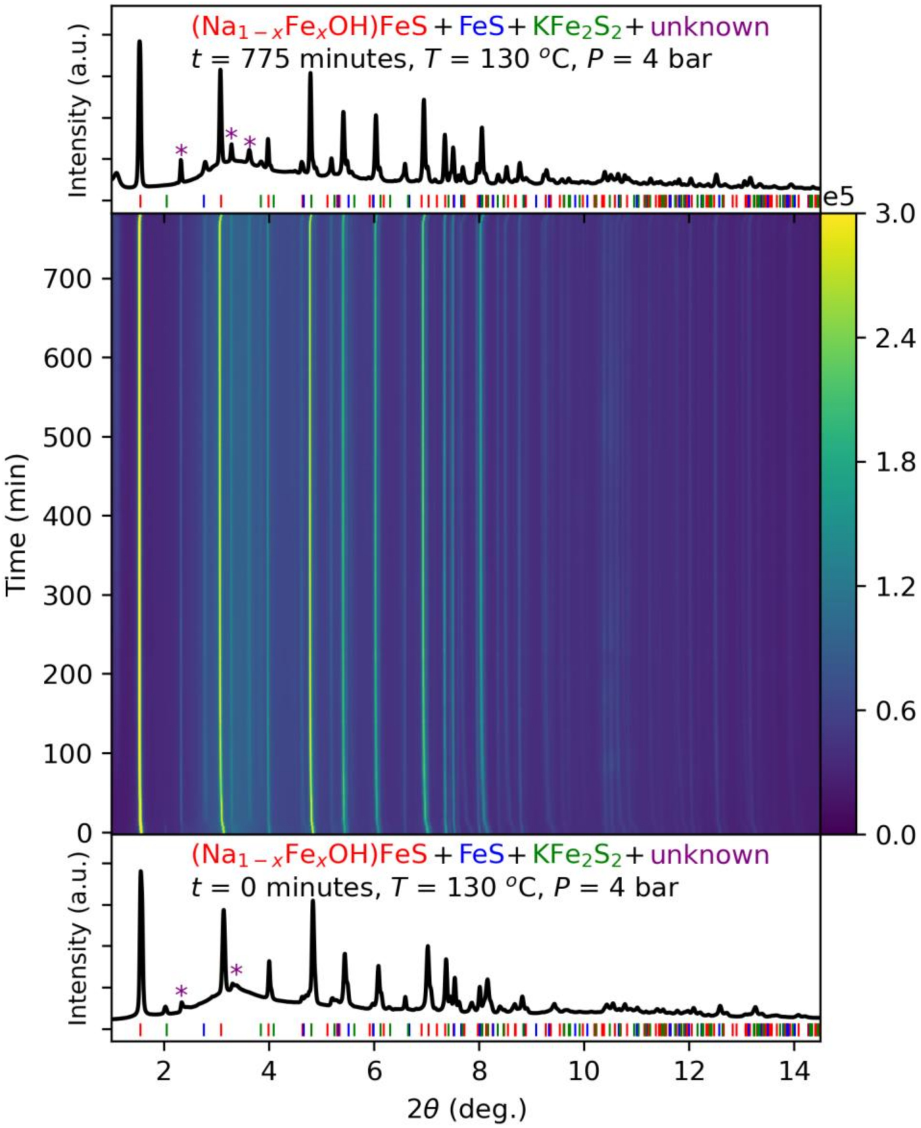

Figure 5.8: In-situ synchrotron PXRD contour plot of the hydrothermal reaction between Fe powder, NaOH, and thiourea, at 130 °C and 4 bar. The initial (bottom) and final (top) diffraction patterns correspond to $t = 0$ min and $t = 775$ min, respectively. The formation of (Na$_{1-x}$Fe$_x$OH)FeS (red), FeS (blue), and KFe$_2$S$_2$ (green) phases is observed, along with additional unidentified reflections (purple asterisks). The contour reveals gradual crystallization behavior of KFe$_2$S$_2$ and the layered hydroxide Fe phase, with persistent unidentified peaks suggesting a possible intermediate or minor impurity phase. Tick marks below each pattern denote reference reflections for the identified phases.

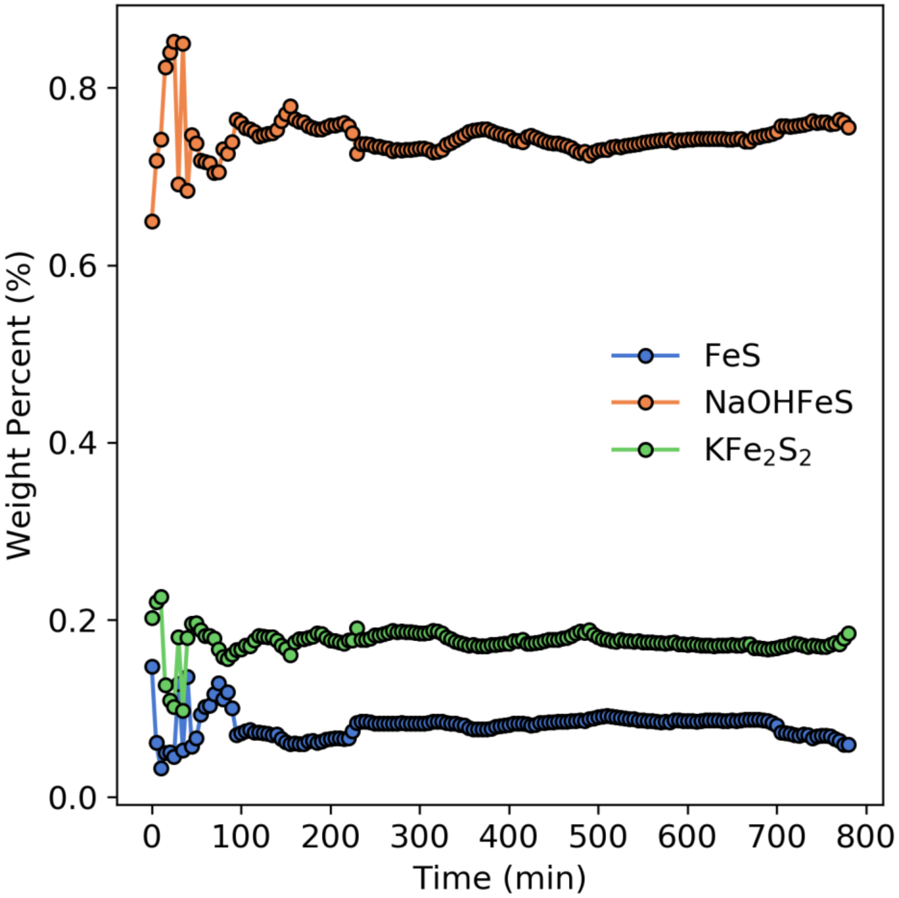

Figure 5.9: Evolution of the relative weight percentages of crystalline phases during the hydrothermal reaction of Fe powder, NaOH, and thiourea at 130 °C and 4 bar, as determined by sequential Rietveld refinement. The dominant product is $(Na_{1-x}Fe_xOH)FeS$ (orange), which forms rapidly and stabilizes early in the reaction. Minor phases include $KFe_2S_2$ (green) and FeS (blue), both of which appear at early stages and persist throughout the experiment at relatively low concentrations.

If the reaction is indeed fundamentally stalled, this could stem from multiple factors. First, the larger ionic radius and weaker hydration of $Na^+$ relative to $Li^+$ can hinder stable intercalation into the FeS-based layered framework, potentially destabilizing intermediate structures or preventing complete layer reassembly. In addition, NaOH's higher basicity may promote rapid structural breakdown of $KFe_2S_2$ without allowing sufficient time for controlled topochemical rearrangement. It should also be noted that unlike the previous reaction system, we did not add extra Fe powder at the beginning in the NaOH-$KFe_2S_2$ system. Limited availability of $Fe^{2+}$, either from insufficient oxidation of metallic Fe or lack of redox cycling in the system, may constrain hydroxide layer growth, leading to incomplete intercalation and structural lock-in. These factors suggest that while NaOH initiates transformation quickly, it lacks the necessary structural and redox balance to drive full top-down conversion under these conditions.

### 5.3.4 $KFe_2Se_2$ deintercalation with LiOH

The reaction in the $KFe_2Se_2$ and LiOH system proceeds through a gradual intercalation-driven pathway that partially preserves the layered FeSe framework. This process parallels the behavior observed in the sulfide analogue, $KFe_2S_2$, but exhibits distinct structural dynamics and kinetic features associated with the larger and more polarizable $Se^{2-}$ anion. As shown in the time-resolved PXRD contour plot (Figure 5.10), the initial conversion is rapid: reflections from $KFe_2Se_2$ diminish significantly within the first few hundred minutes, while $(Li_{1-x}Fe_xOH)FeSe$ begins to form concurrently. Two unidentified low-angle reflections emerge transiently and disappear within the first 300 minutes, suggesting the involvement of a short-lived disordered intermediate, possibly a partially deintercalated phase or solvated complex.

The sequential refinements reveal that the formation of $(Li_{1-x}Fe_xOH)FeSe$ is continuous but slow. The product increases gradually from ~30% at $t = 0$ to ~37% after 1400 minutes, without any abrupt phase transition or crystallization surge. In contrast to the sulfide system, where the reaction temporarily stagnates before sharply accelerating beyond 1000 minutes, the selenide reaction shows no distinct inflection point, indicating a more diffusely distributed transformation. The precursor $KFe_2Se_2$ is only partially consumed (~17% remains), and FeSe appears briefly in the early stage before decreasing, suggesting competition between direct FeSe formation and intercalated phase assembly.

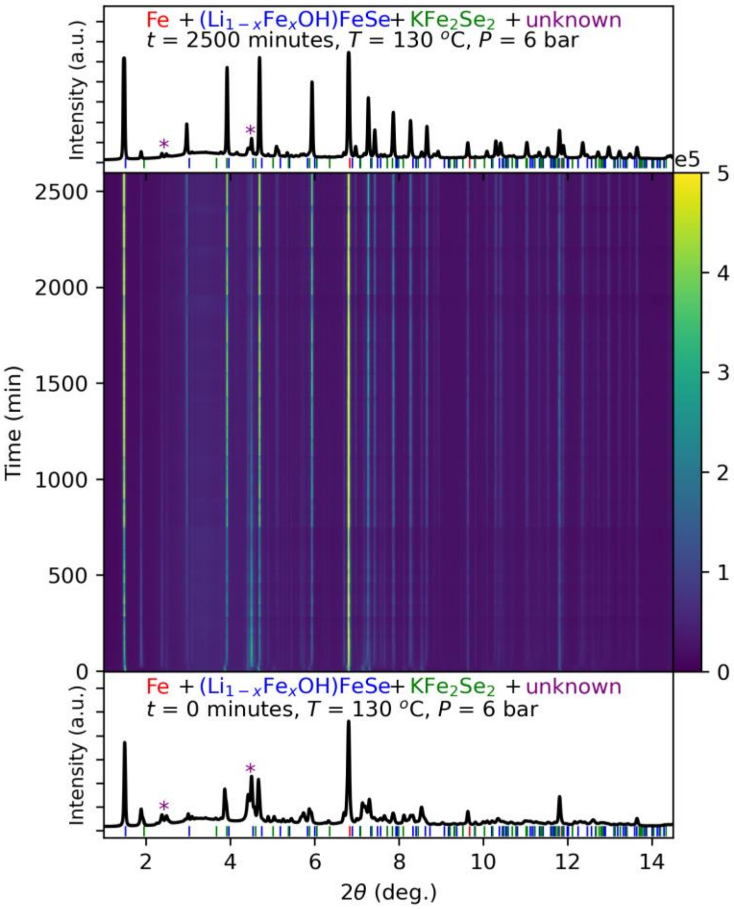

Figure 5.10: In-situ synchrotron powder X-ray diffraction contour plot showing the time-resolved structural evolution of the $KFe_2Se_2$ + LiOH system under hydrothermal conditions (130 °C, 6 bar). Diffraction data were collected continuously over 2500 minutes. Reflections from the precursor $KFe_2Se_2$ gradually diminish, while peaks corresponding to the intercalated phase $(Li_{1-x}Fe_xOH)FeSe$ grow in intensity. Two transient low-angle reflections (marked by asterisks) are observed in the early stage and disappear after ~300 minutes, likely associated with short-lived intermediates. A small amount of Fe and an unknown phase persist throughout the reaction, while the transformation progresses gradually without a sharp phase transition.

Lattice parameter evolution provides further mechanistic insight (Figure 5.11). $KFe_2Se_2$ undergoes a slight contraction in the a-axis and a subtle expansion in the c-axis, which may be attributed to partial deintercalation of $K^+$ and the temporary insertion of small species such as $H_2O$ or $OH^-$ between the layers. These changes suggest that the structure is not fully broken down but experiences interlayer disruption that facilitates reorganization. The FeSe phase exhibits minor contraction in both axes, possibly due to stress relaxation or its displacement by the growing intercalated product.

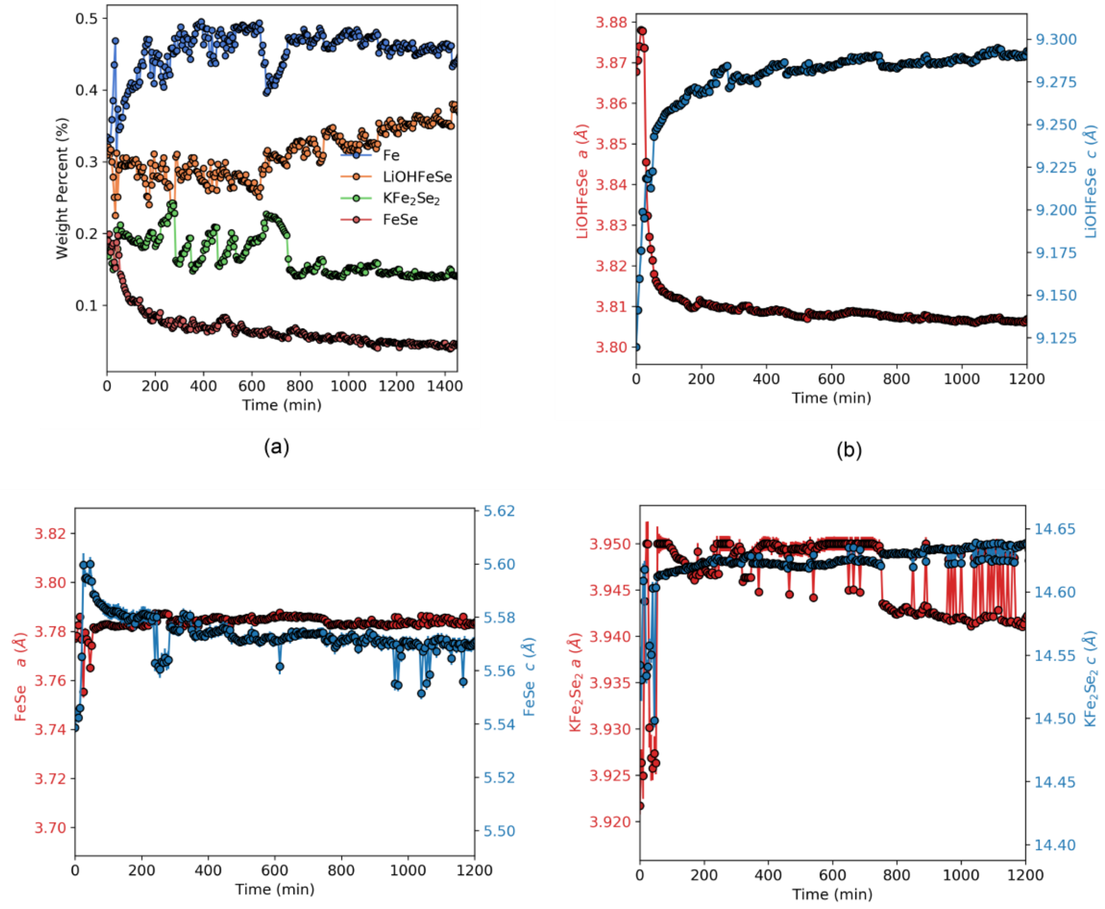

(a) (b)

(c) (d)

Figure 5.11: Summary of structural evolution during the hydrothermal reaction of $KFe_2Se_2$ in LiOH at 130 °C and 6 bar. (a) Weight percent of major crystalline phases as a function of reaction time, obtained from in-situ sequential Rietveld refinement. The ($Li_{1-x}Fe_xOH$)FeSe phase gradually increases while $KFe_2Se_2$ is only partially consumed. FeSe appears as an intermediate, and metallic Fe accumulates early and remains largely unreacted. (b) Lattice parameters of ($Li_{1-x}Fe_xOH$)FeSe showing a steady contraction in the a-axis and a continuous expansion in the c-axis, indicative of in-

plane ordering and progressive intercalation. (c) Lattice parameters of FeSe show slight contraction in both axes, possibly due to stress relaxation or competition with the intercalated phase. (d) $KFe_2Se_2$ shows a small decrease in the a-axis and a subtle increase in the c-axis, consistent with partial deintercalation and temporary interlayer perturbation without full structural collapse.

In contrast, $(Li_{1-x}Fe_xOH)FeSe$ shows a distinct structural evolution characteristic of progressive intercalation. The a-axis decreases steadily, indicating improved in-plane ordering within the FeSe layers, while the c-axis expands from ~9.15 to 9.30 Å over time. This expansion reflects the gradual incorporation of $Li^+$ and $OH^-$ species into the interlayer gallery, accompanied by enhanced crystallinity and stabilization of the final layered structure.

The metallic Fe added to the system accumulates to nearly 50% and remains largely unreacted, suggesting that only a portion of the Fe is oxidized and incorporated into the hydroxide layers. This partial consumption contrasts with the LiOH–sulfide system, where Fe is more fully utilized over time. The lower degree of Fe utilization in the selenide system may reflect either a weaker driving force for redox cycling or a kinetic limitation in $Fe^{2+}$ transport and insertion.

In summary, the hydrothermal transformation of $KFe_2Se_2$ in LiOH follows a broadly similar pathway to its sulfide counterpart but proceeds more gradually and remains incomplete within the measured timeframe. The selenide host shows greater structural persistence and a slower top-down conversion, highlighting the impact of chalcogen identity on interlayer reactivity, crystallization kinetics, and redox balance in intercalation-driven hydrothermal reactions.

### 5.3.5 Bottom-up ammonia intercalation into FeS

The hydrothermal reaction of elemental Fe with thiourea and guanidine at 150 °C and 7 bar leads to the formation of the previously reported ammonia- and proton-intercalated layered compound $(H_{0.5}NH_3)Fe_2S_2$, as established by Zhou et al. [66]. In the work, guanidine serves as a strong, metal-

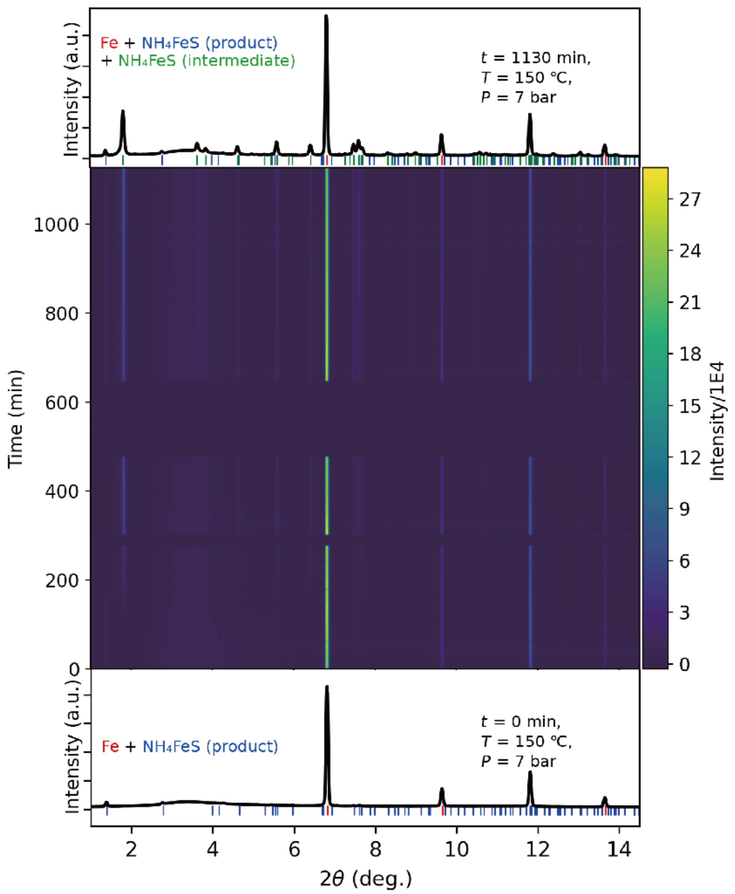

Figure 5.12: In-situ synchrotron powder X-ray diffraction contour plot showing the hydrothermal formation of $(H_{0.5}NH_3)Fe_2S_2$ from Fe, thiourea, and guanidine at 150 °C and 7 bar. The transformation proceeds over 1100 minutes, involving a transient intermediate phase with P4/nmm symmetry that exhibits fluctuating Bragg reflections during the first half of the reaction. The final product adopts an I4/mmm structure, with stable reflections corresponding to the layered intercalated compound. Two short periods of missing data between 280–300 min and 480–650 min result from temporary beamline interruptions. The persistent presence of unreacted Fe and gradual product peak growth reflect the slow redox kinetics and limited intercalation yield under these weakly reducing, metal-free conditions.

free base (pKa ≈ 13.6) that facilitates Fe digestion and gradually releases $NH_3$ via thermal decomposition above 150 °C. These ammonia molecules, along with protons generated in situ, act as the sole intercalating species—demonstrating that neither alkali metal cations nor external oxidants are required to stabilize the layered product.

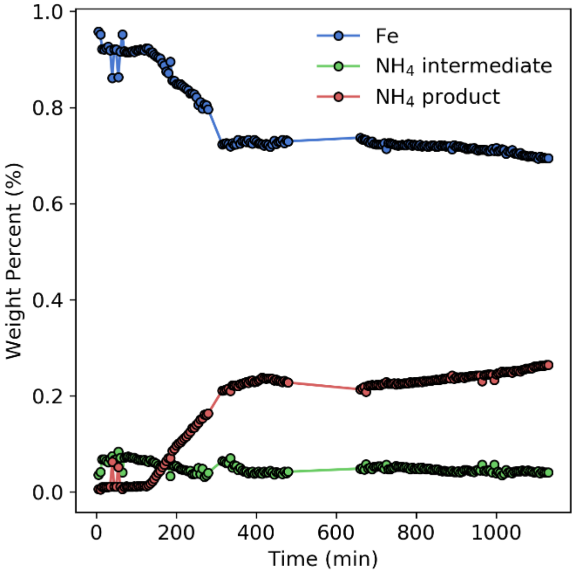

Figure 5.13: Time-dependent phase composition during the hydrothermal synthesis of $(H_{0.5}NH_3)Fe_2S_2$ at 150 °C and 7 bar, extracted via in-situ Rietveld refinement of synchrotron PXRD data. The product phase (red), corresponding to the I4/mmm-structured $(H_{0.5}NH_3)Fe_2S_2$, gradually increases in weight fraction, reaching ~25% after 1000 minutes. A crystalline intermediate phase with P4/nmm symmetry (green) appears early but remains minor (<8%) and disappears over time. Metallic Fe (blue) remains the dominant phase throughout the experiment, decreasing only slightly in the first 300 minutes before plateauing, indicating slow $Fe^0$ oxidation and incomplete conversion. The sluggish kinetics are consistent with the weak redox environment provided by thiourea and guanidine decomposition.

In our current in-situ synchrotron XRD study, the formation of $(H_{0.5}NH_3)Fe_2S_2$ is directly observed over 1100 minutes. The transformation proceeds through a crystalline intermediate with P4/nmm symmetry, which exhibits fluctuating lattice parameters indicative of a metastable and partially ordered phase. This intermediate exists only transiently and never dominates the phase composition. The final product adopts the I4/mmm space group, consistent with the 122-type body-centered tetragonal structure previously reported. Its stable c-axis (~15.1 Å) confirms the interlayer incorporation of ammonia and protons, likely stabilized by hydrogen bonding with the chalcogenide layers.

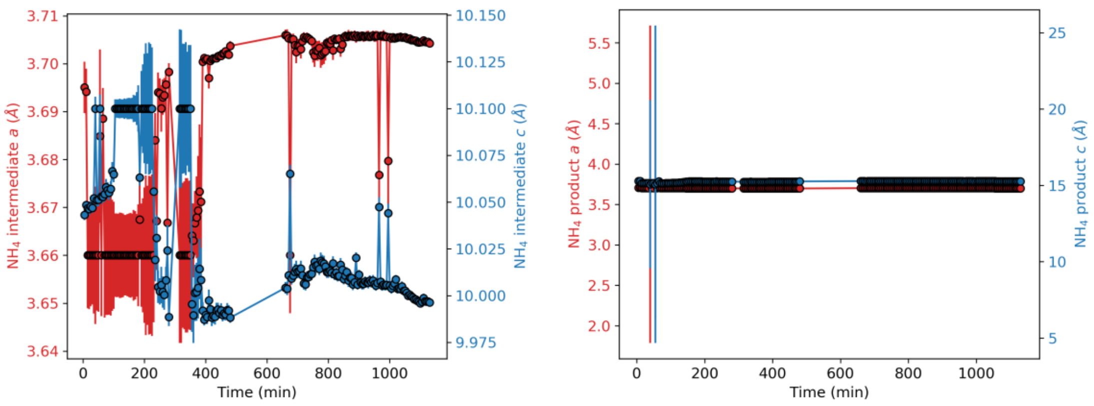

(a) (b)

Figure 5.14: Lattice parameter evolution of the intermediate (a) and product (b) phases during the hydrothermal reaction of Fe, thiourea, and guanidine at 150 °C and 7 bar. The intermediate phase, indexed in space group *P*4/*nmm*, exhibits substantial fluctuations in both *a* and *c* axes during the early reaction stage, reflecting structural instability or poor crystallinity. After ~500 minutes, the lattice constants stabilize as the intermediate transitions to the final product. The product phase, indexed in *I*4/*mmm*, displays sharp and stable lattice parameters from its initial appearance, with $a \approx 3.73$ Å and $c \approx 15.1$ Å, consistent with previously reported layered $(H_{0.5}NH_3)Fe_2S_2$ structures.

Quantitative sequential Rietveld analysis shows that Fe is only partially consumed, remaining above 60 wt% throughout the reaction—indicating a sluggish oxidation process and incomplete conversion. The reaction lacks the strong chemical driving forces typical of LiOH or Birch-type reducing agents. This is reflected in the gradual and partial growth of the product phase, which reaches ~25 wt% after nearly 1000 minutes, and the persistence of metallic Fe. The weakly reducing environment provided by guanidine and thiourea decomposition products appears insufficient to fully convert $Fe^0$ to $Fe^{2+}$, thereby limiting intercalation yield. Two periods of missing diffraction data between 280–300 min and 480–650 min resulted from temporary beamline interruptions. No abrupt changes in lattice parameters are observed before or after these intervals, suggesting that key structural events were not missed.

This slow and partial topochemical transformation highlights the delicate interplay between proton/ammonia availability, redox chemistry, and structural reorganization. The product

$(H_{0.5}NH_3)Fe_2S_2$ benefits from enhanced thermal stability relative to pure FeS, likely due to strong hydrogen bonding between $NH_3/H^+$ and $S^{2-}$ layers, as previously supported by neutron diffraction and DSC studies. However, no superconductivity was observed, possibly due to Fe site vacancies and electron over-doping, both of which are known to suppress superconductivity in Fe-based chalcogenides.

### 5.3.6 Bottom-up solvothermal intercalation of ethylenediamine into CoS

The formation of $Co(en)_3Cl_2$ through the reaction of Co metal, $NH_4Cl$, and ethylenediamine was observed directly in the in-situ X-ray contour plot even before the heating stage, indicating its precipitation at room temperature. Upon heating to 140 °C, the diffraction peaks of the target layered product $[Co(en)3](CoS)_{12}\cdot en$ (hereafter referred to as en-CoS, as we did in Chapter 3) began to emerge at approximately 200–240 minutes and continued to grow in intensity throughout the experiment. Although en-CoS is the desired phase, sequential Rietveld refinement revealed that $Co(en)_3Cl_2$ was the dominant product by weight during the solvothermal process and formed more rapidly than the layered phase.

The lattice parameter analysis showed that the c-axis of en-CoS exhibited a sharp increase of ~0.1 Å upon its initial crystallization, stabilizing at ~20.36 Å without further significant change. This one-step expansion of the interlayer spacing suggests that en-CoS does not form via a post-synthetic intercalation of $[Co(en)_3]^{2+}$ cations into a preformed CoS host lattice. Rather, the data support a synchronous growth mechanism, where the CoS layers and $[Co(en)_3]^{2+}$/en interlayers assemble cooperatively during crystallization. This is consistent with the final orthorhombic $Pca2_1$ space group structure determined from single-crystal X-ray diffraction, in which the ordering of the $[Co(en)_3]^{2+}$ cations breaks the fourfold symmetry of the CoS layers, yielding a polar metal.

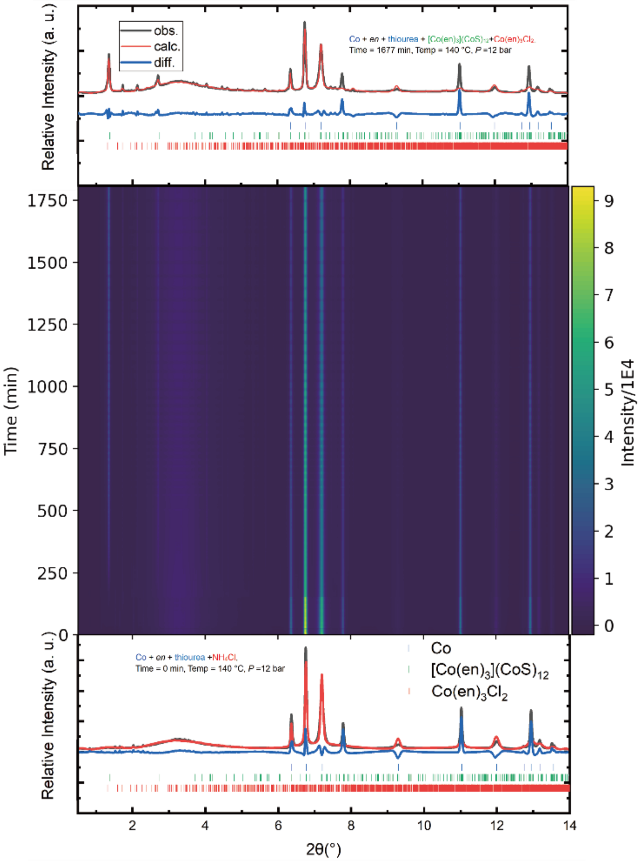

Figure 5.15: In-situ synchrotron powder X-ray diffraction contour plot showing the solvothermal reaction of Co metal, thiourea, and ethylenediamine at 140 °C and 12 bar. Reflections from $Co(en)_3Cl_2$ appear early, even before full heating, consistent with its precipitation at room temperature. At ~200–240 minutes, diffraction peaks corresponding to the layered product [Co(en)3](CoS)12·en begin to emerge and steadily increase in intensity. The two phases grow concurrently throughout the reaction, reflecting parallel coordination and redox pathways. Metallic Co remains detectable, indicating incomplete consumption within the experimental window. The slow and anisotropic crystallization behavior is characteristic of solvothermal synthesis in viscous organic solvents.

Time-resolved phase quantification shows that both en-CoS and $Co(en)_3Cl_2$ evolve concurrently, rather than via sequential conversion. The parallel evolution of $Co(en)_3Cl_2$ and en-CoS suggests that multiple coordination and redox pathways coexist in the solvothermal environment. $[Co(en)_3]^{2+}$ readily forms through the oxidation of $Co^0$ in the presence of $NH_4^+$ and ethylenediamine, as indicated by the continuous gas evolution (presumably $H_2$) observed in the in-situ reaction cell. The

$[Co(en)_3]^{2+}$ then either precipitates with $Cl^-$ as $Co(en)_3Cl_2$ or integrates into the forming layered framework with CoS and ethylenediamine.

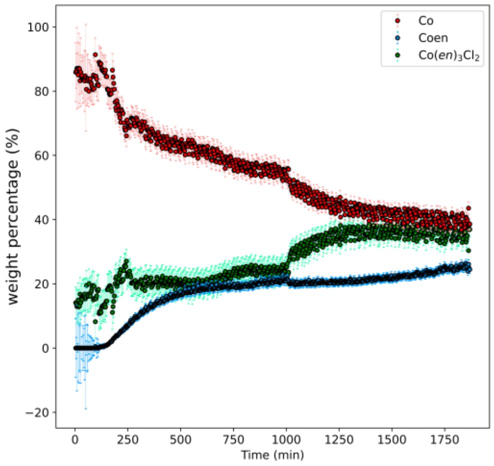

Figure 5.16: Phase evolution during the solvothermal synthesis of [Co(en)3](CoS)12·en at 140 °C and 12 bar, derived from in-situ Rietveld refinement. $Co(en)_3Cl_2$ forms rapidly and remains the dominant crystalline phase throughout the reaction, suggesting fast coordination of $[Co(en)_3]^{2+}$ with $Cl^-$. The layered en-CoS phase begins to form at ~240 minutes and steadily increases in weight fraction, ultimately reaching ~30% at the end of the experiment. Metallic Co is gradually consumed but remains present, indicating incomplete oxidation. The concurrent formation of both products implies parallel reaction pathways rather than a sequential transformation.

The early precipitation and stability of $Co(en)_3Cl_2$ suggest it may also serve a templating or seeding role during en-CoS formation. However, since $Co(en)_3Cl_2$ and en-CoS crystallize simultaneously and independently, their formation appears to reflect a competition between ligand complexation and sulfur incorporation pathways. Notably, similar behavior has been observed in related solvothermal systems: Konvir et al. reported the early appearance and eventual disappearance of $Fe(en)_3Cl_2$ in their in-situ synthesis of $[Fe(en)_3]_4(Fe_{14}Se_{21})Cl_2$, although in their case the starting $Fe^{2+}$ salt and high solubility of the complex influenced the observed kinetics. [201] In our case, the persistence of metallic Co and the steady (but incomplete) growth of en-CoS throughout the entire ~1800 min experiment suggest that the synthesis had not reached completion within the allotted beamtime. This is consistent with the slow kinetics typical of solvothermal in-situ reactions, particularly in organic solvents with high viscosity. Compared to hydrothermal reactions, where water facilitates rapid ion transport and redox processes, the ethylenediamine-based system appears diffusion-limited. This could explain both the slow metal consumption and the moderate crystallinity of the products, particularly in more complex systems such as CoSe or FeSe analogues.

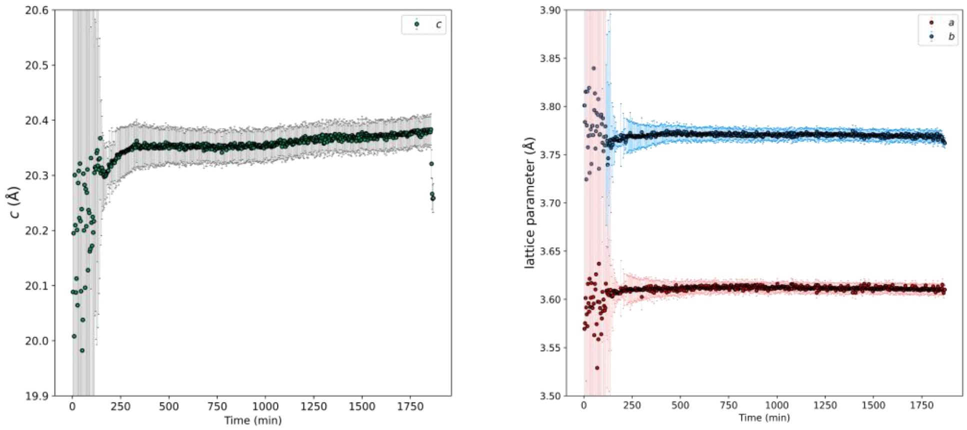

(a) (b)

Figure 5.17: Time evolution of the lattice parameters of [Co(en)3](CoS)12·en obtained from sequential Rietveld refinements during the solvothermal reaction of Co, thiourea, and ethylenediamine. (a). The *c*-axis exhibits a rapid increase to ~20.36 Å around 240 minutes, followed by a gradual stabilization, indicating the onset and completion of en-CoS layer growth. (b). The *a*- and *b*-axes also stabilize after an initial fluctuation, reflecting the anisotropic growth behavior and structural ordering during the formation of the polar orthorhombic phase (space group *Pca*$2_1$). Error bars represent refinement uncertainties. The shaded regions highlight early-time fluctuations associated with nucleation.

### 5.3.7 Bottom-up solvothermal intercalation of 1,2-diaminopropane into CoS.

To further understand the role of diamine structure and solvent dynamics in solvothermal reactions, we compare the in-situ crystallization behavior of en-CoS and CoS-1,2-dap. While both reactions involve Co metal, thiourea, and a diamine ligand, the progression and crystallinity of their layered products show notable differences.

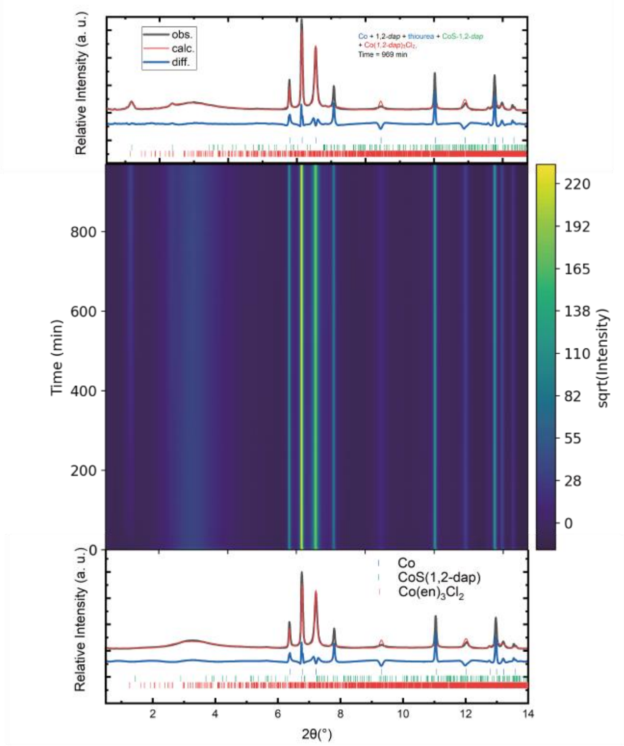

Figure5.18: In-situ synchrotron powder X-ray diffraction contour plot showing the solvothermal reaction of Co metal, thiourea, and 1,2-diaminopropane (1,2-dap) at 140 °C and ~12 bar. Bragg reflections from the intermediate Co(1,2-dap)$_3$Cl$_2$ complex appear around 300 minutes, preceding the emergence of peaks corresponding to the layered product CoS-1,2-dap, which become detectable after ~400 minutes. The metallic Co reflections persist throughout, indicating incomplete oxidation and low conversion. Compared to the en-based system, the peak intensities for CoS-1,2-dap remain weak and broad, suggesting poor crystallinity and slower reaction kinetics. This contour plot highlights the impact of ligand structure and solvent viscosity on product formation and crystallization behavior in solvothermal synthesis.

In the en-CoS system, diffraction peaks corresponding to en-CoS emerge around 240 minutes, and their intensity continues to rise steadily throughout the experiment. The lattice parameters, especially the c-axis, show a distinct one-step increase and stabilize at ~20.36 Å, indicating synchronous growth of the CoS layers and intercalated $[Co(en)_3]^{2+}$ complexes. The product exhibits high crystallinity with sharp and well-defined peaks, reflecting coherent stacking and robust layer formation.

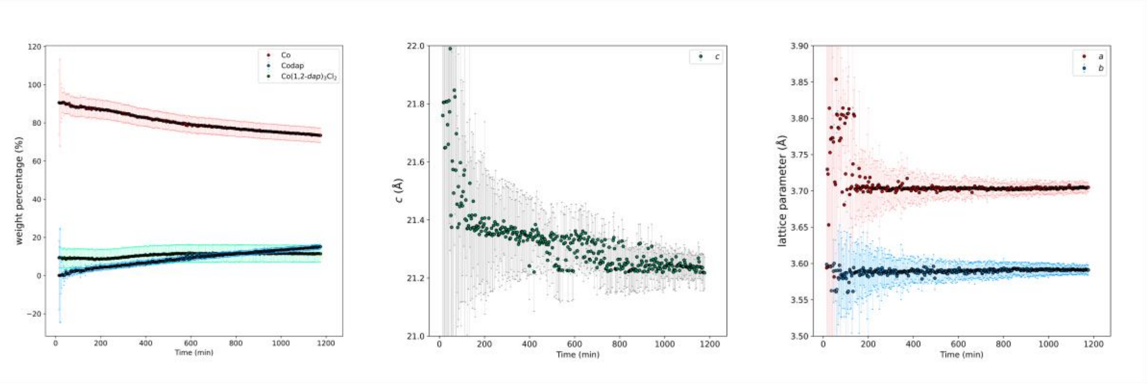

(a) (b) (c)

Figure 5.19: Time-resolved evolution of crystalline parameters during the solvothermal synthesis of CoS–1,2-dap. (a). Quantitative phase analysis showing the weight percent evolution of metallic Co, CoS–1,2-dap, and $[Co(1,2\text{-}dap)_3]Cl_2$. The consumption of Co and slow accumulation of the product highlight the sluggish reaction kinetics. (b). Evolution of the *c*-axis lattice parameter of CoS–1,2-dap, which gradually decreases from ~21.8 Å to ~21.2 Å, likely due to slow solvent loss or framework contraction. (c). Evolution of the *a*- and *b*-axis parameters of CoS–1,2-dap, showing initial anisotropic changes that stabilize over time, indicating structural relaxation and improved ordering.

In contrast, the CoS-1,2-dap system displays a delayed and less defined crystallization process. The diffraction peaks of $Co(1,2\text{-}dap)_3Cl_2$ appear early (~300 min), but the layered product CoS-1,2-dap only becomes evident around 400–500 minutes, with weaker and broader peaks. This temporal sequence indicates that $Co^{2+}$ preferentially forms coordination complexes with 1,2-dap before engaging in the formation of the layered Co–S framework. Moreover, phase percentage analysis shows that $Co(1,2\text{-}dap)_3Cl_2$ remains the dominant crystalline phase throughout the reaction, exceeding CoS-1,2-dap in abundance, which further confirms the strong competitive binding of 1,2-dap to $Co^{2+}$. The c-axis stabilizes at a significantly shorter value (~15.6 Å), and the large fluctuations and error bars in a, b, c parameters reveal poor crystallinity. Weight percentage data also confirm that $Co(1,2\text{-dap})_3Cl_2$ dominates the reaction, and CoS-1,2-dap remains a minority phase throughout the entire duration.

The c-axis shows a gradual decrease (~0.2 Å) during the 1000-minute reaction. This could suggest slow structural reorganization, possible solvent loss, or the gradual relaxation of strain within the layered framework. However, considering the relatively poor crystallinity and the large error bars associated with the refinement, such a trend must be interpreted cautiously. It is possible that the observed decrease in c is partially influenced by refinement uncertainties arising from overlapping peaks, weak diffraction intensity, and broadened reflections.

The disparity likely stems from the structural and physical differences between ethylenediamine and 1,2-diaminopropane. 1,2-dap has a higher viscosity, which can significantly slow diffusion and particle interaction, especially under solvothermal conditions. Moreover, its additional methyl group introduces steric hindrance, possibly disrupting ordered stacking or templated growth of the layered structure. As a result, while $[Co(en)_3]^{2+}$ seems to act as a templating species for en-CoS, no such templating effect is apparent in the 1,2-dap system.

### 5.3.7 Bottom-up solvothermal intercalation of 1,2-diaminopropane into FeS.

The solvothermal reaction between iron powders, thiourea, and 1,2-diaminopropane (1,2-dap) proceeds via a slow and direct formation of FeS(1,2-dap), as revealed by in-situ X-ray diffraction. Compared with analogous Co-based reactions, the conversion of Fe is markedly slower, with metallic Fe still accounting for over 85% of the crystalline phases even after 960 minutes at 200 °C. The contour plot shows that reflections corresponding to FeS(1,2-dap) begin to emerge only after ~400 minutes, and grow gradually thereafter, suggesting sluggish nucleation and growth. Unlike the Co/1,2-dap system where $Co(1,2\text{-dap})_3Cl_2$ is a dominant intermediate crystalline phase, no signals from $Fe(1,2\text{-dap})_3Cl_2$ are observed throughout the Fe-based reaction. This can likely be attributed to the significantly higher solubility of $Fe^{2+}$-diamine complexes in 1,2-dap, in contrast to their Co counterparts. The $Fe(1,2\text{-}dap)_3^{2+}$ complex, although expected to form rapidly in solution upon Fe oxidation, likely remains fully dissolved and does not precipitate under these conditions, precluding its detection by diffraction. This behavior is consistent with previous reports showing that $Fe(en)_3Cl_2$ readily dissolves at elevated temperatures in diamine solvents, while $Co(en)_3Cl_2$ tends to crystallize.

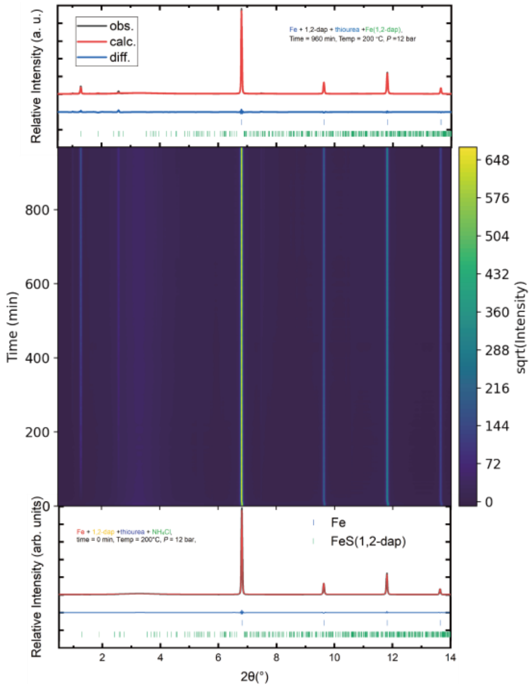

Figure 5.20: In-situ synchrotron powder X-ray diffraction contour plot of the solvothermal reaction between Fe, thiourea, and 1,2-diaminopropane (1,2-dap) at 200 °C and ~12 bar. Reflections from FeS(1,2-dap) gradually emerge after ~400 minutes and slowly intensify, indicating sluggish crystallization. No intermediate phases such as $Fe(1,2\text{-}dap)_3Cl_2$ are observed throughout the reaction. Top and bottom panels show Rietveld refinements of the final and initial patterns, respectively, with tick marks corresponding to Fe (blue) and FeS(1,2-dap) (green).

The extracted lattice parameters of FeS(1,2-dap) indicate an initial elongation of the c-axis (~21.9 Å), followed by a contraction and stabilization at ~21.3 Å. This may suggest initial disordered interlayer solvation that evolves into a more ordered structure. The a and b axes show noisy and scattered values, especially the b-axis, indicating poor crystallinity and possibly anisotropic growth or stacking disorder. The generally weak and broad Bragg reflections support the conclusion that crystallite quality is limited, which is also reflected in the refinement uncertainty.

Taken together, these observations suggest that FeS(1,2-dap) forms via a slow, solution-mediated pathway, with $Fe^{2+}$ coordination and sulfur incorporation occurring directly without stable intermediate crystallization. The absence of $Fe(1,2\text{-dap})_3Cl_2$ precipitation further reinforces the unique coordination chemistry and solubility profile of $Fe^{2+}$ in 1,2-dap. Compared to ethylenediamine, 1,2-dap's higher viscosity and steric hindrance likely slow diffusion and complexation, contributing to the lower crystallinity and slower kinetics observed.

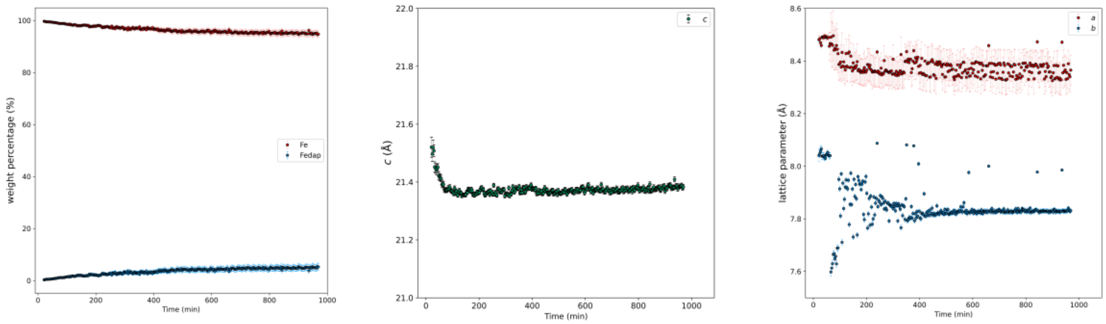

(a)

(b)

(c)

Figure 5.21: Time-resolved structural evolution during the solvothermal synthesis of FeS(1,2-dap) from Fe, thiourea, and 1,2-diaminopropane at 200 °C and ~12 bar. **(a)** Phase weight percentages of Fe (red), FeS(1,2-dap) (blue), and their evolution over time, showing gradual Fe consumption and product formation. **(b)** c-axis lattice parameter of FeS(1,2-dap), exhibiting a rapid initial contraction followed by a plateau at ~14.5 Å. **(c)** a- and b-axis parameters of FeS(1,2-dap), which stabilize after an initial fluctuation, indicative of structural ordering during crystal growth.

### 5.3.9 Summary.

We systematically investigated the time-resolved crystallization processes of eight hydrothermal and solvothermal reactions involving Fe and Co-based transition metal chalcogenides using in-situ synchrotron X-ray diffraction. These reactions span both bottom-up and top-down strategies and encompass aqueous and diamine-based solvents. By tracking phase evolution, lattice parameter changes, and reaction kinetics under relevant synthetic conditions, we obtained direct mechanistic insight into the formation of layered intercalated structures that are otherwise obscured in conventional ex-situ approaches.

Hydrothermal systems, particularly those based on LiOH and $NH_4^+$, displayed rapid and robust formation of intercalated FeS or FeSe frameworks. The $(Li_{1-x}Fe_xOH)FeS$ system, in particular, followed a two-stage reaction pathway—from initial $Fe^{2+}$ intercalation to subsequent $Li^+$ substitution—highlighted by a continuous rise in the c-axis and a clear shift in reaction kinetics. In contrast, NaOH-mediated deintercalation reactions initiated rapidly but then plateaued, indicating incomplete transformation. The larger $Na^+$ ion, stronger basicity, and lack of added $Fe^{2+}$ may have limited further conversion by destabilizing the interlayer structure or stalling redox processes. In the selenide analogue $KFe_2Se_2$, top-down conversion occurred more gradually and remained incomplete over the full reaction window, reflecting the lower redox activity and structural rigidity of the Se-based host. Notably, the ammonia-driven reaction using guanidine yielded an intercalated $(H_{0.5}NH_3)Fe_2S_2$ product via a transient P4/nmm intermediate, confirming that metal-free intercalation can proceed under hydrothermal conditions, albeit slowly and with low yield.

Solvothermal systems showed markedly slower kinetics and greater sensitivity to solvent identity. The reaction of Co with thiourea in ethylenediamine (en) formed both $[Co(en)_3]Cl_2$ and the polar layered product en-CoS, with in-situ data revealing their synchronous crystallization and suggesting cooperative growth of the CoS layers and molecular interlayers. In contrast, the analogous system using 1,2-diaminopropane (1,2-dap) yielded CoS-1,2-dap with lower crystallinity and delayed onset, likely due to 1,2-dap's higher viscosity and steric hindrance. The Fe + 1,2-dap system followed a similarly sluggish trajectory, with no observable Fe-diamine complex precipitation, in contrast to the Co case. This reflects the higher solubility of $Fe^{2+}$ complexes in 1,2-dap and suggests a more homogeneous, solution-mediated reaction pathway.

These results highlight several governing principles for in-situ intercalation under hydrothermal and solvothermal conditions. First, redox strength and precursor solubility strongly dictate reaction rate and completeness. Second, interlayer expansion and lattice parameter evolution provide a reliable fingerprint for distinguishing synchronous growth from post-synthetic intercalation. Third, subtle variations in solvent properties—such as viscosity, basicity, and coordination geometry—exert pronounced effects on crystallization dynamics, phase purity, and structural order. By coupling in-situ diffraction with phase and lattice analysis, we offer not only mechanistic clarity but also predictive guidance for the rational design of intercalated quantum materials using soft chemical methods.

## 5.4 Conclusion

In this chapter, we employed in-situ synchrotron powder diffraction to track the time-resolved crystallization of layered transition metal chalcogenides under both hydrothermal and solvothermal conditions. These real-time observations revealed key mechanistic differences among various synthetic strategies and ligand environments.

The hydrothermal experiments involving LiOH and $NH_4^+$ demonstrate a two-step process: initial FeS or FeSe intermediates form first, followed by a sharp structural rearrangement into layered hydroxide chalcogenides. This is consistent with earlier in-situ studies of microporous tin sulfides by O'Hare et al., where a disordered lamellar intermediate was observed prior to the formation of TMA-SnS-1, and reaction temperature was found to be the most critical variable determining crystallinity. Similarly, in our $NH_4^+$-FeS system, we observed two well-separated growth stages with lattice parameter shifts, indicative of dynamic structural evolution and possible hydrogen bonding stabilization—as was confirmed in neutron studies on ammonia intercalation by Zhou et al..

In contrast, the solvothermal systems displayed slower kinetics and a higher dependency on ligand geometry and viscosity. In particular, reactions involving 1,2-diaminopropane were significantly retarded, possibly due to hindered diffusion. The formation of $Co(en)_{312}\cdot en$ (en-CoS) proceeded via cooperative growth of molecular and extended layers. The absence of detectable CoS intermediates or multiple c-axis jumps implies synchronous framework assembly—a behavior reminiscent of that reported by O’Hare and co-workers for ULM-5 formation, where certain reagent combinations led to direct product crystallization without intermediate phases.

Across systems, the presence or absence of intermediate phases, the onset and duration of induction periods, and the evolution of lattice parameters all serve as important indicators of the underlying transformation mechanisms. In light of previous reports that crystallization pathways may be strongly reagent-dependent, even for the same product, our results reinforce the value of high-resolution in-situ diffraction in decoding synthetic complexity.

# Chapter 6: Conclusion and future work

## 6.1 Introduction

In this dissertation, we systematically investigated how molecular intercalation can be used to engineer symmetry breaking—particularly polar and chiral asymmetry—in (TMCs), leading to emergent quantum properties such as ferromagnetism and superconductivity. Across several chapters, we demonstrated that both structural polarity and molecular chirality can be rationally introduced into layered or tetrahedral frameworks through the incorporation of designed amine species.

In Chapter 3, we reported the solvothermal synthesis of ethylenediamine-based CoS hybrids, where polar distortions were induced by directional hydrogen bonding between chiral $Co(en)_3^{2+}$ complexes and the CoS host lattice. This polar arrangement was directly linked to the emergence of ferromagnetic order in a metallic state, constituting a rare example of a polar ferromagnetic metal derived from molecule–solid interactions.

In Chapter 4, we extended our focus to 2H-$TaSe_2$, a van der Waals layered compound with centrosymmetric bulk symmetry. Through intercalation of both achiral (ethylenediamine) and chiral (α-methylbenzylamine, MBA) amines, we investigated how molecular symmetry—particularly chirality—can modulate the superconducting properties of the host lattice. Ethylenediamine intercalation increased the superconducting transition temperature (Tc) from below 1 K to ~5.2 K. Notably, the intercalation of R- and S-MBA, assisted by trace ethylenediamine, led to a further Tc enhancement to ~7 K, despite the steric hindrance and reduced flexibility of MBA. Spectroscopic evidence from circular dichroism and thermal analysis confirmed the successful intercalation of optically active, chiral molecules, marking a critical step toward realizing structurally chiral superconductors.

In Chapter 5, we employed in situ synchrotron diffraction to track the evolution of hydroxide and amine intercalated TMC hybrids during solvothermal reactions. The in-situ experiments unveiled a small part of the entire picture of the hydrothermal reaction “black box,” offering the first glimpses into the hidden intermediates, structural reorganizations, and temporal evolution that govern the formation of complex molecular–solid architectures. These time-resolved experiments revealed the dynamic role of amine coordination, protonation, and symmetry reduction in directing phase selection and structural development, offering insights into how non-centrosymmetric intermediates form and stabilize under hydrothermal conditions.

In summary, this work highlights the effectiveness of molecular symmetry design—particularly through polar and chiral amines—as a tool to break spatial inversion symmetry in quantum materials. These intercalation strategies open pathways for exploring unconventional superconductivity, polar metals, and potentially topologically nontrivial states in low-symmetry hybrid systems.

## 6.2 Future Directions.

### 6.2.1 Chiral biologically relevant molecule intercalation

While this study has primarily focused on small diamines like ethylenediamine and 1,2-dap and MBA, many biologically relevant molecules offer inherent chirality, functional groups capable of hydrogen bonding or metal coordination, and may have the potential to act as both structure-directing agents and reactive ligands. This direction involves the incorporation of naturally occurring chiral molecules, such as amino acids, peptides, or alkaloids, into solvothermal and hydrothermal synthesis to construct new types of hybrid layered materials. Incorporating such molecules may not only facilitate the formation of chiral or noncentrosymmetric frameworks but could also lead to materials with novel optical, piezoelectric, or proton-conducting properties.

Amino acids in particular represent a versatile family of chiral building blocks. Their zwitterionic nature under solvothermal conditions may promote ion exchange, act as pH buffers, or stabilize metastable intermediates. Moreover, the asymmetric environment they provide could drive symmetry breaking in the growing crystal lattice, opening access to polar or even enantioselective intercalation structures. This concept aligns with recent developments in biomimetic crystallization and chirality transfer in inorganic frameworks[212, 213], where organic molecules not only template structure but influence crystallization pathways through stereochemical steering.

Future work could explore the interaction between selected amino acids and layered metal chalcogenide hosts under controlled solvothermal conditions, evaluating their role in directing layer stacking, interlayer ordering, and inducing chirality in otherwise centrosymmetric frameworks. The use of amino acid derivatives or peptide-based ligands may further enhance structural diversity and lead to tunable functionalities relevant to catalysis, sensing, or bioelectronics. In the long term, bridging the synthetic chemistry of soft templates with the structural complexity of biological molecules could unlock a new class of environmentally adaptive, molecularly engineered layered materials.

### 6.2.2 Co-intercalation

Another promising avenue for future research is the deliberate design and control of co-intercalation systems, where two or more distinct species are simultaneously incorporated into a layered host. In this study, we have observed evidence of spontaneous co-intercalation, for instance, the presence of both ethylenediamine and MBA in RMBA–$TaSe_2$ systems, and $Co(en)_3^{2+}$ complex together with *en* in en-CoS. Such coexistence, whether cooperative or competitive, can significantly affect structural symmetry, interlayer spacing, and even electronic properties.

Purposefully tuning co-intercalation conditions, such as combining an inorganic ion (e.g., $Li^+$, $NH_4^+$, $Na^+$) with a chiral or polar organic molecule—could lead to emergent structural motifs inaccessible via single-component intercalation. This may be especially powerful when the two intercalants differ in function: for example, one contributing charge (redox-active cation) and the other chirality or polarizability (e.g., amino acids, alkylamines).

And this rise to another very interesting topic. Can those co-intercalating particles react with each other? Beyond the co-insertion of multiple guest species, a compelling direction is to explore whether chemical reactions or supramolecular interactions can occur between intercalants within the confined interlayer space. While most intercalation studies treat the inserted species as non-interacting or weakly ordered, the restricted geometry and dynamic solvation environment of layered hosts can in fact promote close proximity and directional bonding between guest molecules. This opens the door to layer-confined chemical coupling, such as hydrogen bonding networks, acid–base interactions, or even covalent or coordination bond formation.

Such layer-confined reactions may occur between co-inserted amines, acids, or small organics, especially under solvothermal conditions where thermal activation and partial solvation can drive reactivity. In principle, one could imagine in situ formation of supramolecular dimers, zwitterionic pairs, or ligand–metal complexes inside the interlayer gap, effectively turning the host lattice into a 2D reaction vessel. This approach would not only influence the spacing and symmetry of the host lattice but could also generate emergent properties such as polar ordering, proton conductivity, or chiral domain formation

# Bibliography

[1] Heine, T., Transition Metal Chalcogenides: Ultrathin Inorganic Materials with Tunable Electronic Properties. *Accounts of Chemical Research* **2015,** *48* (1), 65-72.

[2] Zhou, X.; Rodriguez, E. E. Tetrahedral Transition Metal Chalcogenides as Functional Inorganic Materials. *Chem. Mater.* **2017**, *29* (13), 5737–5752.

[3] Friend, R.; Yoffe, A. Electronic properties of intercalation complexes of the transition metal dichalcogenides. Adv. Phys. 1987, 36, 1−94.

[4] Wang, Q. H.; Kalantar-Zadeh, K.; Kis, A.; Coleman, J. N.; Strano, M. S., Electronics and optoelectronics of two-dimensional transition metal dichalcogenides. *Nature Nanotechnology* **2012,** *7* (11), 699-712.

[5] Lv, R.; Robinson, J. A.; Schaak, R. E.; Sun, D.; Sun, Y.; Mallouk, T. E.; Terrones, M., Transition Metal Dichalcogenides and Beyond: Synthesis, Properties, and Applications of Single- and Few-Layer Nanosheets. *Accounts of Chemical Research* **2015,** *48* (1), 56-64.

[6] Zhou, W.; Zou, X.; Najmaei, S.; Liu, Z.; Shi, Y.; Kong, J.; Lou, J.; Ajayan, P. M.; Yakobson, B. I.; Idrobo, J.-C., Intrinsic Structural Defects in Monolayer Molybdenum Disulfide. *Nano Letters* **2013,** *13* (6), 2615-2622

[7] Srivastava, S. K.; Avasthi, B. N. Preparation, Structure and Properties of Transition Metal Trichalcogenides. *J. Mater. Sci.* **1992**, *27* (14), 3693–3705.

[8] Jung, Y.; Zhou, Y.; Cha, J. J., Intercalation in two-dimensional transition metal chalcogenides. *Inorganic Chemistry Frontiers* **2016,** *3* (4), 452-463.

[9] Mattheiss, L. F. Band structures of transition-metal-dichalcogenide layer compounds. *Phys. Rev. B* **1973**, 8, 3719−3740.

[10] Wilson, J. A.; Yoffe, A. D. Transition metal dichalcogenides: discussion and interpretation of observed optical, electrical and structural properties. *Adv. Phys.* **1969**, 18, 193−335.

[11] Di Salvo, F. J.; Schwall, R.; Geballe, T. H.; Gamble, F. R.; Osiecki, J. H. Superconductivity in layered compounds with variable interlayer spacings. *Phys. Rev. Lett.* **1971**, 27,

310−313.

[12] Gamble, F. R.; Silbernagel, B. G. Anisotropy of the proton spinlattice relaxation time in the superconducting intercalation complex $TaS_2(NH_3)$: Structural and bonding implications. *J. Chem. Phys.* **1975**, 63, 2544−2552.

[13] Murphy, D. W.; Di Salvo, F. J.; Hull, G. W.; Waszczak, J. V.; Meyer, S. F.; Stewart, G. R.; Early, S.; Acrivos, J. V.; Geballe, T. H. Properties of HxTaS2: Correlation between the superconducting $T_c$ and an electronic instability in layer compounds. *J. Chem. Phys.* **1975**, *62*.10.1063/1.430512

[14] Friend, R.; Yoffe, A. Electronic properties of intercalation complexes of the transition metal dichalcogenides. *Adv. Phys.* **1987**, 36, 1−94.

[15] Huan, G.; Greenblatt, M.; Croft, M. New ternary transitionmetal chalcogenides $AM_2X_2$ (A = K, Rb, Cs, M = Co, A = K, M = Ni, X = S, Se) - magnetically ordered metals with $ThCr_2Si_2$-Type structure. *Eur. J. Solid State Inorg. Chem.* **1989**, 26, 193−220.

[16] Oledzka, M.; Lee, J.-G.; Ramanujachary, K.; Greenblatt, M. Synthesis and characterization of quaternary sulfides with $ThCr_2Si_2$- type Structure: $KCo_{2}-xCu_xS_2$$(0.5 \leqslant x \leqslant 1.5)$ and $ACoCuS_2$($A$= K, Rb, Cs). *J. Solid State Chem.* **1996**, 127, 151−160.

[17] Oledzka, M.; Ramanujachary, K.; Greenblatt, M. Synthesis and characterization of new quaternary selenides with $ThCr_2Si_2$-type structure: $ACuMnSe_2$ (A = K, Rb, Cs). *Mater. Res. Bull.* **1998**, 33, 855−866.

[18] Klepp, K. O.; Boller, H. Ternaere Thallium-Uebergangsmetall-Chalkogenide mit ThCr2Si2-Struktur. *Monatsh. Chem.* **1978**, 109, 1049−1057.

[19] Huster, J.; Bronger, W. α-und β-BaCu2X2 (X = S, Se)− Darstellung von Einkristallen in Kaliumchalkogenocyanat-Schmelzen. Z. *Anorg. Allg. Chem.* **1999,** 625, 2033−2040.

[20] Neilson, J. R.; McQueen, T. M. Bonding, ion Mobility, and ratelimiting steps in deintercalation reactions with ThCr2Si2-type KNi2Se2. *J. Am. Chem. Soc.* **2012**, 134, 7750−7757.

[21] Rüdorff, W., Graphite Intercalation Compounds. In *Advances in Inorganic Chemistry and Radiochemistry*, Emeléus, H. J.; Sharpe, A. G., Eds. Academic Press: 1959; Vol. 1, pp 223-266.

[22] Lerf, A., Storylines in intercalation chemistry. *Dalton Transactions* **2014,** *43* (27), 10276-10291.

[23] Weber, E. Inclusion Compounds. In *Kirk-Othmer Encyclopedia of Chemical Technology*, 4th ed.; Wiley-Interscience: New York, 2000; Vol. 14.

[24] Pérez-Botella, E.; Valencia, S.; Rey, F., Zeolites in Adsorption Processes: State of the Art and Future Prospects. *Chemical Reviews* **2022,** *122* (24), 17647-17695.

[25] Soler-Illia, G. J. d. A. A.; Sanchez, C.; Lebeau, B.; Patarin, J., Chemical Strategies To Design Textured Materials: from Microporous and Mesoporous Oxides to Nanonetworks and Hierarchical Structures. *Chemical Reviews* **2002,** *102* (11), 4093-4138.

[26] Rüdorff, W. Intercalation compounds with alkali and alkaline earth metals. *Angew. Chem.* **1959**, 71, 487–491.

[27] Whittingham, M. S. Chemistry of intercalation compounds: Metal guests in chalcogenide hosts. *Prog. Solid State Chem.* **1978**, 12, 41–99.

[28] Whittingham, M. S.; Chen, R.; Chirayil, T.; Zavalij, P. The Intercalation and Hydrothermal Chemistry of Solid Electrodes. *Solid State Ionics* **1997**, *94*, 227–238.

[29] Mermut, A. R., Ed. *Layer Charge Characteristics of 2:1 Silicate Clay Minerals (CMS Workshop Lectures)*; Clay Minerals Society: Boulder, CO, 1994.

[30] Zhou, J.; Lin, Z.; Ren, H.; Duan, X.; Shakir, I.; Huang, Y.; Duan, X. Layered Intercalation Materials. *Adv. Mater.* **2021**, *33* (25), 2004557.

[31] Parvez, K.; Wu, Z.-S.; Li, R.; Liu, X.; Graf, R.; Feng, X.; Müllen, K. Exfoliation of Graphite into Graphene in Aqueous Solutions of Inorganic Salts. *J. Am. Chem. Soc.* **2014**, *136* (16), 6083–6091.

[32] Su, C.-Y.; Lu, A.-Y.; Xu, Y.; Chen, F.-R.; Khlobystov, A. N.; Li, L.-J. High-Quality Thin Graphene Films from Fast Electrochemical Exfoliation. *ACS Nano* **2011**, *5* (3), 2332–2339.

[33] You, X.; Liu, N.; Lee, C. J.; Pak, J. J. Electrochemical Exfoliation of $MoS_2$ with High Yield. *Mater. Lett.* **2014**, *121*, 31–33.

[34] Abdelkader, A. M.; Cooper, A. J.; Dryfe, R. A. W.; Kinloch, I. A. How to Get Between the Sheets: A Review of Recent Works on the Electrochemical Exfoliation of Graphene Materials from Bulk Graphite. *Nanoscale* **2015**, *7* (16), 6944–6956.

[35] Wagner, M. R.; Albering, J. H.; Moeller, K. C.; Besenhard, J. O.; Winter, M. Electrochemical and Chemical Lithium Insertion into $MoS_2$ and Co-Intercalation of Solvents. *Electrochem. Commun.* **2005**, *7* (9), 947–952.

[36] Bao, W.; Wan, J.; Han, X.; Cai, X.; Zhu, H.; Kim, D.; Ma, D.; Xu, Y.; Munday, J. N.; Drew, H. D.; Fuhrer, M. S.; Hu, L. Approaching the Limits of Transparency and Conductivity in Graphitic Materials through Lithium Intercalation. *Nat. Commun.* **2014**, *5*, 4224.

[37] Yazdani, S.; Yarali, M.; Cha, J. J. Electronic Structure Engineering of 2D Transition Metal Dichalcogenide Alloys through Controlled Anion Intercalation. *Nano Res.* **2019**, *12* (9), 2126–2132.

[38] Xu, M.; Sun, H.; Shen, C.; Yang, S.; Que, W.; Zhang, Y.; Song, X. A Facile Electrochemical Approach to Fabricate Few-Layer $MoS_2$ Nanosheets with High Catalytic Activity for Hydrogen Evolution Reaction. *Nano Res.* **2015**, *8* (3), 801–812.

[39] Zeng, Z.; Yin, Z.; Huang, X.; Li, H.; He, Q.; Lu, G.; Boey, F.; Zhang, H. Single-Layer Semiconducting Nanosheets: High-Yield Preparation and Device Fabrication. *Angew. Chem., Int. Ed.* **2011**, *50* (47), 11093–11097.

[40] Dresselhaus, M. S.; Dresselhaus, G. Intercalation Compounds of Graphite. *Adv. Phys.* **2002**, *51*, 1–186.

[41] Falardeau, E. R.; Hanlon, L. R.; Thompson, T. E. The Preparation and Characterization of Graphite Intercalation Compounds of Arsenic Pentafluoride. *Inorg. Chem.* **1978**, *17*, 301–304.

[42] Jung, N.; Kim, B.; Crowther, A. C.; Kim, N.; Nuckolls, C.; Brus, L. Doping Graphene via the Proximity of Aromatic Molecules. *ACS Nano* **2011**, *5*, 5708–5716.

[43] Ohuchi, F. S.; Jaegermann, W.; Pettenkofer, C.; Parkinson, B. A. Surface Photovoltage and Photoemission Studies of the Electronic Structure of $WS_2$. *Langmuir* **1989**, *5*, 439–444.

[44] Bronold, M.; Pettenkofer, C.; Jaegermann, W. Surface and Interface Properties of $SnS_2$ and

Related Compounds. *Appl. Phys. A* **1991**, *52*, 171–178.

[45] Pronin, I. I.; Gomoyunova, M. V.; Faradzhev, N. S.; Valdaitsev, D. A.; Starnberg, H. I. Alkali Metal Intercalation in $VSe_2$ Investigated by Photoelectron Spectroscopy. *Surf. Sci.* **2000**, *461*, 137–146.

[46] Starnberg, H. I.; Hughes, H. P. Alkali Metal Intercalation in $TiS_2$ Studied by Ultraviolet Photoemission. *J. Phys. C: Solid State Phys.* **1987**, *20*, 4429–4441.

[47] Jung, N.; Kim, N.; Jockusch, S.; Turro, N. J.; Kim, P.; Brus, L. Charge Transfer Chemical Doping of Few Layer Graphenes: Charge Distribution and Band Gap Formation. *Nano Lett.* **2009**, *9*, 4133–4137.

[48] Nixon, D. E.; Parry, G. S. Graphite Intercalation Compounds—II: Preparation of Compounds Using Alkali Metals and Alkaline Earths. *J. Phys. D: Appl. Phys.* **1968**, *1*, 291–299.

[49] Dimiev, A. M.; Bachilo, S. M.; Saito, R.; Tour, J. M. Chemical Formation of Graphene Oxide Films on the Carbon Nanotube Surface. *ACS Nano* **2012**, *6*, 7842–7849.

[50] Seiler, S.; Halbig, C. E.; Grote, F.; Rietsch, P.; Börrnert, F.; Kaiser, U.; Meyer, B.; Eigler, S. π–π Stacking Interactions as Stabilizing Forces for Functionalized Graphene Sheets. *Nat. Commun.* **2018**, *9*, 836.

[51] Gamble, F. R.; Osiecki, J. H.; DiSalvo, F. J. Intercalation Complexes of Lewis Bases and Layered Sulfides: A New Class of Inorganic-Organic Solids. *J. Chem. Phys.* **1971**, *55*, 3525–3533.

[52] Ehrenfreund, E.; Gossard, A. C.; Gamble, F. R. Magnetic and Transport Properties of Layered Transition-Metal Dichalcogenides Intercalated with Organic Molecules. *Phys. Rev. B* **1972**, *5*, 1708–1716.

[53] Dines, M. B. Lithium Intercalation via n-Butyllithium of Layered Transition-Metal Dichalcogenides. *Inorg. Chem.* **1978**, *17*, 762–775.

[54] Tsai, H.-L.; Heising, J.; Schindler, J. L.; Kannewurf, C. R.; Kanatzidis, M. G. Exfoliated and Restacked $MoS_2$ and $WS_2$: Ionic Conductivity and Structural Characterization. *Chem. Mater.* **1997**, *9*, 879–882.

[55] Fan, X.; Xu, P.; Li, Y. C.; Zhou, D.; Sun, Y.; Nguyen, M. A. T.; Terrones, M.; Mallouk, T.

E. Controlled Exfoliation of $MoS_2$ Crystals into Trilayer Nanosheets. *J. Am. Chem. Soc.* **2016**, *138*, 5143–5149.

[56] Koski, K. J.; Wessells, C. D.; Reed, B. W.; Cha, J. J.; Kong, D.; Cui, Y. Chemical Intercalation of Zero-Valent Metals into 2D Layered $Bi_2Se_3$ Nanoribbons. *J. Am. Chem. Soc.* **2012**, *134*, 13773–13779.

[57] L. Pauling, *The Nature of the Chemical Bond*. Ithaca, New York: Cornell University Press, 3 ed., 1960.

[58] F. H. Allen, C. M. Bird, R. S. Rowland, and P. R. Raithby, "Resonance-Induced Hydrogen Bonding at Sulfur Acceptors in $R_1R_2C{=}S$ and $R_1CS_2^-$ Systems," *Acta Crystallographica Section B,* vol. 53, pp. 680-695, Aug 1997.

[59] G. R. Desiraju and T. Steiner, *The Weak Hydrogen Bond. International Union of Crystallography, New York, U.S.A.*: Oxford Science Publications, 1999.

[60] F. H. Allen, C. M. Bird, R. S. Rowland, and P. R. Raithby, \Hydrogen-Bond Acceptor and Donor Properties of Divalent Sulfur (*Y-S-Z* and *R-S-H*)," *Acta Crystallographica Section B*, vol. 53, pp. 696-701, Aug 1997.

[61] Arunan, E.; Desiraju, G. R.; Klein, R. A.; Sadlej, J.; Scheiner, S.; Alkorta, I.; Clary, D. C.; Crabtree, R. H.; Dannenberg, J. J.; Hobza, P.; Kjaergaard, H. G.; Legon, A. C.; Mennucci, B.; Nesbitt, D. J. Defining the Hydrogen Bond: An Account. *Pure Appl. Chem.* **2011**, *83*, 1619–1636.

[62] Huggins, M. L., The Hydrogen Bond (Pimentel, George C.; McClellan, Aubrey L.). *Journal of Chemical Education* **1960,** *37* (11), A754.

[63] Zhou, X.; Borg, C. K. H.; Lynn, J. W.; Saha, S. R.; Paglione, J.; Rodriguez, E. E., The preparation and phase diagrams of $(Li_{1-x}Fe_xOD)FeSe$ and $(Li_{1-x}Fe_xOH)FeSe$ superconductors. *Journal of Materials Chemistry C* **2016,** *4* (18), 3934-3941.

[64] Vivanco, H. K.; Rodriguez, E. E., The intercalation chemistry of layered iron chalcogenide superconductors. *Journal of Solid State Chemistry* **2016,** *242*, 3-21.

[65] Zhou, X.; Eckberg, C.; Wilfong, B.; Liou, S.-C.; Vivanco, H. K.; Paglione, J.; Rodriguez, E. E. Superconductivity and Magnetism in Iron Sulfides Intercalated by Metal Hydroxides. *Chemical science* **2017**, *8* (5), 3781--3788.

[66] Zhou, X.; Wilfong, B.; Liou, S.-C.; Hodovanets, H.; Brown, C. M.; Rodriguez, E. E., Proton and ammonia intercalation into layered iron chalcogenides. *Chemical Communications* **2018,** *54* (50), 6895-6898.

[67] Murchison, R. Remarks on Mineral Crystallization in the 1840s; cited by Somiya, S.

[68] Bunsen, R. Observations on Crystal Growth in 1839; cited in: Laudise, R. A. *The Growth of Single Crystals*; Prentice-Hall: Englewood Cliffs, NJ, 1970; pp 278–281.

[69] Schafthaul, K. F. E. Ueber Gelehrte Anzeigen. *Bayer. Akad.* **1845**, *20* (557), 569, 575, 592.

[70] Tarasov, V. G.; Gebruk, A. V.; Mironov, A. N.; Moskalev, L. I. Deep-Sea and Shallow-Water Hydrothermal Vent Communities: Two Different Phenomena? *Chem. Geol.* **2005**, *224*, 5–39.

[71] NOAA Pacific Marine Environmental Laboratory. Multimedia Resources. https://www.pmel.noaa.gov/eoi/multimedia.htfml (accessed May 12, 2025).

[72] Morey, G. W.; Niggli, P. The Hydrothermal Formation of Silicates, a Review. *J. Am. Chem. Soc.* **1913**, *35*, 1086–1130.

[73] Laudise, R. A. *The Growth of Single Crystals*; Prentice-Hall: Englewood Cliffs, NJ, 1970; pp 278–281.

[74] Rabenau, A. The Role of Hydrothermal Synthesis in Preparative Chemistry. *Angew. Chem., Int. Ed. Engl.* **1985**, *24*, 1026–1040.

[75] Lobachev, A. N., Ed. *Crystallization Processes under Hydrothermal Conditions*; Consultants Bureau: New York, NY, 1973.

[76] Roy, R. Acceleration the Kinetics of Low-Temperature Inorganic Syntheses. *J. Solid State Chem.* **1994**, *111*, 11–17.

[77] Byrappa, K., Ed. *Hydrothermal Growth of Crystals*; Pergamon Press: Oxford, UK, 1992.

[78] Yoshimura, M.; Suda, H. Hydrothermal Processing of Hydroxyapatite: Past, Present, and Future. In *Hydroxyapatite and Related Materials*; Brown, P. W., Constanz, B., Eds.; CRC Press: Boca Raton, FL, 1994; pp 45–72.

[79] Byrappa, K.; Yoshimura, M. *Handbook of Hydrothermal Technology: A Technology for Crystal Growth and Materials Processing*; William Andrew Publishing: Norwich, NY, 2001.

[80] Byrappa, K**.** Novel Hydrothermal Solution Routes of Advanced High Melting Nanomaterials Processing. *J. Ceram. Soc. Jpn.* **2009**, *117*, 236–244.

[81] Yoshimura, M.; Byrappa, K. Hydrothermal Processing of Materials: Past, Present and Future. *J. Mater. Sci.* **2008**, *43*, 2085–2103.

[82] Litvin, B. N.; Tules, D. A. Apparatus for Hydrothermal Synthesis and Growth of Single Crystals. In *Hydrothermal Synthesis of Crystals*; Nauka: Moscow, 1968

[83] Parr Instrument Company. Acid Digestion. https://www.parrinst.com/products/sample-preparation/acid-digestion/ (accessed May 12, 2025).

[84] Laudise, R. A.; Nielsen, J. W. Hydrothermal Crystal Growth. In *Solid State Physics*; Seitz, F., Turnbull, D., Eds.; Academic Press: New York, NY, 1961; Vol. 12.

[85] Wilfong, B.; Zhou, X.; Rodriguez, E. E. Hydrothermal Synthesis and Crystal Growth. In *Fundamentals of Quantum Materials: A Practical Guide to Synthesis and Exploration*; Paglione, J., Butch, N. P., Rodriguez, E. E., Eds.; World Scientific: New Jersey, 2021; pp 99–136.

[86] Zhou, X.; Wilfong, B.; Vivanco, H.; Paglione, J.; Brown, C. M.; Rodriguez, E. E., Metastable Layered Cobalt Chalcogenides from Topochemical Deintercalation. *Journal of the American Chemical Society* **2016,** *138* (50), 16432-16442.

[87] Pecharsky, V. K.; Zavalij, P. Y. *Fundamentals of Powder Diffraction and Structural Characterization of Materials*, 2nd ed.; Springer: New York, 2009.

[88] Bacon, G. E.; Lonsdale, K. Neutron Diffraction. *Rep. Prog. Phys.* **1953**, *16*, 1–58.

[89] McKeehan, L. The Measurement of Magnetic Quantities. *J. Opt. Soc. Am.* **1929**, *19*, 213–242.

[90] Kapitza, P. L.; Webster, W. A Method of Measuring Magnetic Susceptibilities. *Proc. R. Soc. London, Ser. A* **1931**, *132*, 442–459.

[91] Morris, B. L.; Wold, A. Faraday Balance for Measuring Magnetic Susceptibility. *Rev.*

*Sci. Instrum.* **1968**, *39*, 1937–1941.

[92] Mugiraneza, S.; Hallas, A. M. Tutorial: A Beginner's Guide to Interpreting Magnetic Susceptibility Data with the Curie–Weiss Law. *Commun. Phys.* **2022**, *5*, 95.

[93] Zhou, W. X.; Ariando, A. Review on Ferroelectric/Polar Metals. *Jpn J Appl Phys* **2020**, *59* (SI), SI0802.

[94] Anderson, P. W.; Blount, E. I. Symmetry Considerations on Martensitic Transformations: "Ferroelectric" Metals? *Phys Rev Lett* **1965**, *14* (7), 217–219.

[95] Bauer, E.; Sigrist, M., *Non-centrosymmetric superconductors: introduction and overview*. Springer Science & Business Media: 2012; Vol. 847.

[96] Puggioni, D.; Stroppa, A.; Rondinelli, J. M. Design of a Polar Half-Metallic Ferromagnet with Accessible and Enhanced Electric Polarization. *Phys Rev Mater* **2018**, *2* (11), 114403.

[97] Puggioni, D.; Giovannetti, G.; Capone, M.; Rondinelli, J. M. Design of a Mott Multiferroic from a Nonmagnetic Polar Metal. *Phys Rev Lett* **2015**, *115* (8), 087202.

[98] Kim, T. H.; Puggioni, D.; Yuan, Y.; Xie, L.; Zhou, H.; Campbell, N.; Ryan, P. J.; Choi, Y.; Kim, J.-W.; Patzner, J. R.; Ryu, S.; Podkaminer, J. P.; Irwin, J.; Ma, Y.; Fennie, C. J.; Rzchowski, M. S.; Pan, X. Q.; Gopalan, V.; Rondinelli, J. M.; Eom, C. B. Polar Metals by Geometric Design. *Nature* **2016**, *533* (7601), 68–72.

[99] Laurita, N. J.; Ron, A.; Shan, J.-Y.; Puggioni, D.; Koocher, N. Z.; Yamaura, K.; Shi, Y.; Rondinelli, J. M.; Hsieh, D. Evidence for the Weakly Coupled Electron Mechanism in an Anderson-Blount Polar Metal. *Nat Commun* **2019**, *10* (1), 3217.

[100] Shi, Y.; Guo, Y.; Wang, X.; Princep, A. J.; Khalyavin, D.; Manuel, P.; Michiue, Y.; Sato, A.; Tsuda, K.; Yu, S.; Arai, M.; Shirako, Y.; Akaogi, M.; Wang, N.; Yamaura, K.; Boothroyd, A. T. A Ferroelectric-like Structural Transition in a Metal. *Nat Mater* **2013**, *12* (11), 1024–1027.

[101] Puggioni, D.; Rondinelli, J. M. Designing a Robustly Metallic Noncenstrosymmetric Ruthenate Oxide with Large Thermopower Anisotropy. *Nat Commun* **2014**, *5* (1), 3432.

[102] Peng, Y.; Bie, J.; Liu, X.; Li, L.; Chen, S.; Fa, W.; Wang, S.; Sun, Z.; Luo, J. Acquiring High-$T_c$ Layered Metal Halide Ferroelectrics via Cage-Confined Ethylamine Rotators. *Angewandte Chemie Int Ed* **2020**.

[103] Ji, C.; Dey, D.; Peng, Y.; Liu, X.; Li, L.; Luo, J. Ferroelectricity-Driven Self-Powered Ultraviolet Photodetection with Strong Polarization Sensitivity in a Two-Dimensional Halide Hybrid Perovskite. *Angewandte Chemie Int Ed* **2020**, *59* (43), 18933–18937.

[104] Zhang, H.-Y.; Song, X.-J.; Chen, X.-G.; Zhang, Z.-X.; You, Y.-M.; Tang, Y.-Y.; Xiong, R.-G. Observation of Vortex Domains in a Two-Dimensional Lead Iodide Perovskite Ferroelectric. *J Am Chem Soc* **2020**, *142* (10), 4925–4931.

[105] Xu, X.; Xiao, L.; Zhao, J.; Pan, B.; Li, J.; Liao, W.; Xiong, R.; Zou, G. Molecular Ferroelectrics-Driven High-Performance Perovskite Solar Cells. *Angewandte Chemie Int Ed* **2020**, *59* (45), 19974–19982.

[106] Shi, C.; Ma, J.-J.; Jiang, J.-Y.; Hua, M.-M.; Xu, Q.; Yu, H.; Zhang, Y.; Ye, H.-Y. Large Piezoelectric Response in Hybrid Rare-Earth Double Perovskite Relaxor Ferroelectrics. *J Am Chem Soc* **2020**, *142* (21), 9634–9641.

[107] Shi, C.; Ye, L.; Gong, Z.-X.; Ma, J.-J.; Wang, Q.-W.; Jiang, J.-Y.; Hua, M.-M.; Wang, C.-F.; Yu, H.; Zhang, Y.; Ye, H.-Y. Two-Dimensional Organic–Inorganic Hybrid Rare-Earth Double Perovskite Ferroelectrics. *J Am Chem Soc* **2019**, *142* (1), 545–551.

[108] Lu, H.; Xiao, C.; Song, R.; Li, T.; Maughan, A. E.; Levin, A.; Brunecky, R.; Berry, J. J.; Mitzi, D. B.; Blum, V.; Beard, M. C. Highly Distorted Chiral Two-Dimensional Tin Iodide Perovskites for Spin Polarized Charge Transport. *J Am Chem Soc* **2020**, *142* (30), 13030–13040.

[109] Park, I.-H.; Kwon, K. C.; Zhu, Z.; Wu, X.; Li, R.; Xu, Q.-H.; Loh, K. P. Self-Powered Photodetector Using Two-Dimensional Ferroelectric Dion–Jacobson Hybrid Perovskites. *J Am Chem Soc* **2020**, *142* (43), 18592–18598.

[110] Zhou, X.; Wang, L.; Fan, X.; Wilfong, B.; Liou, S.-C.; Wang, Y.; Zheng, H.; Feng, Z.; Wang, C.; Rodriguez, E. E. Isotope Effect between $H_2O$ and $D_2O$ in Hydrothermal Synthesis. *Chem Mater* **2020**, *32* (2), 769–775.

[111] Borg, C. K. H.; Zhou, X.; Eckberg, C.; Campbell, D. J.; Saha, S. R.; Paglione, J.; Rodriguez, E. E. Strong Anisotropy in Nearly Ideal Tetrahedral Superconducting FeS Single Crystals. *Physical Review B* **2016**, *93*, 094522.

[112] Sedlmaier, S. J.; Cassidy, S. J.; Morris, R. G.; Drakopoulos, M.; Reinhard, C.; Moorhouse, S. J.; O’Hare, D.; Manuel, P.; Khalyavin, D.; Clarke, S. J. Ammonia-Rich High-Temperature Superconducting Intercalates of Iron Selenide Revealed through

Time-Resolved *in Situ* X-Ray and Neutron Diffraction. *Journal of the American Chemical Society* **2014**, *136* (2), 630--633.

[113] Huan, G.; Greenblatt, M.; Croft, M. New Ternary Transition Metal Chalcogenides $AM_2X_2$ ($A$= K, Rb, Cs; $M$= Co; $A$= K, $M$= Ni; $X$= S, Se): Magnetically Ordered Metals with the $ThCr_2Si_2$-Type Structure. *European journal of solid state and inorganic chemistry* **1989**, *26* (2), 193--220.

[114] Neilson, J. R.; McQueen, T. M. Bonding, Ion Mobility, and Rate-Limiting Steps in Deintercalation Reactions with $ThCr_2Si_2$-Type $KNi_2Se_2$. *Journal of the American Chemical Society* **2012**, *134* (18), 7750–7757.

[115] Whittingham, M. S. Chemistry of Intercalation Compounds: Metal Guests in Chalcogenide Hosts. *Prog Solid State Ch* **1978**, *12* (1), 41–99.

[116] Lewis, K. G.; Ghosh, S. K.; Bhuvanesh, N.; Gladysz, J. A. Cobalt(III) Werner Complexes with 1,2-Diphenylethylenediamine Ligands: Readily Available, Inexpensive, and Modular Chiral Hydrogen Bond Donor Catalysts for Enantioselective Organic Synthesis. *Acs Central Sci* **2015**, *1* (1), 50–56.

[117] Ehnbom, A.; Ghosh, S. K.; Lewis, K. G.; Gladysz, J. A. Octahedral Werner Complexes with Substituted Ethylenediamine Ligands: A Stereochemical Primer for a Historic Series of Compounds Now Emerging as a Modern Family of Catalysts. *Chem Soc Rev* **2016**, *45* (24), 6799–6811.

[118] Ghosh, S. K.; Ganzmann, C.; Bhuvanesh, N.; Gladysz, J. A. Werner Complexes with $\omega$-Dimethylaminoalkyl Substituted Ethylenediamine Ligands: Bifunctional Hydrogen-Bond-Donor Catalysts for Highly Enantioselective Michael Additions. *Angewandte Chemie Int Ed* **2016**, *55* (13), 4356–4360.

[119] Valasek, J. Piezo-Electric and Allied Phenomena in Rochelle Salt. *Phys Rev* **1921**, *17* (4), 475–481.

[120] Horiuchi, S.; Tokura, Y. Organic Ferroelectrics. *Nat Mater* **2008**, *7* (5), 357–366.

[121] Sheldrick, G. M. Crystallographic Shelves: Space-Group Hierarchy Explained. *Acta Cryst. A* **2015**, *71*, 3--8.

[122] Kresse, G. Efficient Iterative Schemes for Ab Initio Total-Energy Calculations Using a Plane-Wave Basis Set. *Phys Rev B* **1996**, *54* (16), 11169–11186.

[123] Kresse, G.; Joubert, D. From Ultrasoft Pseudopotentials to the Projector Augmented-Wave Method. *Phys Rev B* **1998**, *59* (3), 1758–1775.

[124] Perdew, J. P.; Ruzsinszky, A.; Csonka, G. I.; Vydrov, O. A.; Scuseria, G. E.; Constantin, L. A.; Zhou, X.; Burke, K. Restoring the Density-Gradient Expansion for Exchange in Solids and Surfaces. *Phys Rev Lett* **2008**, *100* (13), 136406.

[125] Blöchl, P. E. Projector Augmented-Wave Method. *Phys Rev B* **1994**, *50* (24), 17953–17979.

[126] Brown, I. D. Recent Developments in the Methods and Applications of the Bond Valence Model. *Chem Rev* **2009**, *109* (12), 6858–6919.

[127] Cooke, K.; Olenev, A. V.; Kovnir, K. Tris(ethylenediamine)cobalt(II) Dichloride. *Acta Crystallogr Sect E Struct Reports Online* **2013**, *69* (6), m332–m332.

[128] Halasyamani, P. S.; Poeppelmeier, K. R. Noncentrosymmetric Oxides. *Chem Mater* **1998**, *10* (10), 2753–2769.

[129] Huan, G.; Greenblatt, M. Antiferromagnetic-to-Ferromagnetic Transition in Metallic $Tl_{1-x}K_xCo_2Se_2$ ($0 \leqslant x \leqslant 1.0$) with $ThCr_2Si_2$-Type Structure. *J Less Common Metals* **1989**, *156* (1–2), 247–257.

[130] Wilfong, B.; Zhou, X.; Vivanco, H.; Campbell, D. J.; Wang, K.; Graf, D.; Paglione, J.; Rodriguez, E. Frustrated Magnetism in the Tetragonal CoSe Analog of Superconducting FeSe. *Physical Review B* **2018**, *97* (10), 104408.

[131] Desiraju, G. R.; Steiner, T. *The Weak Hydrogen Bond*; International Union of Crystallography; Oxford Science Publications: New York, U.S.A., 1999.

[132] Goldsmith, G. J.; White, J. G. Ferroelectric Behavior of Thiourea. *J Chem Phys* **1959**, *31* (5), 1175–1187.

[133] Allen, F. H.; Bird, C. M.; Rowland, R. S.; Raithby, P. R. Hydrogen-Bond Acceptor and Donor Properties of Divalent Sulfur ( *Y-S-Z* and *R-S-H*). *Acta Crystallogr Sect B Struct Sci* **1997**, *53* (4), 696--701.

[134] Schaefer, M.; Stähler, R.; Kiebach, W.; Näther, C.; Bensch, W. Four New Thioantimonates(III) with the General Formula [*TM*(tren)]$Sb_4S_7$ (*TM* = Mn, Fe, Co, Zn) with the Transition Metal as Part of a Thioantimonate(III) Network Synthesized under

Solvothermal Conditions and Tuning of the Optical Band Gap by the Transition Metal Cation. *Zeitschrift Für Anorganische Und Allgemeine Chemie* **2004**, *630* (12), 1816–1822.

[135] Behrens, M.; Scherb, S.; Näther, C.; Bensch, W. On the Incorporation of Transition Metal Atoms into Thiostannates: Synthesis, Crystal Structures and Spectroscopic Properties of $[Ni(en)_3]_2Sn_2S_6$, $[Ni(dap)_3]_2Sn_2S_6 \cdot 2H_2O$, $[Co(tren)]_2Sn_2S_6$, and $[Ni(tren)]_2Sn_2S_6$. *Zeitschrift Für Anorganische Und Allgemeine Chemie* **2003**, *629* (7-8), 1367–1373.

[136] Schaefer, M.; Engelke, L.; Bensch, W. Solvothermal Synthesis and Crystal Structures of Two Thioantimonate(V) Compounds with the $[SbS_4]^{3-}$ Anion Acting as a Monodentate Ligand: $[Mn(C_6H_{18}N_4)(C_6H_{19}N_4)]SbS_4$ and $[Mn(C_6H_{14}N_2)_3]_2[Mn(C_6H_{14}N_2)_2(SbS_4)_2]\cdot 6H_2O$. *Zeitschrift Für Anorganische Und Allgemeine Chemie* **2003**, *629* (11), 1912–1918.

[137] Jia, D.; Zhao, Q.; Dai, J.; Zhang, Y.; Zhu, Q. New Chalcogenidoarsenates with Transition Metal Complex Cations: $[M(en)_3]_2As_2S_5$ ($M$ = Mn, Ni) and $[Mn(en)_3]_2As_2Se_5$. *Zeitschrift Für Anorganische Und Allgemeine Chemie* **2006**, *632* (2), 349–353.

[138] Zhou, J.; Zhang, Y.; Bian, G.-Q.; Zhu, Q.-Y.; Li, C.-Y.; Dai, J. Solvothermal Synthesis of a Series of Telluridoindate Compounds Displaying Three Types of One-Dimensional Polymeric Anion Chains with the Formula $\{[InTe_2]^-\}_\infty$. *Cryst Growth Des* **2007**, *7* (9), 1889–1892.

[139] Zhou, J.; Dai, J.; Bian, G.-Q.; Li, C.-Y. Solvothermal Synthesis of Group 13–15 Chalcogenidometalates with Chelating Organic Amines. *Coordin Chem Rev* **2009**, *253* (9–10), 1221–1247.

[140] Zhou, J.; Bian, G.; Zhang, Y.; Dai, J.; Cheng, N. Solvothermal Synthesis of Two 2-D Thioantimonates(III) with Metal Complexes as Template Ions, $[M(dap)_3]Sb_4S_7$ ($M = Ni^{2+}$ and $Co^{2+}$). *Zeitschrift Für Anorganische Und Allgemeine Chemie* **2007**, *633* (15), 2701–2705.

[141] Zhou, J.; Zhang, Y.; Bian, G.-Q.; Li, C.-Y.; Chen, X.-X.; Dai, J. Structural Study of Organic−Inorganic Hybrid Thiogallates and Selenidogallates in View of Effects of the Chelate Amines. *Cryst Growth Des* **2008**, *8* (7), 2235–2240.

[142] Harmer, C. P.; Pak, C.; Greenfield, J. T.; Adeyemi, A. N.; Gamage, E. H.; Kovnir, K. Non-Innocent Intercalation of Diamines into Tetragonal FeS Superconductor. *Acs Appl Energy Mater* **2021**, *4* (1), 42–46.

[143] Spaldin, N. A. A Beginner's Guide to the Modern Theory of Polarization. *J Solid State Chem* **2012**, *195*, 2–10.

[144] Resta, R.; Vanderbilt, D. *Physics of Ferroelectrics, A Modern Perspective*; Springer, 2007.

[145] Gnewuch, S.; Rodriguez, E. E. The Fourth Ferroic Order: Current Status on Ferrotoroidic Materials. *J Solid State Chem* **2019**, *271*, 175–190.

[146] Fiebig, M.; Lottermoser, T.; Meier, D.; Trassin, M. The Evolution of Multiferroics. *Nat Rev Mater* **2016**, *1* (8), 16046.

[147] Eerenstein, W.; Mathur, N. D.; Scott, J. F. Multiferroic and Magnetoelectric Materials. *Nature* **2006**, *442* (7104), 759–765.

[148] Benedek, N. A.; Birol, T. 'Ferroelectric' Metals Reexamined: Fundamental Mechanisms and Design Considerations for New Materials. *J Mater Chem C* **2016**, *4* (18), 4000–4015.

[149] Wang, Y.; Liu, X.; Burton, J. D.; Jaswal, S. S.; Tsymbal, E. Y. Ferroelectric Instability Under Screened Coulomb Interactions. *Phys Rev Lett* **2012**, *109* (24), 247601.

[150] Kolodiazhnyi, T.; Tachibana, M.; Kawaji, H.; Hwang, J.; Takayama-Muromachi, E. Persistence of Ferroelectricity in $BaTiO_3$ through the Insulator-Metal Transition. *Phys Rev Lett* **2010**, *104* (14), 147602.

[151] Liu, H. M.; Du, Y. P.; Xie, Y. L.; Liu, J.-M.; Duan, C.-G.; Wan, X. Metallic Ferroelectricity Induced by Anisotropic Unscreened Coulomb Interaction in LiOsO3. *Phys Rev B* **2015**, *91* (6), 064104.

[152] Fei, Z.; Zhao, W.; Palomaki, T. A.; Sun, B.; Miller, M. K.; Zhao, Z.; Yan, J.; Xu, X.; Cobden, D. H. Ferroelectric Switching of a Two-Dimensional Metal. *Nature* **2018**, *560* (7718), 336–339.

[153] Sharma, P.; Xiang, F.-X.; Shao, D.-F.; Zhang, D.; Tsymbal, E. Y.; Hamilton, A. R.; Seidel, J. A Room-Temperature Ferroelectric Semimetal. *Sci Adv* **2019**, *5* (7), eaax5080.

[154] Oledzka, M.; Lee, J.-G.; Ramanujachary, K. V.; Greenblatt, M. Synthesis and Characterization of Quaternary Sulfides with $ThCr_2Si_2$-Type Structure: $KCo_{2-x}Cu_xS_2$(0.5 $\leq x \leq$ 1.5) And $A$CoCu$S_2$($A$= K, Rb, Cs). *J Solid State Chem* **1996**, *127* (2), 151–160.

[155] Oledzka, M.; Ramanujachary, K. V.; Greenblatt, M. Physical Properties of Quaternary Mixed Transition Metal Sufides: $A$CuFe$_2$ ($A$ = K, Rb, Cs). *Materials Research Bulletin* **1996**, *31*, 1491–1499.

[156] Newmark, A. R.; Huan, G.; Greenblatt, M.; Croft, M. Magnetic Ordering in $TlCo_{2-x}Ni_xSe_2$ with the $ThCr_2Si_2$ Structure. *Solid State Commun* **1989**, *71* (11), 1025–1032.

[157] Huan, G.; Greenblatt, M.; Ramanujachary, K. V. Magnetic Ordering in Metallic $TlCo_{2-x}Ni_xS_2$ ($0 \leqslant x \leqslant 2.0$) with the $ThCr_2Si_2$ Structure. *Solid State Commun* **1989**, *71* (3), 221–228.

[158] Greaney, M.; Huan, G.; Ramanujachary, K. V.; Teweldemedhin, Z.; Greenblatt, M. Antiferro-to-Ferromagnetic Transition in Metallic $TlCo_2S_xSe_{2-x}$ ($0 \leqslant x \leqslant 2.0$) with the $ThCr_2Si_2$ Type Structure. *Solid State Commun* **1991**, *79* (10), 803–810.

[159] Guo, Z.; Zhang, H.; Wang, D.; Han, B.; Jin, S.; Yuan, W. Ferromagnetic Interlayer Interaction in $KCo_2Se_{2-x}S_x$($0 \leq x \leq 2$) and Its Chemical Origin. *Dalton T* **2016**, *45* (19), 8248–8252.

[160] Ronneteg, S.; Lumey, M.-W.; Dronskowski, R.; Gelius, U.; Berger, R.; Felton, S.; Nordblad, P. Magnetic and Electronic Structure of $TlCo_2S_2$. *J Solid State Chem* **2004**, *177* (9), 2977–2984.

[161] Tan, X.; Yaroslavtsev, A. A.; Cao, H.; Geondzhian, A. Y.; Menushenkov, A. P.; Chernikov, R. V.; Nataf, L.; Garlea, V. O.; Shatruk, M. Controlling Magnetic Ordering in $Ca_{1-x}Eu_xCo_2As_2$ by Chemical Compression. *Chem Mater* **2016**, *28* (20), 7459–7469.

[162] Tan, X.; Fabbris, G.; Haskel, D.; Yaroslavtsev, A. A.; Cao, H.; Thompson, C. M.; Kovnir, K.; Menushenkov, A. P.; Chernikov, R. V.; Garlea, V. O.; Shatruk, M. A Transition from Localized to Strongly Correlated Electron Behavior and Mixed Valence Driven by Physical or Chemical Pressure in $A$Co$_2$As$_2$ ($A$ = Eu and Ca). *J Am Chem Soc* **2016**, *138* (8), 2724–2731.

[163] Yang, J.; Chen, B.; Wang, H.; Mao, Q.; Imai, M.; Yoshimura, K.; Fang, M. Magnetic Properties in Layered $A$Co$_2$Se$_2$ ($A$ = K, Rb, Cs) with the $ThCr_2Si_2$-Type Structure. *Phys Rev B* **2013**, *88* (6), 064406.

[164] Gamage, E. H.; Greenfield, J. T.; Unger, C.; Kamali, S.; Clark, J. K.; Harmer, C. P.; Luo, L.; Wang, J.; Shatruk, M.; Kovnir, K. Tuning Fe–Se Tetrahedral Frameworks by a Combination of $[Fe(en)_3]^{2+}$ Cations and $Cl^-$ Anions. *Inorg Chem* **2020**.

[165] Stahl, J.; Shlaen, E.; Singer, H.; Johrendt, D. Systematic Dimensional Reduction of the Layered $\beta$-FeSe Structure by Solvothermal Synthesis. *Dalton Transactions* **2018**, *47* (10), 3264--3271.

[166] Ok, K. M.; Chi, E. O.; Halasyamani, P. S. Bulk Characterization Methods for Non-Centrosymmetric Materials: Second-Harmonic Generation, Piezoelectricity, Pyroelectricity, and Ferroelectricity. *Chem Soc Rev* **2006**, *35* (8), 710–717.

[167] Zhou, X.; Borg, C. K. H.; Lynn, J. W.; Saha, S. R.; Paglione, J.; Rodriguez, E. E. The Preparation and Phase Diagrams of ($^7Li_{1-x}Fe_xOD$)FeSe and ($Li_{1-x}Fe_xOH$)FeSe Superconductors. *Journal of Materials Chemistry C* **2016**, *4*, 3934–3941.

[168] Dong, X.; Jin, K.; Yuan, D.; Zhou, H.; Yuan, J.; Huang, Y.; Hua, W.; Sun, J.; Zheng, P.; Hu, W.; Mao, Y.; Ma, M.; Zhang, G.; Zhou, F.; Zhao, Z. ($Li_{0.84}Fe_{0.16}$)OH$Fe_{0.98}$Se Superconductor: Ion-Exchange Synthesis of Large Single-Crystal and Highly Two-Dimensional Electron Properties. *Physical Review B* **2015**, *92*, 064515.

[169] Zhao, L.; Wang, D.; Huang, Q.; Wu, H.; Sun, R.; Fan, X.; Song, Y.; Jin, S.; Chen, X. Structural Evolution and Phase Diagram of the Superconducting Iron Selenides $Li_x(C_2H_8N_2)_yFe_2Se_2$ ($x = 0 \sim 0.8$). *Physical Review B* **2019**, *99* (9), 094503.

[170] Dong, X.; Zhou, H.; Yang, H.; Yuan, J.; Jin, K.; Zhou, F.; Yuan, D.; Wei, L.; Li, J.; Wang, X.; Zhang, G.; Zhao, Z. Phase Diagram of ($Li_{1-x}Fe_x$)OHFeSe: A Bridge between Iron Selenide and Arsenide Superconductors. *Journal of the American Chemical Society* **2015**, *137* (1), 66–69.

[171] Lu, X. F.; Wang, N. Z.; Wu, H.; Wu, Y. P.; Zhao, D.; Zeng, X. Z.; Luo, X. G.; Wu, T.; Bao, W.; Zhang, G. H.; Huang, F. Q.; Huang, Q. Z.; Chen, X. H. Coexistence of Superconductivity and Antiferromagnetism in ($Li_{0.8}Fe_{0.2}$)OHFeSe. *Nature Materials* **2015**, *14* (3), 325–329.

[172] Burrard-Lucas, M.; Free, D. G.; Sedlmaier, S. J.; Wright, J. D.; Cassidy, S. J.; Hara, Y.; Corkett, A. J.; Lancaster, T.; Baker, P. J.; Blundell, S. J.; Clarke, S. J. Enhancement of the Superconducting Transition Temperature of FeSe by Intercalation of a Molecular Spacer Layer. *Nature Materials* **2013**, *12* (1), 15--19.

[173] Sun, H.; Woodruff, D. N.; Cassidy, S. J.; Allcroft, G. M.; Sedlmaier, S. J.; Thompson, A. L.; Bingham, P. A.; Forder, S. D.; Cartenet, S.; Mary, N.; Ramos, S.; Foronda, F. R.; Williams, B. H.; Li, X.; Blundell, S. J.; Clarke, S. J. Soft Chemical Control of Superconductivity in Lithium Iron Selenide Hydroxides $Li_{1-x}Fe_x(OH)Fe_{1-y}Se$. *Inorganic Chemistry* **2015**, *54* (4), 1958–1964.

[174] Pachmayr, U.; Nitsche, F.; Luetkens, H.; Kamusella, S.; Bruckner, F.; Sarkar, R.; Klauss, H.-H.; Johrendt, D. Coexistence of 3d-Ferromagnetism and Superconductivity in $[(Li_{1-x}Fe_x)OH](Fe_{1-y}Li_y)Se$. *Angew. Chem. Int. Ed.* **2015**, *54* (1), 293--297.

[175] Pachmayr, U.; Johrendt, D. $[(Li_{0.8}Fe_{0.2})OH]FeS$ and the Ferromagnetic Superconductors $[(Li_{0.8}Fe_{0.2})OH]Fe(S_{1-x}Se_x)$ ($0 < x \leqslant 1$). *Chemical Communications* **2015**, *51*, 4689–4692.

[176] McQueen, T. M.; Williams, A. J.; Stephens, P. W.; Tao, J.; Zhu, Y.; Ksenofontov, V.; Casper, F.; Felser, C.; Cava, R. J. Tetragonal-to-Orthorhombic Structural Phase Transition at 90 K in the Superconductor Fe1.01Se. *Physical Review Letters* **2009**, *103* (5), 057002.

[177] Böhmer, A. E.; Hardy, F.; Wang, L.; Wolf, T.; Schweiss, P.; Meingast, C. Superconductivity-Induced Re-Entrance of the Orthorhombic Distortion in $Ba_{1-x}K_xFe_2As_2$. *Nature Communications* **2015**, 6 (1), 7911.

[178] Böhmer, A. E.; Hardy, F.; Eilers, F.; Ernst, D.; Adelmann, P.; Schweiss, P.; Wolf, T.; Meingast, C. Lack of Coupling between Superconductivity and Orthorhombic Distortion in Stoichiometric Single-Crystalline FeSe. *Physical Review B* **2013**, *87* (18), 180505.

[179] Zheng, H.; Wilfong, B. C.; Hickox-Young, D.; Rondinelli, J. M.; Zavalij, P. Y.; Rodriguez, E. E., Polar Ferromagnetic Metal by Intercalation of Metal–Amine Complexes. *Chemistry of Materials* **2021**.

[180] Sigrist, M.; Ueda, K.Phenomenological theory of unconventional superconductivity. *Rev. Mod. Phys.* **1991**, *63*, 239–311.

[181] Schnyder, A. P.; Ryu, S.; Furusaki, A.; Ludwig, A. W. W. Classification of topological insulators and superconductors. *Phys. Rev. B* **2008**, *78*, 195125.

[182] Fu, L.; Kane, C. L. Superconducting proximity effect and Majorana fermions at the surface of a topological insulator. *Phys. Rev. Lett.* **2008**, *100*, 096407.

[183] Tanaka, Y.; Yokoyama, T.; Nagaosa, N. Theory of topological spin current in noncentrosymmetric superconductors. *Phys. Rev. Lett.* **2009**, *103*, 107002.

[184] Yip, S.-K. Noncentrosymmetric superconductors. *Annu. Rev. Condens. Matter Phys.* **2014**, *5*, 15–33.

[185] Ramires, A. Symmetry aspects of chiral superconductors. *Contemp. Phys.* **2022**, *63*, 71–86.

[186] Kallin, C.; Berlinsky, A. J. Chiral superconductors. *Rep. Prog. Phys.* **2016**, *79*, 054502.

[187] Aiello, C. D.; Wei, R.; Naaman, R.; Waldeck, D. H.; Yang, S.-H.; Parkin, S. S. P. A chirality-based quantum leap. *ACS Nano* **2022**, *16*, 4989–5035.

[188] Ray, K.; Ananthavel, S. P.; Waldeck, D. H.; Naaman, R. Asymmetric scattering of polarized electrons by organized organic films of chiral molecules. *Science* **1999**, *283*, 814–816.

[189] Liu, Y.; Bian, Y.; Ren, J.; Yang, Y.; Wan, C. Chirality-driven topological electronic structure of DNA-like materials. *Nat. Mater.* **2021**, *20*, 362–368.

[190] Bian, Y.; Liu, Y.; Yang, Y.; Zhang, S.; Lu, H.; Ren, J.; Wang, J.; Zhou, Y.; Luo, J.; Wan, C. Hybrid chiral $MoS_2$ layers for spin-polarized charge transport and spin-dependent electrocatalysis. *Adv. Sci.* **2022**, *9*, 2200845.

[191] Göhler, B.; Hamelbeck, V.; Markus, T. Z.; Kettner, M.; Hanne, G. F.; Vager, Z.; Naaman, R.; Zacharias, H. Spin selectivity in electron transmission through self-assembled monolayers of double-stranded DNA. *Science* **2011**, *331*, 894–897.

[192] Alpern, H.; Yochelis, S.; Capua, A.; Capua, E.; Porath, D.; Millo, O. Unconventional superconductivity induced in Nb films by adsorbed chiral molecules. *New J. Phys.* **2016**, *18*, 113048.

[193] Sukenik, C. A.; Yochelis, S.; Yeshurun, Y.; Millo, O. Imprinting chirality on a conventional superconductor. *Adv. Phys. Res.* **2023**, *5*, 2300013.

[194] Nakajima, R.; Hayashida, S.; Fujiyama, S.; Tajima, N. Giant spin polarization and a pair of antiparallel spins in a chiral organic superconductor. *Sci. Adv.* **2023**, *9*, eadf0873.

[195] Ramires, A. Symmetry aspects of chiral superconductors. *Contemp. Phys.* **2022**, *63*, 71–86.

[196] Qian, Q.; Ren, H.; Zhou, J.; Wan, Z.; Zhou, J.; Yan, X.; Cai, J.; Wang, P.; Li, B.; Sofer, Z.; Li, B.; Duan, X.; Pan, X.; Huang, Y.; Duan, X. Chiral Molecular Intercalation Superlattices. *Nature* **2022**, *606*, 902–908.

[197] Wan, Z.; Qiu, G.; Ren, H.; Qian, Q.; Li, Y.; Xu, D.; Zhou, J.; Zhou, J.; Zhou, B.; Wang, L.; Yang, T.-H.; Sofer, Z.; Huang, Y.; Wang, K. L.; Duan, X. Unconventional Superconductivity in Chiral Molecule–$TaS_2$ Hybrid Superlattices. *Nature* **2024**, *632*, 69–74.

[198] Cheetham, A. K.; Mellot-Draznieks, C. Solid State and Hydrothermal Chemistry of Metal Phosphates and Oxalates. *Chem. Mater.* **1997**, *9*, 2269–2279.

[199] Walton, R. I.; O'Hare, D. Hydrothermal Synthesis of Inorganic Materials. *Chem. Commun.* **2000**, *7*, 2283–2291.

[200] Sedlmaier, S. J.; Cassidy, S. J.; Morris, R. G.; Drakopoulos, M.; Reinhard, C.; Moorhouse, S. J.; O'Hare, D.; Manuel, P.; Khalyavin, D.; Clarke, S. J. Ammonia-Rich High-Temperature Superconducting Intercalates of Iron Selenide Revealed through Time-Resolved In Situ X-ray and Neutron Diffraction. *J. Am. Chem. Soc.* **2014**, *136*, 630–633

[201] Gamage, E. H.; Greenfield, J. T.; Unger, C.; Kamali, S.; Clark, J. K.; Harmer, C. P.; Luo, L.; Wang, J.; Shatruk, M.; Kovnir, K. Tuning Fe–Se Tetrahedral Frameworks by a Combination of $[Fe(en)_3]^{2+}$ Cations and $Cl^-$ Anions. *Inorg. Chem.* **2020**, *59*, 13353–13363

[202] Shoemaker, D. P.; Hu, Y.-J.; Chung, D. Y.; Halder, G. J.; Chupas, P. J.; Soderholm, L.; Mitchell, J. F.; Kanatzidis, M. G. In Situ Studies of a Platform for Metastable Inorganic Crystal Growth and Materials Discovery. *Proc. Natl. Acad. Sci. U.S.A.* **2014**, *111*, 10922–10927

[203] Pienack, N.; Bensch, W. In Situ Monitoring of the Formation of Inorganic Materials in the Hydrothermal Synthesis Using Synchrotron Radiation. *Angew. Chem., Int. Ed.* **2011**, *50*, 2014–2034.

[204] Turrillas, X.; Martinez-Lara, M.; Cabeza, A. Applications of Time-Resolved X-ray Diffraction with Synchrotron Radiation in Solid-State Chemistry. *Radiat. Phys. Chem.* **1995**, *45*, 591–603.

[205] Kanatzidis, M. G.; et al. Direct Observation of the Mechanism of SnSe Formation by In Situ Time-Resolved X-ray Diffraction. *J. Am. Chem. Soc.* **2019**, *141*, 3690–3698.

[206] Sedlmaier, S. J.; Clarke, S. J. In Situ Studies of the Formation of Layered Bismuth Chalcogenides. *J. Am. Chem. Soc.* **2014**, *136*, 630–633.

[207] Panaro, S.; et al. Direct Observation of the Mechanism of SnSe Formation by In Situ Time-Resolved X-ray Diffraction. *J. Am. Chem. Soc.* **2019**, *141*, 3690–3698.

[208] Bensch, W.; et al. New Alkali- and Transition-Metal-Containing Thiophosphates: Synthesis and Structural Investigations. *Chem. Mater.* **2001**, *13*, 4590–4599.

[209] Francis, R. J.; et al. Hydrothermal Synthesis and Structural Characterization of New Layered Selenide Materials. *J. Am. Chem. Soc.* **1999**, *121*, 181–190.

[210] O'Hare, D.; et al. The Hydrothermal Synthesis and Structure of New Layered Hydroxide–Sulfide Materials. *Chem. Mater.* **1996**, *8*, 1283–1288.

[211] O'Hare, D.; et al. Hydrothermal Synthesis and Structure of New Layered Hydroxide–Halide Compounds. *Chem. Mater.* **2002**, *14*, 2199–2206.

[212] Crassous, J. Chiral Transfer in Coordination Complexes: Towards Molecular Materials. *Chem. Soc. Rev.* **2009**, *38*, 830–845.

[213] Gower, L. B. Biomimetic Model Systems for Investigating the Amorphous Precursor Pathway and Its Role in Biomineralization. *Chem. Rev.* **2008**, *108*, 4551–4627.